약학박사학위논문

항암치료를 위한 그래핀 기반 나노시트의 응용연구

Applications of Graphene-based Nanosheets for Anticancer Therapy

2014 년 8 월

서울대학교 대학원

약학과 물리약학전공

Wenjun Miao

항암치료를 위한 그래핀 기반 나노시트의 응용연구

Applications of Graphene-based Nanosheets for Anticancer Therapy

지도교수 오 유 경

이 논문을 약학박사학위논문으로 제출함

2014 년 6 월

서울대학교 대학원

약학과 물리약학전공

Wenjun Miao

Abstract

Applications of Graphene-based Nanosheets for Anticancer Therapy

Wenjun Miao

Physical Pharmacy, Department of Pharmacy

The Graduate School

Seoul National University

Graphene-based nanosheets (GNS) have emerged as novel and potent nanomedicines for cancer treatment. First, the surface of graphene oxide nanosheets was chemically modified by polyethylene glycol (PEG), and as-prepared PEG-grafted graphene oxide (pGO) showed significantly enhanced cellular delivery of photosensitizer chlorin e6 (Ce6) and much higher safety than GO nanosheets *in vivo*. Moreover, Ce6/Dox/pGO could accumulate in SCC7 tumor tissues and subsequently showed improved synergistic anticancer effect. Second, cholestryl hyaluronic acid-coated reduced graphene oxide nanosheets (CHA-rGO) were fabricated for tumor targeted delivery of chemotherapeutics. As compared to plain rGO, CHA-rGO nanosheets showed increased colloidal stability under

physiological conditions, improved *in vivo* safety, and enhanced loading capacity and cellular delivery efficiency of Dox. Molecular imaging of KB tumor-bearing mice indicated that CHA-rGO/Dox showed remarkable higher tumor tissue accumulation and greater tumor growth inhibition effect than other groups. Third, the effect of structure on the biological properties of photoresponsive carbon nanomaterials was investigated. Poloxamer 407-functionalized single-walled carbon nanotubes (PSWCNT) and poloxamer 407-functionalized graphene nanosheets (PGNS) exhibited similar physical stability and heating capacities after irradiation with an 808 nm near-infrared (NIR) laser. However, cancer cells treated with PGNS took up a higher quantity of the nanosheets than of the PSWCNT and displayed a higher rate of cancer cell killing upon laser irradiation. In addition, PGNS could circulate in the blood 2.2 times longer than that of the PSWCNT, and accumulate in the SCC7 tumor tissues to a greater degree than did PSWCNT. NIR irradiation resulted in the complete ablation of tumor tissues in the PGNS-treated group but not in the other groups. Last, CHA-rGO was utilized as tumor targeted delivery system for a NIR dye, ICG. CHA-rGO-loaded ICG showed substantially increased photo-stability and photothermal efficacy upon NIR laser irradiation than did free ICG. CHA-rGO/ICG nanophysisorplexes treated tumor-bearing mice displayed the highest tumor local temperature and subsequent tumor ablation. In conclusion, GNS can be used as novel delivery vehicles for various chemical drugs and surface-engineered GNS would be a potent modality of photothermal therapy for cancer treatment.

Keywords: Graphene-based nanosheets, Photodynamic therapy, Chemotherapy, Photothermal therapy, Enhanced anticancer effect

Student Number: 2010-31367

Contents

List of Tables

List of Figures

List of Abbreviations

Abbreviation	Word
AFM	atomic force microscopy
ANOVA	analysis of variance
AUC	area under curve
CAEC	cholesteryl-2-aminoethylcarbamate
Ce6	chlorin e6
CHA	cholesteryl hyaluronic acid
CI	combinational index
DAPI	4',6-diamidino-2-phenylindole dihydrochloride
Dox	doxorubicin
EPR	enhanced permeation and retention effect
FT-IR	Fourier transform infrared spectroscopy
GNS	graphene-based nanosheets
GO	graphene oxide
GQD	graphene quantum dot
HA	hyaluronic acid
hMSCs	human mesenchymal stem cells
ICG	indocyanine green
IONP	iron oxide nanoparticles

MTT	3-(4,5-dimethylthiazol-2-yl)-2,5-diphenyltetrazolium bromide
MRI	magnetic resonance imaing
MRT	mean residence time
NIR	near infrared
PCNA	proliferating cell nuclear antigen
PDT	photodynamic therapy
pGO	peglyated graphene oxide
PGNS	poloxamer 407-functionalized graphene nanosheets
PSWCNT	poloxamer 407-functionalized single-walled carbon nanotubes
PTT	photothermal therapy
rGO	reduced graphene oxide
TUNEL	terminal deoxynucleotidyl transferase dUTP nick-end labeling

Chapter I

Overview

1. Introduction

Graphene, a novel two dimensional nanomaterials composed of atomic-thickness monolayers of hexagonally arranged sp^2-hybridized carbon atoms, has become one of the hottest topics in the fields of materials science, physics, chemistry, and nanotechnology [1]. A single-layer sheet of graphene was discovered and isolated in 2004 by K. S. Novoselov and A. K. Geim, who were awarded the 2010 Novel Prize in physics. As a basic building block of other carbon allotropes, graphene can be wrapped to generate zero-dimensional fullerenes, rolled up to form one-dimensional carbon nanotubes, and stacked to produce three-dimensional graphite (Fig. I-1) [2]. Due to its unique structure and geometry, graphene exhibits distinctly different properties, such as its high planar surface (calculated value, 2630 m^2/g) [3], superlative mechanical strength (Young's modulus, ~1100 GPa) [4], unparalleled thermal conductivity (~5000 W/m/K) [5], and remarkable electronic properties [6, 7]. These distinguished properties of graphene provide essentially infinite possibilities for various applications in many areas, including those pertaining to nanoelectronic devices [8], energy technology [9, 10], and transparent conductors [11].

Graphene-based nanosheets (GNS) are generally composed of graphene and its derivatives encompassing graphene oxide (GO) and reduced graphene oxide (rGO). The chemical approach for production of GO nanosheets involves initial oxidation of graphite and mechanical or thermal exfoliation [12]. GO nanosheets contain hydroxyl (-OH) and epoxide (-O-) functional groups on their basal surfaces

and carboxyl functional groups at their plane edges (Fig. I-2A) [13]. They are hydrophilic, and readily disperse in water and polar solvents, such as dimethyl formamide [14]. GO nanosheets have been treated with high temperature and reducing agents (e.g., hydrazine) to produce reduced GO (rGO) nanosheets (Fig. I-2B) [15]. However, the reduction of GO also increases light absorption in the visible and near infrared (NIR) region due to recovery of the conjugated π network of graphene [16, 17]. Furthermore, decreasing the oxygen content to generate rGO was shown to increase its hydrophobicity and improve protein loading [18].

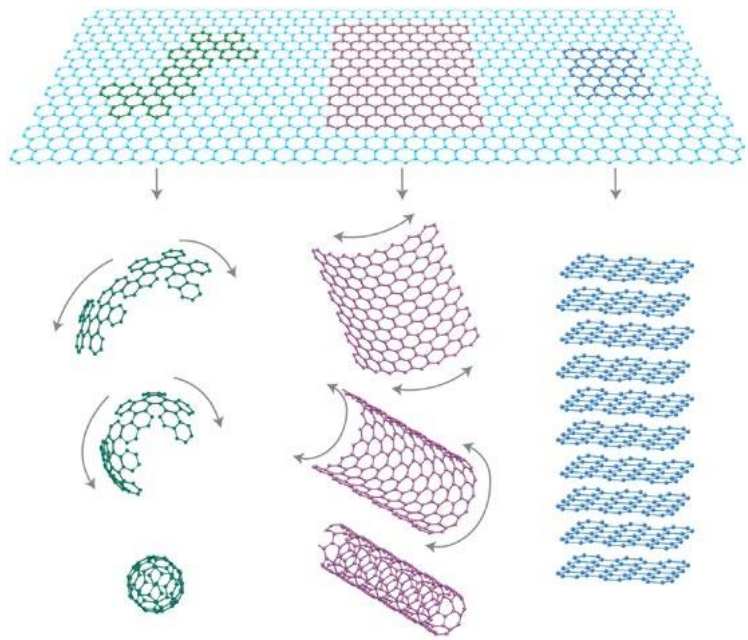

Fig. I-1. Graphene: the parent of all graphitic forms.

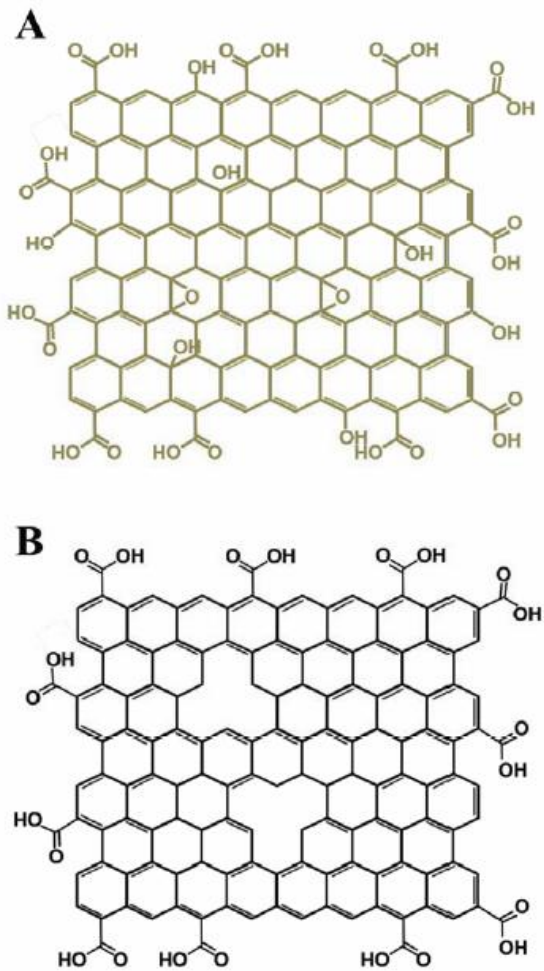

Fig. I-2. Functional groups of GO and rGO nanosheets.

Hydroxyl, epoxide and carboxyl groups are present on GO nanosheets (A), and carboxyl groups are on plane edges of rGO nanosheets (B).

2. Biomedical applications of graphene-based materials

Beyond the applications aforementioned, the biomedical applications of graphene-based materials are a relative new area with significant potential. Since the seminal report on use of GO as an efficient nanocarrier for drug delivery by Dai et al. in 2008 [19], the first study on graphene for biomedical applications, a lot of interesting work has been carried out to explore the use of GNS for widespread biomedical applications, ranging from drug/gene delivery, biological sensing and imaging, antibacterial materials, to biocompatible scaffold for cell culture, as listed in Table I-1.

2.1. Biosensing

Since the discovery of graphene, there has been a significant number of publications reporting graphene-based biosensors [20-35], mainly utilized the unique chemical, optical, electrical and eletrochemical properties of GNS. It has been found that the nucleotide bases in ssDNA bind strongly to the graphene surface by π-π interaction, which could be greatly weakened after DNA hybridization to form dsDNA [27-31]. Several different groups have utilized this phenomenon, as well as the effective fluorescence-quenching ability of graphene, to develop novel graphene-based DNA detection platforms [24, 27-30]. Fan and co-workers reported a GO-based multicolor DNA probe for rapid, sensitive and selective detection of DNA targets in solutions [28]. Others found that graphene could deliver oligonucleotides, such as molecular beacons and aptamers, into living

cells for in situ probing of biomolecules [24, 29].

Many other graphene-based biosensing systems using different mechanisms have also been studied [20, 31, 34, 36-37]. In 2008, Mohanty et al. for the first time successfully fabricated graphene electronic devices for detection of bacterium, DNA and proteins [20]. Since then, biosensing using graphene electronic devices has been actively pursued [25, 32, 36-38]. Owing to its ultra-high surface area and excellent electron mobility, graphene and graphene-based composite materials were used to modify electrodes in the electrochemical sensing of various biomolecules, including glucose, DNA and proteins, with high sensitivities [33, 39-43]. Recently, a number of groups have also used graphene as a novel matrix for mass spectrometry assay of biological molecules. Furthermore, graphene could also be combined with other nanomaterials for various novel biosensing applications [44-48].

Table I-1. Biomedical applications of GNS.

Application	Examples	Ref.
Graphene-based biosensors		
Optical sensing	Oligonucleotides	[24,27,29]
	Proteins (e.g.,thrombin)	[123,124]
	Heavy metal ions (e.g., Ag)	[125]
	Pathogen (e.g.,rotavirus)	[25]
Electrochemical sensing	Biomacromolecules	[39,126-127]
	Enzymes	[22,33,42]
	Small molecules	[23, 43]
Matrix for mass spectra	Small molecules or DNA	[24,128]
Bioimaging		
Fluorescence imaging	Graphene quantum dot (GQD)	[53-58]
MRI	Fe_3O_4-GO nanocomposite	[51]
GNS for potent anticancer therapy		
Drug delivery	Chemotherapeutics	[79-85]
Gene delivery	plasmid DNA	[73,74]
Photodynamic therapy	Photosensitizers (e.g., Ce6）	[77,86-89]
Photothermal therapy	PEG-rGO,GO-AuNP nanocomposite	[99-102]
Combinational therapy	Chemo-gene, Chemo-PTT	[103-106]
Theranostics	MRI, FL, PA	[116-122]
Other applications		
Antibacterial papers	GO and rGO paper	[61-62]
Tissue engineering scoffolds	NIH-3T3 fibroblasts, hMSCs	[63-66]

2.2. Bioimaging

Exploration the feasibilities of GNS in biological imaging with optical and magnetic modalities have been initiated [49-52]. Dai et al. [50] firstly examined cellular uptake of PEG-modified GO loaded with chemical drugs using intrinsic fluorescence of GO in the NIR region. Later, researchers have begun to prepare smaller GO (with a size of 10 nm or less), often referred to as graphene quantum dots (GQDs), from chemical oxidation of graphite [53-55] and "bottom-up" approach [56]. These GQDs exhibit intrinsic fluorescence, and can be used for bioimaging purposes. Compared with CdSe and other II-VI type QDs, GQDs show excellent biocompatibility, physical solubility, and low cytotoxicity, and can be used directly for intracellular imaging without the necessity of further surface processing or functionalization. In addition, GQDs possess unique optical properties such as pH dependent and upconversion fluorescence behaviors [57]. The upconversion fluorescence property of GQDs allows them to be excited at NIR region, making both *in vitro* and *in vivo* bio-detection and imaging efficient, safe and without interference from auto-fluorescence from the cells, organs, or tissues in this region [58].

Like fluorescence imaging technique, magnetic resonance imaging (MRI) is widely used in clinical practice [56, 60]. Composite of dextran-coated Fe_3O_4 nanoparticles and GO (Fe_3O_4-GO) has been reported as T_2-weighted contrast agent for efficient cellular MRI. The Fe_3O_4-GO composites possess good physiological stability and low cytotoxicity. Compared with the isolated Fe_3O_4 nanoparticles, the Fe_3O_4-GO composites exhibit significantly enhanced cellular MRI [51].

2.3. GO-based antibacterial materials

Fan et al. [61] prepared macroscopic freestanding GO and rGO paper from their suspension by vacuum filtration technique, and found that these papers exhibit strong antibacterial effect. Considering the scale up ability and low cost of the graphene-based antibacterial paper, this work opens new opportunities for the use of GO in environmental and clinical application. Liu et al. [62] further probed the mechanism of antibacterial effect of 4 types of graphene derivatives, graphite (Gt), graphite oxide (GtO), GO and rGO. They found that the antibacterial activities decrease in the order of GO, rGO, Gt and GtO. The assign the antibacterial effect to both membrane and oxidative stress, and then proposed a three-step mechanism for the antibacterial effect, similar to that of carbon nanotubes.

2.4. GO-based scaffold for cell culture

Min's group studied the behavior of NIH-3T3 fibroblasts as a model of mammalian cells growing on a supported film of GO [63]. Their work suggests that GO film induces no significant harmful effect on the mammalian cells with respects to adhesion, and exhibits remarkably high gene transfection efficiency, indicating the potential application of GO as a surface coating materials for implant.

A graphene/chitosan film produced by solution casting method has also been investigated as scaffold materials in tissue engineering [64]. The work indicates that the graphene-based film does not hamper the proliferation of human mesenchymal stem cells (hMSCs). Instead, it accelerates their specific

differentiation into bone cells in a controlled manner through the use of growth factors and osteogenic inducers, suggesting the potential use for proliferation and transplantation of stem cell and their specific differentiation into muscles, bones, and cartilages for bone regeneration therapy [65]. Another study [66] revealed that chemical vapor deposition (CVD) grown graphene substrate is biocompatible for human osteoblasts as well as for hMSCs with higher proliferation of cell, compared to SiO_2 substrate, and stimulates the growth and differentiation of cells.

3. GNS as novel nanomaterials for anticancer therapy

The unique structural features, such as large and planar sp^2 hybridized carbon domain, high specific surface area (2630 m^2/g), and enriched oxygen-containing groups, render GNS excellent biocompatibility, and capability of loading of drugs and genes via chemical conjugation or physical adsorption approaches. Moreover, the reactive carboxyl and hydroxyl groups GNS bears facilitate conjugation with various systems, such as polymers [67], biomolecules (biotargeting ligand [50], DNA [68], protein [69, 70]), quantum dots [71], Fe_3O_4 nanoparticles [51], and others [72], imparting GNS with multi-functionalities, and multi-modalities for diverse approaches for anticancer therapy.

3.1. Surface-engineering of graphene-based nanosheets

GNS, without any surface functionalization, usually has sheet dimensions of hundreds of nanometers and tends to aggregate in physical solutions with salts and proteins due to screening of electrostatic charges and non-specific binding of proteins. To improve the physiological stability and reduce toxicity of GNS, it is necessary to modify and functionalize graphene by other biocompatible polymers. Among such materials, polyethylene glycol (PEG) is frequently applied to modify GNS via non-covalent or covalent methods for imaging, drug delivery and photothermal therapy. In 2008, Dai's group for the first time reported 6-arm-branched PEG chemically modified graphene oxide showed excellent stability in a variety of physiological solutions for delivery of aromatic anticancer

chemicals [19]. Other materials, such as polyethyleneimine, chitosan, Pluronic and dextran, are reported to stabilize and functionalize graphene as well [73-76]. This strategy enables GNS to have long circulation time and passively target to tumor tissue via enhanced permeation and retention (EPR) effect. However, targeted drug delivery using graphene as a vehicle is still desirable.

So far, there are only a few reports about conjugating targeting ligands onto GNS for active targeting to tumor cell. Sun et al for the first time utilized anti-CD20 antibody conjugated pegylated graphene oxide to Raji B cells [50]. Arg-Gly-Asp (RGD) peptide is also used to modify reduced graphene oxide for selective photothermal therapy, which showed potent photothermal efficacy to U87MG cells *in vitro* [16]. Cui's group employed folic acid-conjugated graphene oxide for targeted photodynamic therapy [77]. Hong et al. conjugated reduced graphene oxide with anti-CD105 antibody TRC105, and this conjugated showed improved tumor uptake of graphene by positron emission tomography imaging [78]. Above-described strategies show promise to use graphene based materials for cancer-targeted drug delivery, photodynamic therapy and/or photothermal therapy. However, their fabrication processes are somehow complicated and cost high, which inhibit their translation in future.

3.2. GNS for chemotherapy

The ability of graphene to physically adsorb various compounds has prompted many researchers to use it as a potential drug carrier for cancer treatment. The first such study introduced a new research area by demonstrating that GO nanosheets

can be used as an efficient nanocarrier for drug delivery [19]. In their approach, nanographene oxide was first conjugated with an amine-terminated six armed PEG molecule, followed by loading of a water insoluble anticancer drug SN38 onto GO surface by simple non-covalent adsorption. The PEG-functionalized GO loaded with SN38 exhibited high cytotoxicity for HCT-116 cells, 1000-fold more potent than CPT-11. And their work demonstrated that the drug release from the GO surface was pH dependent, suggesting the possibility of pH-controlled drug release [50]. After that, various anticancer chemotherapeutics have been loaded onto GNS, including doxorubicin (Dox) [79-81], methotrexate [82], ellagic acid [83], comptothecin [84] and 5-fluorouracil [85].

Although numerous studies have examined the utility of GNS as chemical anticancer drug carriers, most of these researches have been done at the *in vitro* level. Only a few studies have tested the feasibility of GNS as drug carriers *in vivo*. Thus, more *in vivo* studies are needed to assess the safety, biodistribution, pharmacokinetics and therapeutic efficacy of GNS.

3.3. GNS for gene therapy

Successful gene therapy requires a gene vector that protects genes from nuclease degradation and facilitate cellular uptake of genes with high transfection efficiency. The major challenge facing the development of gene therapy is the lack of potent and safe gene vectors. Liu's group [74] reported that GO conjugated with positively charged polyethylenimine (PEI) allows condensation of plasmid DNA onto the surface of GO sheet through electrostatic interaction arising from the

cationic polymer. The grafting of PEI to GO not only significantly lowered the cytotoxicity of free PEI, but also improved the transfection efficiency of the cationic polymer. Besides PEI, chitosan is also used to modify GO and condense plasmid DNA into stable nanoparticles which show reasonable DNA transfection efficiency in HeLa cells at optimized nitrogen/phosphate ratio [73].

3.4. GNS for photodynamic therapy (PDT)

Although chemotherapy is the major and most widely available therapeutic strategy against cancer at this time, the use of GNS for chemotherapy has been limited by the lack of specific delivery methods with the killing of healthy and cancer cells alike. Phototherapies, such as photodynamic therapy (PDT) and photothermal therapy (PTT), can generate specific killing of cancer cells following localized irradiation of the tumor site. PDT requires the generation of reactive oxygen species produced from photosensitizers (PS), which can be loaded onto GNS by hydrophobic interactions and π-π stacking.

For PDT, GNS can be loaded with various PS, including Ce6 [77, 86-87], hypocrellin A [88], and hypocrellin B [89]. Although most of the studied chemical drugs have been loaded onto GNS via hydrophobic interactions and π-π stacking, Ce6 was reported to be loaded onto GO nanosheets via a disulfide bond linker [86]. Due to the fluorescence-quenching ability of GO, Ce6 was neither fluorescent nor phototoxic as long as it was bound to GO nanosheets. Upon entering a cell, this disulfide bond linker was cleaved by the abundant redox agents (e.g., glutathione) found in intracellular compartments, separating Ce6 from GO and leading to

fluorescence and cell-killing effects upon light irradiation. This redox-responsive GO-Ce6 conjugate thus conferred tumor site-specific NIR fluorescence imaging and PDT activation by utilizing redox agents such as glutathione or dithiothreitol that are naturally present at high levels in cancer cells [90]. Hyaluronic acid (HA)-conjugated GO was also developed as a cancer-targeting PDT [87]. When Ce6 was loaded to HA-grafted GO via π-π stacking and hydrophobic interactions, it showed increased cellular uptake in HeLa cells compared to free Ce6, and provided improved photodynamic effect upon light irradiation.

3.5. GNS for photothermal therapy (PTT)

Photothermal therapy (PTT) for treating solid tumors, as an attractive alternative way which utilizes the conversion of absorbed light into local heating through non-irradiative mechanism, has been widely investigated because of its advantages, including spatial and temporal controllability, minimal invasion and few complications [91-95]. Light in the near-infrared (NIR) region (700-1100 nm) used in PTT enables deep tissue penetration and low energy absorption of normal tissue [96-98]. Light-absorbing agents with high absorption in NIR region are generally involved in PTT process for effective energy conversion from light to heat in localized tumor tissue.

GNS possesses high visible and NIR absorbance that can be exploited for PTT. PEG-coated rGO was reported to show significant photothermal antitumor effects in tumor-bearing mouse models [99]. After intravenous injection of PEG-coated rGO (20 mg/kg), 4T1 murine breast cancer-bearing mice were irradiated for 5 min

with an 808-nm laser. This treatment yielded significant tumor growth inhibition and almost complete elimination of the tumor mass. No death or tumor-recurrence was observed among these mice over 100 days. GO and rGO were coated with gold nanoparticles and applied for PTT [100-101]. Gold nanoparticles anchored to GO enhanced the temperature increase observed upon NIR irradiation more effectively than gold nanoparticles or GO alone [102]. Human umbilical vein endothelial cells were treated with gold nanoparticles alone, gold nanoparticle-coated GO, or gold nanoparticle-coated rGO and irradiated at 808 nm. The results revealed that gold nanoparticle-coated rGO killed the cells more rapidly than gold nanoparticle-coated GO or gold nanoparticles alone.

The use of GNS for PTT is attractive because PTT does not require any loading of drug compound to induce its therapeutic effects; the photothermal activity of GNS alone is sufficient to kill cells following NIR irradiation [16, 99]. In addition, researchers are currently attempting to improve the photoresponsiveness of GNS and reduce the required intensity and time of NIR irradiation, thereby reducing its side effects in normal tissues.

3.6. GNS for combinational therapy

Thanks to their versatile interactive properties, GNS may be loaded with various molecules ranging from chemicals to nucleic acids. They have been studied as suitable materials for combinational chemotherapy [103], chemo-gene therapy [103-105], and chemo-PTT [106].

Polyethylenimine (PEI)-functionalized GO has been assessed for chemo-gene

therapy. PEI-functionalized GO was loaded with Dox and small interference RNA (siRNA) against Bcl-2 via electrostatic interaction with positively charged PEI on GO [107]. PEI-grafted GO was also used to co-deliver Dox and microRNA-21 [108], enhancing the cytotoxic effects and intracellular accumulation of Dox observed in MCF-7/ADR cells.

Dox-loaded PEG-GO was studied as a means to combine chemotherapy and PTT [109]. The combination of Dox and NIR irradiation showed higher tumor growth inhibition compared to free Dox or PTT alone. For tumor-targeted delivery, FA-grafted, polyvinylpyrrolidone -stabilized GO was loaded with Dox for chemo-PTT [106] and found to effectively kill HeLa cells upon NIR irradiation. A recent study reported that photothermal effects could promote endosomal escape after the cellular uptake of graphene [110]. The release of Dox from rGO was shown to be triggered by NIR irradiation, which enhanced the cytotoxicity of the drug in HeLa and PC3 cells.

GO-based photodynamic and photothermal combination strategies have been proposed using PEG-functionalized GO [111] or amphiphilic block copolymer-coated GO [76]. PEG-functionalized GO was loaded with Ce6 for PDT [111] and applied to KB cells, which were first irradiated with 808 nm NIR to induce the photothermal effect, followed by 660 nm laser irradiation to activate Ce6. The authors observed that this combined treatment had a synergistic effect.

3.7. GNS for theranostics

"Theranostics," which is an amalgamation of the words "therapeutics" and

"diagnostics," refers to the co-delivery of a therapeutic agent plus a monitoring agent. This dual functionality allows researchers to monitor the delivery kinetics and efficacy of a drug in real-time, potentially eliminating the risk of obtaining divergent biodistribution and selectivity profiles from the separate use of a biomarker and a therapeutic agent [112]. Furthermore, theranostics is leading the way towards the development of patient-specific therapies. Because the ultimate goal of theranostics is to enable real-time monitoring of drug behavior, it may be used to flexibly tune treatment parameters (e.g., drug dosage and administration timing) according to a given patient's response profile [113]. Nanomaterials (e.g., quantum dots and gold particles) are considered to be major candidates for theranostics, as are carbon-based nanomaterials, such as fullerenes, carbon nanotubes, and graphene [114-115]. Examples of GNS for theranostic applications are summarized in Table I-2.

GNS were covalently pegylated with branched PEG having Cy7 conjugated to one of its amine ends [116], enabling fluorescence imaging. The imaging data indicated longer blood circulation of GNS-PEG-Cy7 compared to non-pegylated GNS. Intravenously injected GNS-PEG-Cy7 was detected in all organs of injected mice at 1 h post-injection, but was observed only in kidneys and tumor tissues by 24 h post-injection. Executing the photothermal effect of GNS significantly reduced the tumor volume and improved survival up to 40 days compared to the non-irradiated group, which showed full mortality within 20 days.

Another model is the coating of rGO-iron oxide nanoparticle (IONP) nanocomposites with PEG via non-covalent interactions [117]. In addition to

exploiting the strong intrinsic magnetism and NIR absorbance of the nanocomposite, this system employed Cy5 to allow tri-modal imaging at the fluorescent, photoacoustic, and magnetic resonance (MR) levels. As for therapeutic effects, the authors reported that enhanced photothermal effects arose due to the considerable reduction of GO during the synthesis of rGO-IONP.

Multimodal imaging device, GO-IONP-Au-PEG, was developed [118] as a dual-functionalization of GO with the magnetic factor, IONP, and the plasmonic factor, gold. This nanocomposite was further coated with lipoic acid-PEG and FA-modified lipoic acid-PEG to increase its physiological stability, and GO-IONP-Au-PEG was found to be suitable for X-ray and MR dual-imaging. Upon laser irradiation at 808 nm, it also exhibited strong heat generation and antitumor effects *in vitro* and *in vivo*.

Table I-2. Applications of GNS for theranostics.

Probe	Diagnostic	Therapy	Ref.
Cy7	Fluorescence imaging	PTT	[116]
IONP, Cy5	Fluorescence, PAT, and MRI	PTT	[117]
IONP, Au	MRI, X-ray	PTT	[118]
IONP	MRI	Dox	[119]
AuNP	Ultrasound imaging, CT	PTT	[120]
—	Photoacoustic imaging	PTT	[121]
Superparamagnetic IONP	MRI	Dox and pDNA	[122]

4. Scope of the studies

As a class of novel nanomaterials, GNS have drawn tremendous attention in their applications in biomedical field, especially for anticancer therapy. Many research groups have emphasized the benefits of GNS, such as their high capacity for drug loading, photothermal effect, versatile modifiability, etc. The main objective of the current studies is to explore new approaches for cancer treatment using GNS.

In chapter II, we synthesized GO and pGO nanosheets and compared their *in vitro* cytotoxicity and *in vivo* safety. Next, we tested whether a Ce6-pGO nanophysisorplex could be delivered to tumor tissues, as assessed by *in vivo* imaging in mice. Moreover, we evaluated the synergistic photodynamic effects of Ce6- and Dox-dual loaded pGO nanophysisorplexes in tumor-bearing mice.

In chapter III, we tested whether HA could be used to increase graphene-based nanosheets stability and safety, and enhance the tumor-targeted distribution of anticancer drugs to CD44-overexpressing cancer cells.

In chapter IV, using amphiphilic triblock copolymer-functionalized SWCNT and graphene nanosheets, we tested whether the structure of carbon-based nanomaterials could affect their physical properties, *in vivo* fates, and photothermal anticancer effects.

In chapter V, we tested whether the use of graphene-based photothermal nanoplatform for delivery of ICG could improve the photothermal potency. Moreover, to enhance tumor accumulation, cellular internalization and subsequent

photothermal tumor destruction efficacy, we used cholesteryl hyaluronic acid-coated reduced graphene oxide nanosheets (CHA-rGO) for ICG delivery vehicle to CD44-overexpressing xenograft tumor.

5. References

[1] Geim AK. Graphene: status and prospects. Science 2009;324:1530-34.

[2] Rao CNR, Sood AK, Subrahmanyam KS, Govindaraj A. Graphene: the new two-dimensional nanomaterials. Angew Chem Int Ed 2009;48:7752-77.

[3] Stoller MD, Park S, Zhu Y, An J, Ruoff, RS. Graphene-based ultracapacitors. Nano Lett 2008;8:3498-502.

[4] Lee C, Wei X, Kysar JW, Hone J. Measurements of the elastic properties and intrinsic strength of monolayer graphene. Science 2008;321:385-88.

[5] Balandin AA, Ghosh S, Bao W, Calizo I, Teweldebrhan D, Miao F, Lau CN. Superior thermal conductivity of single-layer graphene. Nano Lett 2008;8:902-07.

[6] Geim AK, Novoselov KS. The rise of graphene. Nat Mater 2007;6:183-91.

[7] Chen D, Tang L, Li J. Graphene-based materials in electrochemistry. Chem Soc Rev 2010;39:3157-80.

[8] Xuan Y, Wu YQ, Shen T, Qi M, Capano MA, Cooper JA, Ye PD. Atomic-layer-deposited nanostructures for graphene-based nanoelectronics. Appl Phys Lett 2008;92:013101.

[9] Wang L, Lee K, Sun YY, Lucking M, Chen Z, Zhao, JJ, Zhang SB. Graphene oxide as an ideal substrate for hydrogen storage. ACS Nano 2009;3:2995-3000.

[10] Liu C, Alwarappan S, Chen Z, Kong X, Li CZ. Membrane-less enzymatic biofuel cells based on graphene nanosheets. Biosens Bioelectron 2010;25:1829-33.

[11] Stankovich S, Dikin DA, Piner RD, Kohlhaas KA, Kleinhammes A, Jia Y, Wu Y, Nguyen ST, Ruoff RS. Synthesis of graphene-based nanosheets via chemical reduction of exfoliated graphite oxide. Carbon 2007;45:1558-65.

[12] Seo JT, Green AA, Antaris AL, Hersam MC. High-concentration aqueous dispersions of graphene using nonionic, biocompatible block polymers. J Phys Chem Lett 2011,2:1004-08.

[13] Park S, An J, Jung I, Piner RD, An SJ, Li X, Velamakanni A, Ruoff RS. Colloidal suspensions of highly reduced graphene oxide in a wide variety of organic solvents. Nano Lett 2009,9:1593-97.

[14] Niyogi S, Bekyarova E, Itkis ME, McWilliams JL, Hamon MA, Haddon RC. Solution properties of graphite and graphene. J Am Chem Soc 2006,128:7720-21.

[15] Park S, Ruoff RS, Chemical methods for the production of graphenes. Nat Nanotech 2009;4:217-24.

[16] Robinson JT, Tabakman SM, Liang Y, Wang H, Casalongue HS, Vinh D, Dai H. Ultrasmall reduced graphene oxide with high near-infrared absorbance for photothermal therapy. J Am Chem Soc 2011:133:6825-31.

[17] Kim J, Kim F, Huang J. Seeing graphene-based sheets. Mat Today

2010,12:28-38.

[18] Zhang Y, Zhang J, Huang X, Zhou X, Wu H, Guo S. Assembly of graphene oxide-enzyme conjugates through hydrophobic interaction. Small 2012,8:154-59.

[19] Liu Z, Robinson JT, Sun X, Dai H. PEGylated nanographene oxide for delivery of water-insoluble cancer drugs. J Am Chem Soc 2008;130:10876-77.

[20] Mohanty N, Berry V. Graphene-based single-bacterium resolution biodevice and DNA transistor: interfacing graphene derivatives with nanoscale and microscale biocomponents. Nano Lett 2008;8:4469–76.

[21] Zhou M, Zhai YM, Dong SJ. Electrochemical sensing and biosensing platform based on chemically reduced graphene oxide. Anal Chem 2009;81:5603–13.

[22] Shan CS, Yang HF, Song JF, Han DX, Ivaska A, Niu L. Direct electrochemistry of glucose oxidase and biosensing for glucose based on graphene. Anal Chem 2009;81:2378–82.

[23] Song YJ, Qu KG, Zhao C, Ren JS, Qu XG. Graphene oxide: intrinsic peroxidase catalytic activity and its application to glucose detection. Adv Mater 2010;22:2206–10.

[24] Tang LAL, Wang JZ, Loh KP. Graphene-based SELDI probe with ultrahigh extraction and sensitivity for DNA oligomer. J Am Chem Soc 2010;132:10976–77.

[25] Wang Y, Li ZH, Hu DH, Lin CT, Li JH, Lin YH. Aptamer/graphene

oxide nanocomplex for in situ molecular probing in living cells. J Am Chem Soc 2010;132:9274–9276.

[26] Nelson T, Zhang B, Prezhdo OV. Detection of nucleic acids with graphene nanopores: ab initio characterization of a novel sequencing device. Nano Lett 2010;10:3237–42.

[27] Jang HJ Kim YK Kwon HM Yeo WS Kim DE Min DH. A graphene-based platform for the assay of duplex-DNA unwinding by helicase. Angew Chem Int Ed 2010;49:5703–07.

[28] He SJ, Song B, Li D. Graphene nanoprobe for rapid, sensitive, and multicolor fluorescent DNA analysis. Adv Funct Mater 2010;20: 453–59.

[29] Lu CH, Zhu CL, Li J, Liu JJ, Chen X, Yang HH. Using graphene to protect DNA from cleavage during cellular delivery. Chem Commun 2010;46:3116–68.

[30] Balapanuru J, Yang JX, Xiao S. Graphene oxide–organic dye ionic complex with DNA-Sensing and optical-limiting properties. Angew Chem Int Ed 2010;49:6549–53.

[31] Chen D, Tang L, Li J. Graphene-based materials in electrochemistry. Chem Soc Rev 2010;39:3157–80.

[32] Ohno Y, Maehashi K, Yamashiro Y, Matsumoto K. Electrolyte-gated graphene field-effect transistors for detecting pH protein adsorption. Nano Lett 2009;9:3318–22.

[33] Zeng QO, Cheng JS, Tang LH. Self-assembled graphene–enzyme hierarchical nanostructures for electrochemical biosensing. Adv Funct

Mater 2010;20:3366–72.

[34] Chen XP, Ye HZ, Wang WZ, Qui B, Lin ZY, Chen GN. Electrochemiluminescence biosensor for glucose based on graphene/ nafion/GOD film modified glassy carbon electrode. Electroanalysis 2010;22:2347–52.

[35] Shao YY, Wang J, Wu H, Liu J, Aksay IA, Lin YH. Graphene based electrochemical sensors and biosensors: a review. Electroanalysis 2010;22:1027–36.

[36] Cohen-Karni T, Qing Q, Li Q, Fang Y, Lieber CM. Graphene and nanowire transistors for cellular interfaces and electrical recording. Nano Lett 2010;10:1098–02.

[37] Dong XC, Shi YM, Huang W, Chen P, Li LJ. Electrical detection of DNA hybridization with single-base specificity using transistors based on CVD-grown graphene sheets. Adv Mater 2010;22:1649–53.

[38] Stine R, Robinson JT, Sheehan PE, Tamanaha CR. Real-time DNA detection using reduced graphene oxide field effect transistors. Adv Mater 2010;22:5297–5300.

[39] Zhou M, Zhai YM, Dong SJ. Electrochemical sensing and biosensing platform based on chemically reduced graphene oxide. Anal Chem 2009;81:5603–13.

[40] Liu Y, Yu DS, Zeng C, Miao ZC, Dai LM. Biocompatible graphene oxide-based glucose biosensors. Langmuir 2010;26:6158–60.

[41] Kang XH, Wang J, Wu H, Aksay IA, Liu J, Lin YH. Glucose

oxidase–grapheme–chitosan modified electrode for direct electrochemistry and glucose sensing. Biosens Bioelectro 2009;25:901–905.

[42] Lim CX, Hoh HY, Ang PK, Loh KP. Direct voltammetric detection of DNA and pH sensing on epitaxial graphene: an insight into the role of oxygenated defects. Anal Chem 2010:82:7387–93.

[43] Lu CH, Yang HH, Zhu CL, Chen X, Chen GN. A graphene platform for sensing biomolecules. Angew Chem Int Ed 2009;48:4785–87.

[44] Jung JH, Cheon DS, Liu F, Lee KB, Seo TS. A graphene oxide based immuno-biosensor for pathogen detection. Angew Chem Int Ed 2010;49:5708–11.

[45] Baby TT, Aravind SSJ, Arockiadoss T, Rakhi RB, Ramaprabhu S. Metal decorated graphene nanosheets as immobilization matrix for amperometric glucose biosensor. Sensor Actuat B Chem 2010;145: 71–77.

[46] Mao S, Lu GH, Yu KH, Bo Z, Chen JH. Specific protein detection using thermally reduced graphene oxide sheet decorated with gold nanoparticle–antibody conjugates. Adv Mater 2010;22:3521–26.

[47] Wang K, Liu QA, Wu XY, Guan QM, Li HN. Graphene enhanced electrochemiluminescence of CdS nanocrystal for H_2O_2 sensing. Talanta 2010;82:372–76.

[48] Xia TA, Kovochich, M, Liong M. Polyethyleneimine coating enhances the cellular uptake of mesoporous silica nanoparticles and allows safe

delivery of siRNA and DNA constructs. ACS Nano 2009;3: 3273–86.

[49] Loh KP, Bao QL, Eda G. Graphene oxide as a chemically tunable platform for optical applications. Nat chem 2010;2:1015-24.

[50] Sun XM, Liu Z, Welsher K. Nano-graphene oxide for cellular imaging and drug delivery. Nano Res. 2008;1:203-212.

[51] Chen WH, Yi PW, Zhang Y. Composites of aminodextran-coated Fe_3O_4 nanoparticles and graphene oxide for cellular magnetic resonance imaging. ACS Appl Mater Interfaces 2011;3:4085-91.

[52] Bianco A, Kostarelos K, Partidos CD. Biomedical applications of functionalised carbon nanotubes. Chem Commun 2005;5:571-77.

[53] Pan DY, Zhang JC, Li Z. Hydrothermal route for cutting graphene sheets into blue-luminescent graphene quantum dots. Adv Mater 2010;22:734-38.

[54] Eda G, Lin YY, Mattevi C. Blue photoluminescence from Chemically Derived Graphene Oxide. Adv Mater 2010;2:505-09.

[55] Mei QS, Zhang K, Guan GJ. Highly efficient photoluminescent graphene oxide with tunable surface properties. Chem Commun 2010;46:7319-21.

[56] Yan X, Cui X, Li LS. Synthesis of large, stable colloidal graphene quantum dots with tunable size. J Am Chem Soc 2010;132:5944-45.

[57] Shen JH, Zhu YH, Chen C. Facile preparation and upconversion luminescence of graphene quantum dots. Chem Commun 2011;47:2580-82.

[58] Welsher K, Liu Z, Daranciang D. Selective probing and imaging of cells

with single walled carbon nanotubes as near-infrared fluorescent molecules. Nano Lett 2008;:586-90.

[59] Sipkins DA, Cheresh DA, Kazemi MR. Detection of tumor angiogenesis *in vivo* by αvβ3-targeted magnetic resonance imaging. Nature Med 1998;4:623-26.

[60] Bonnemain B. Superparamagnetic Agents in magnetic resonance imaging: physicochemical characteristics and clinical applications a review. J Drug Targeting 1998;6:167-74.

[61] Hu WB, Peng C, Luo WJ. Min L, Li XM, Li D, Huang Q, Fan C. Graphene-based antibacterial paper. ACS Nano. 2010;4:4317-23.

[62] Liu SB, Zeng TH, Hofmann M, Burcombe W, Wei J, Jiang R, Kong J, Chen Y. Antibacterial activity of graphite, graphite oxide, graphene oxide, and reduced graphene oxide: membrane and oxidative stress. ACS Nano 2011;5:6971-80.

[63] Ryoo SR, Kim YK, Kim MH, Min DH. Behaviors of NIH-3T3 fibroblasts on graphene/carbon nanotubes: Proliferation, focal adhesion, and gene transfection studies. ACS Nano 2010;4:6587-98.

[64] Fan HL, Wang LL, Zhao KK. Li N, Shi ZJ, Ge ZQ, Jin ZX. Fabrication, mechanical properties, and biocompatibility of graphene-reinforced chitosan composites. Biomacromolecules 2010; 11: 2345-51.

[65] Nayak TR, Andersen H, Makam VS. Khaw C, Bae SK, Xu XF, Ee PLR, Ahn JH, Hong BH, Pastorin G, Ozyilmaz B. Graphene for controlled and accelerated osteogenic differentiation of human mesenchymal stem cells.

ACS Nano 2011;5:4670-78.

[66] Kalbacova M, Broz A, Kong J, Kalbac M. Graphene substrates promote adherence of human osteoblasts and mesenchymal stromal cells. Carbon 2010;48:4323-29.

[67] Shan CS, Yang HF, Han DX. Zhang QX, Ivaska A, Niu L. Water-soluble graphene covalently functionalized by biocompatible poly-L-lysine. Langmuir 2009;25:12030-33.

[68] Lei HZ, Mi LJ, Zhou XJ. Chen JJ, Hu J, Guo SW, Zhang Y. Adsorption of double-stranded DNA to graphene oxide preventing enzymatic digestion. Nanoscale 2011;3:3888-92.

[69] Zhang JL, Zhang F, Yang HJ. Huang XL, Liu H, Zhang JY, Guo SW. Graphene oxide as a matrix for enzyme immobilization. Langmuir 2010;2:6083-85.

[70] Zhang F, Zheng B, Zhang JL. Huang XL, Liu H, Guo SW, Zhang JY. Horseradish peroxidase immobilized on graphene oxide: physical properties and applications in phenolic compound removal. Phys Chem C 2010;114:8469-73.

[71] Dong HF, Gao WC, Yan F, Ji HX, Ju HX. Fluorescence resonance energy transfer between quantum dots and graphene oxide for sensing biomolecules. Anal Chem 2010;82:5511-17.

[72] Shen JF, Shi M, Li N, Yan B, Ma HW, Hu YZ, Ye MX. Facile synthesis and application of Ag-chemically converted graphene nanocomposite. Nano Res 2010;3:339-49.

[73] Bao H, Pan Y, Ping Y, Sahoo NG, Wu T, Li L, Li J, Gan LH. Chitosan-fucntionalized graphene oxideas a nanocarrier for drug and gene delivery. Small 2011,7:1569-78.

[74] Feng L, Zhang S, Liu Z. Graphene based gene transfection. Nanoscale 2011,3:1252-57.

[75] Zhang S, Yang K, Feng L, Liu Z. *In vitro* and *in vivo* behaviors of dextran functionalized graphene. Carbon 2011,49:4040-49.

[76] Sahu A, Choi WI, Lee JH, Tae G, Graphene oxide mediated delivery of methylene blue for combined photodynamic and photothermal therapy. Biomaterials 2013,34:6239-48.

[77] Huang P, Xu C, Lin J, Wang C, Wang X, Zhang C, Zhou X, Guo S, Cui D. Folic-acid-conjugated graphene oxide loaded with photosensitizers for targeting photodynamic therapy. Theranostics 2011,1:240-250.

[78] Hong H, Yang K, Zhang Y, Engle JW, Feng L, Yang Y, Nayak TR, Goel S, Bean J, Theuer CP, Barnhart TE, Liu Z, Cai W. *In vivo* targeting and imaging of tumor vasculature with radiolabeled antibody-conjugated nanographene. ACS Nano 2012,6:2361-70.

[79] Wu J, Wang YS, Yang XY, Liu YY, Yang JR, Yang R, Zhang N. Graphene oxide used as a carrier for adriamycin can reverse drug resistance in breast cancer cells. Nanotechnology 2012,23:355101.

[80] Hu H, Yu J, Li Y, Zhao J, Dong H. Engineering of a novel pluoronic F127/graphene nanohybrid for pH responsive drug delivery. J Biomed Mat Res A 2012,100:141-48.

[81] Wen H, Dong C, Dong H, Shen A, Xia W, Cai X, Song Y, Li X, Li Y, Shi D. Engineered redox-responsive PEG detachment mechanism in PEGyalted nano-graphene oxide for intracellular drug delivery. Small 2012,8:760-69.

[82] An J, Gou Y, Yang C, Hu F, Wang C. Synthesis of a biocompatible gelatin functionalized graphene nanosheets and its application for drug delivery. Mat Sci Eng C 2013,33:2827-37.

[83] Kakran M, Sahoo NG, Bao H, Pan Y, Li L. Functionalized graphene oxide as a nanocarrier of ellagic acid. Curr Med Chem 2011,18:4503-12.

[84] Kavitha T, Abdi SI, Park SY. pH-sensitive nanocargo based on smart polymer functionalization graphene oxide for site-specific drug delivery. Phys Chem Chem Phys 2013,15:5176-85.

[85] Fan X, Jiao G, Zhao W, Jin P, Li X. Fe_3O_4-graphene composites as targeted drug nanocarriers for pH-activated release. Nanoscale 2013,5:1143-52.

[86] Cho Y, Choi Y. Graphene oxide-photosensitizer conjugate as a redox-responsive theranostic agent. Chem Commun 2012,48:9912-14.

[87] Li F, Park SJ Ling D, Park W, Han JY, Na K, Char K. Hyaluronic acid-conjugated graphene oxide/photosensitizer nanohybrids for cancer targeted photodynamic therapy. J. Mat. Chem. B. 2013,1:1651-56.

[88] Zhou L, Wang W, Tang J, Zhou JH, Jiang HJ, Shen J. Graphene oxide noncovalent photosensitizer and its anticancer activity *in vitro*. Chemistry 2011,17:12084-91.

[89] Zhou L, Jiang H, Wei S, Ge X, Zhou J, Shen J. Highefficiency loading of hypocrellin B on graphene oxide for photodynamic therapy. Carbon 2012,50:5594-04.

[90] Trachootham D, Alexandre J, Huang P. Targeting cancer cells by ROS-mediated mechanisms: a radical therapeutic approach? Nat Rev Drug Discov 2009,8:579-91.

[91] Kam NWS, O'Cornell M, Wisdom JA, Dai H. Carbon nanotubes as multifunctional biological transporters and near-infrared agents for selective cancer cell destruction. Proc Natl Acad Sci 2005,102:11600-05.

[92] Huang X, EI-Sayed IH, Qian W, EI-Sayed MA. Cancer cell imaging and photothermal therapy in the near-infrared region by using gold nanorods. J Am Chem Soc 2006,128:2115-20.

[93] Iancu, C, Mocan L. Advances in cancer therapy through the use of carbon nanotube-mediated targeted hyperthermia. Inter J Nanomed 2011,6:1675-84.

[94] Choi WI, Kim JY, Kang C, Byeon CC, Kim YH, Tae G. Tumor regression *in vivo* by photothermal therapy based on gold-nanorod-loaded functional nanocarriers. ACS Nano 2011,5:1995-2003.

[95] Maltzahn GV, Park J, Agrawal A, Bandaru NK, Das SK, Sailor MJ, Bhatia SN. Computationally guided photothermal tumor therapy using long-circulating gold nanorod antennas. Cancer Res 2009,69:3892-3900.

[96] Weissleder R. A clearer vision for *in vivo* imaging. Nat Biotech

2001,19:316-17.

[97] Helmchen F, Denk W. Deep tissue two-photon microscopy. Nat Methods 2005,2:932-40.

[98] Welsher K, Liu Z, Sherlock SP, Robinson JT, Chen Z, Daranciang, Dai H. A route to brightly fluorescent carbon nanotubes for near-infrared imaging in mice. Nat Nanotechnol 2009,4:773-80.

[99] Yang K, Wan J, Zhang S, Tian B, Zhang Y, Liu Z. The influence of surface chemistry and size of nanoscale graphene oxide on photothermal therapy of cancer using ultra-low laser power. Biomaterials 2012,33:2206-14.

[100] Zedan AF, Moussa S, Terner J, Atkinson G, El-Shall, MS. Ultrasmall gold nanoparticles anchored to graphene and enhanced photothermal effects by laser irradiation of gold nanostructures in graphene oxide solutions. ACS Nano 2013,7:627-36.

[101] Lim DK, Barhoumi A, Wylie, RG, Reznor G, Langer RS. Kohane DS. Enhanced photothermal effect of plasmonic nanoparticles coated with reduced graphene oxide. Nano Lett 2013,13:4075-79.

[102] Zedan AF, Moussa S, Terner J, Atkinson G, El-Shall, MS. Ultrasmall gold nanoparticles anchored to graphene and enhanced photothermal effects by laser irradiation of gold nanostructures in graphene oxide solutions. ACS Nano 2013,7:627-36.

[103] Zhang L, Xia J, Zhao Q, Liu L, Zhang Z. Functional graphene oxide as a nanocarrier for controlled loading and targeted delivery of mixed

anticancer drugs. Small 2010;6:537-544.

[104] Zhang L, Lu Z, Zhao Q, Huang J, Shen H, Zhang Z. Enhanced chemotherapy efficacy by sequential delivery of siRNA and anticancer drugs using PEI-grafted graphene oxide. Small 2011;7:460-64.

[105] Zhi F, Dong H, Jia X, Guo W, Lu H, Yang Y, Ju H, Zhang X, Hu Y. Functionalized graphene oxide mediated adriamycin delivery and miR-21 gene silencing to overcome tumor multidrug resistance *in vitro*. Plos One 2013;8:e60034.

[106] Qin XC, Guo ZY, Liu ZM, Zhang W, Wan MM, Yang BW. Folic acid-conjugated graphene oxide for cancer targeted chemo-photothermal therapy. J Photochem Photobiol B 2013;120:156-62.

[107] Zhang L, Lu Z, Zhao Q, Huang J, Shen H, Zhang Z. Enhanced chemotherapy efficacy by sequential delivery of siRNA and anticancer drugs using PEI-grafted graphene oxide. Small 2011;7:460-64.

[108] Zhi F, Dong H, Jia X, Guo W, Lu H, Yang Y, Ju H, Zhang X, Hu Y. Functionalized graphene oxide mediated adriamycin delivery and miR-21 gene silencing to overcome tumor multidrug resistance *in vitro*. Plos One 2013;8:e60034.

[109] Zhang W, Guo Z, Huang D, Liu Z, Guo X, Zhong H. Synergistic effect of chemo-photothermal therapy using PEGylated graphene oxide. Biomaterials 2011,32:8555-61.

[110] Kim H, Lee D, Kim J, Kim TI, Kim WJ. Photothermally triggered cytosolic drug delivery via endosome disruption using a functionalized

reduced graphene oxide. ACS Nano 2013;7:6735-46.

[111] Tian B, Wang C, Zhang S, Feng L, Liu Z. Photothermally enhanced photodynamic therapy delivered by nano-graphene oxide. ACS Nano 2011;5:7000-09.

[112] Kelkar SS, Reineke TM. Theranostics: Combining imaging and therapy. Bioconjug. Chem 2011;22:1879-1903.

[113] Mura S, Couvreur P. Nanotheranostics for personalized medicine. Adv Drug Del Rev 2012;64:1394-1416.

[114] Chen Z, Ma L, Liu Y, Chen C. Applications of functionalized fullerenes in tumor theranostics. Theranostics 2012;2:238-50.

[115] Zhang Y, Nayak, TR, Hong H, Cai W. Graphene: A versatile nanoplatform for biomedical applications. Nanoscale, 2012;4:3833-42.

[116] Yang K, Zhang S, Zhang G, Sun X, Lee ST, Liu Z. Graphene in mice: ultrahigh *in vivo* tumor uptake and efficient photothermal therapy. Nano Lett 2010;10:3318-23.

[117] Yang K, Hu L, Ma X, Ye S, Cheng L, Shi X, Li C, Li Y, Liu Z. Multimodal imaging guided photothermal therapy using functionalized graphene nanosheets anchored with magnetic nanoparticles. Adv Mat 2012;24:1868-72.

[118] Shi X, Gong H, Li Y, Wang C, Cheng L, Liu Z. Graphenebased magnetic plasmonic nanocomposite for dual bioimaging and photothermal therapy. Biomaterials 2013;34:4786-93.

[119] Wang Y, Huang R, Liang, G, Zhang Z, Zhang P, Yu S, Kong J.

MRI-visualized, dual-targeting, combined tumor therapy using magnetic graphene-based mesoporous silica. Small. 2014;10:109-16.

[120] Jin Y, Wang J, Ke H, Wang S, Dai Z. Graphene oxide modified PLA microcapsules containing gold nanoparticles for ultrasonic/CT bimodal imaging guided photothermal tumor therapy. Biomaterials 2013;34:4794-02.

[121] Sheng Z, Song L, Zheng J, Hu D, He M, Zheng M, Gao G, Gong, P, Zhang P, Ma Y, Cai L. Protein-assisted fabrication of nano-reduced graphene oxide for combined *in vivo* photoacoustic imaging and photothermal therapy. Biomaterials 2013; 34:5236-43.

[122] Wang C, Ravi S, Garapati, US, Das M, Howell M, Mallela J.; Alwarappan S, Mohapatra SS, Mohapatra S. Multifunctional chitosan magnetic-graphene (CMG) nanoparticles: A theranostic platform for tumor-targeted co-delivery of drugs, genes and MRI contrast agents. J Mat Chem B 2013;1:4396-4405.

[123] Chang HX, Tang LH, Wang Y, Jiang JH, Li JH. Graphene fluorescence resonance energy transfer aptasensor for the thrombin detection. Anal Chem 2010;82:2341–46.

[124] Lu CH, Yang HH, Zhu CL, Chen X, Chen GN. A graphene platform for sensing biomolecules. Angew Chem Int Ed 2009; 48:4785–87.

[125] Wen Y, Xing F, He S. A graphene-based fluorescent nanoprobe for silver(I) ions detection by using graphene oxide and a silver-specific oligonucleotide. Chem Commun (Camb) 2010;46:2596–98.

[126] Du D, Zou ZX, Shin YS. Sensitive immunosensor for cancer biomarker based on dual signal amplification strategy of graphene sheets and multienzyme functionalized carbon nanospheres. Anal Chem 2010;82:2989–95.

[127] Xu CH, Wang XB, Wang JC, Hu HT, Wan L. Synthesis and photoelectrical properties of b-cyclodextrin functionalized graphene materials with high bio-recognition capability. Chem Phys Lett 2010; 498:162–67.

[128] Gulbakan B, Yasun E, Ibrahim SM. A dual platform for selective analyte enrichment and ionization in mass spectrometry using aptamer-conjugated graphene oxide. J Am Chem Soc 2010; 132:17408–10.

Chapter II

Safety and tumor tissue accumulation of pegylated graphene oxide nanosheets for co-delivery of anticancer drug and photosensitizer

1. Introduction

Recently, graphene-based materials have drawn considerable attention for their potential in biomedical applications. Graphene, a single or few-layered two-dimensional sp^2-bonded carbon sheet, is a basic building block of other carbon allotropes [1, 2]. Among the graphene-based materials, graphene oxide (GO) is a water-soluble derivative of graphene that has been studied as a potential material for nanomedicine, owing to its abundant functional groups (epoxide, hydroxyl and carboxyl groups) and the availability of its large planar surface area for efficient loading of aromatic drug molecules via π-π stacking. However, a lack of aqueous stability has limited the use of GO in biomedical applications to date.

To improve the aqueous stability of GO, polyethylene glycol (PEG)-grafted GO (pGO) nanosheets have been studied as a nanocarrier of anticancer drugs such as doxorubicin (Dox) and camptothecin derivatives [3, 4]. Despite the potential of pGO for drug nanocarriers, the tolerable dose of pGO and its safety relative to GO have not been fully explored.

For photodynamic therapy, photosensitizers have been delivered using nanocarriers such as liposomes and solid lipid nanoparticles [5, 6]. Only a few studies have examined the use of GO based materials for the delivery of photosensitizers. For example, the photosensitizer, hypocrellin A, was loaded onto GO by physisorption, and the feasibility of this hybrid for photodynamic therapy was tested *in vitro* [7]. In addition, the photosensitizer, chlorin e6 (Ce6), was loaded onto pGO, and the photodynamic anticancer effects were tested *in vitro* [8].

However, further *in vivo* distribution and efficacy studies are needed to validate the potential of GO-based materials for the delivery of photosensitizers.

In this chapter, we synthesized GO and pGO nanosheets and compared their *in vitro* cytotoxicity and *in vivo* safety. Next, we tested whether a Ce6-pGO nanophysisorplex (defined as a nanocomplex between drugs and pGO nanosheets derived by physicochemical adsorption) could be delivered to tumor tissues, as assessed by *in vivo* imaging in mice. Moreover, we evaluated the synergistic photodynamic effects of Ce6- and Dox-dual loaded pGO nanophysisorplexes in tumor-bearing mice.

2. Materials and methods

2.1. Preparation of GO and pGO nanosheets

The synthesis schemes of GO and pGO nanosheets were summarized in Fig. II-1. GO nanosheets were prepared from graphite using Hummers' method with slight modification [9]. Briefly, graphite powder (0.5 g, Sigma-Aldrich, St. Louis, MO, USA) was added to cold H_2SO_4 (23 ml), and then gradually stirred with $KMnO_4$ (3 g) and NaNO3 (0.5 g) on ice. The resulting mixture was further stirred at 35 ^oC for 1 h. Subsequently, 46 ml of distilled water was added and the temperature was increased to 90^oC and maintained for 1h. The reaction was stopped with 140 ml of distilled water and 10 ml of 30% H_2O_2. The reaction products were washed by repeated centrifugation, first with an aqueous 5% HCl solution, and then with distilled water. Finally, the products (200 mg) were dispersed in 40 ml of distilled water and sonicated at 400W (SonicVCX500, Sonics&Materials, Inc, Newtown, CT, USA) for 2 h to exfoliate the GO layers and form GO nanosheets. The unexfoliated GO was removed by centrifugation at 1600 g for 10 min. The supernatant containing GO nanosheets was collected and an extruder (Northern Lipid, British Columbia, Canada) was used to filter it through 0.2-μm polycarbonate membrane filters (Millipore Corp., Billerica, MA, USA).

To generate pGO nanosheets, the surfaces of the GO nanosheets were modified with PEG to increase their aqueous stability. In brief, N-(3-dimethylaminopropyl-N'-ethylcarbodiimide) hydrochloride (5 mM, Sigma-Aldrich) and N-hydroxysulfosuccinimide sodium (5 mM, Sigma-Aldrich)

were added to the GO nanosheets (1 mg/ml) in distilled water to activate the carboxyl groups in GO, and stirred for 24 h at room temperature. Then, 5 mM of NH_2-PEG (Mw2000; NOF, Tokyo, Japan) was added and the mixture was stirred for 24 h at room temperature. Unreacted NH_2-PEG and excess salts were removed by dialysis (MWCO 100K; Spectrum Laboratories, Inc., Rancho Dominguez, CA, USA) against distilled water for 2 days with 4 changes of distilled water at 12 h interval. The presence of functional groups in GO and pGO nanosheets was confirmed by FT-IR spectrometry (Nicolet 6700, Thermo Fisher Scientific, Inc., Waltham, MA, USA). The topography and thickness of pGO nanosheets were measured using atomic force microscopy (AFM, XE-150, PSIA Inc., Santa Clara, CA, USA) in non-contact mode. The AFM sample was prepared by dropping 20 μl of pGO (10 mg/ml) in distilled water onto Si substrate covered with SiO_2, and left at room temperature for 1 h to allow the adhesion of pGO onto substrate surface. The sample was then dried under N_2 gas fluid, and observed under AFM.

2.2. Loading of photosensitizer and anticancer drugs onto pGO nanosheets

Photosensitizers and anticancer drugs were sequentially loaded onto pGO nanosheets. The photosensitizer, Ce6 (Frontier Scientific Inc., West Logan, UT, USA) was loaded onto pGO nanosheets by adding 0.1 ml of Ce6 (10 mM in dimethyl sulfoxide) to 2 ml of pGO nanosheets dispersed in distilled water at a concentration of 1 mg/ml. The mixture was stirred overnight, and then the dimethyl sulfoxide was eliminated by dialysis against distilled water. After dialysis,

the unloaded Ce6, which precipitated in the distilled water, was removed by centrifugation at 1600× g for 10 min. Next, 0.2 mg of Dox (Sigma-Aldrich) was added to either 1 ml of pGO (1 mg/ml) to produce doxorubicin-loaded pGO (Dox/pGO), or 1 ml of Ce6-complexed pGO nanosheets (Ce6/pGO, 1 mg/ml) to produce Dox and Ce6 dual-loaded pGO (Ce6/Dox/ pGO) nanosheets. Free Dox was removed with a Sephadex G-25M column (PD-10 Column; GE Healthcare, Buckinghamshire, UK). The contents of Ce6 and Dox on the pGO nanosheets were determined by UV/Vis spectrometry at 662 nm and 400 nm, respectively.

2.3. Characterization of drug-loaded pGO nanosheets

The sizes of pGO nanosheets with or without drugs were determined using dynamic light scattering (DLS). The samples were diluted with distilled water and placed in an ELS-8000 instrument (Photal, Osaka, Japan). The hydrodynamic diameters were measured by He-Ne laser (10 mW) light scattering at an angle of 90^{o} at 24.1 ^{o}C. Zeta potential values of GO or pGO with or without drug loading were determined by laser Doppler microelectrophoresis at an angle of 22^{o} using an ELS-8000 instrument (Photal, Osaka, Japan). The fluorescent spectra of free Ce6, Dox, Ce6/pGO, Dox/pGO and Ce6/Dox/pGO were recorded by fluorometry under 400nm excitation for Ce6 and 485nm excitation for Dox.

2.4. Cellular uptake of Ce6 delivered by pGO nanosheets

Cellular uptake of Ce6 was studied using confocal microscopy. SCC7 cells were seeded onto cover glasses at a density of 8×10^{4} cells/well (Fisher Scientific)

in 24-well plates. When the cells reached 70% confluence, Ce6 in free form or loaded onto pGO nanosheets at a concentration of 20 μM were added to each well. After 1 h, the cells were fixed with 4% paraformaldehyde in phosphate buffered saline for 15 min, and then stained with 4',6-diamidino-2-phenylindole dihydrochloride (DAPI). The fixed cells were observed using a confocal laser-scanning microscope (LSM 5 Exciter; Carl Zeiss, Inc., Jena, Germany). For quantitation, the cells were harvested, washed three times with phosphate-buffered saline, and evaluated by flow cytometry using a BD FACS Calibur system and Cell Quest Pro analysis software (BD Bioscience, San Jose, CA, USA).

2.5. Evaluating the synergistic antitumor effects of Ce6 and Dox

The synergistic anticancer activity of dual drug-loaded pGO nanosheets was tested using the 3-(4,5-dimethylthiazol-2-yl)-2,5- diphenyltetrazolium bromide (MTT) cell viability assay. SCC7 cells were seeded to 48-well plates at a density of 8×10^4 cells/well. The following day (at ~70% confluence), each well was treated with various concentrations of Ce6 or Dox. For the dose-reduction index assay, wells were co-treated with Dox and Ce6 at molar ratios of 1:2, 1:4 or 1:8. After 24h, the cell culture medium was replaced with fresh medium to eliminate potential artifacts associated with the presence of residual Ce6. For drug-loaded pGO, the cells were treated for 0.5 h, and culture medium was replaced with fresh medium to eliminate the excess amounts of drug-loaded pGO. The cells were then exposed to a 660 nm light-emitting diode (LED) (Mikwang Electronics, Busan, South Korea) with a luminous intensity of 8000 mCd for 30 min. For MTT assays,

20 μl of MTT solution (5 mg/ml) was added to each well. After 2 h incubation, the culture medium was removed and 200 μl of a 0.04 N HCl/isopropanol solution was added. The reduction of MTT to its insoluble formazan product (indicating viable cells) was measured colorimetrically at 570 nm using an enzyme-linked immunosorbent assay reader (Sunrise-Basic TECAN, Männedorf, Switzerland). The cell viability in each group was expressed as a percentage of that in control cells. The synergism of Ce6 and Dox together was evaluated using the Calcusyn software (Biosoft, Cambridge, UK) [10].

2.6. Cytotoxicity of GO and pGO nanosheets

The cytotoxicities of GO and pGO nanosheets were tested using the MTT assay. Murine SCC7 squamous carcinoma cells were purchased from the American Type Culture Collection (Rockville, MD, USA) and cultured in Dulbecco's modified Eagle medium (Gibco BRL Life Technologies, Carlsbad, CA, USA) supplemented with 10% fetal bovine serum and 100 units/ml penicillin plus 100 mg/ml streptomycin in 5% CO_2 at 37 ^{o}C in a humidified incubator. For cell viability measurement, SCC7 cells were seed to 48-well plates at a density of 6×10^4 cells/well. After overnight incubation, cells were exposed to various concentrations of GO or pGO nanosheets for 1, 2, and 3 days. The viabilities of the treated cells were measured by MTT assay, as described above.

2.7. Animals

For the various experiments, 5-week-old female Balb/c and athymic nude

mice, as well as 7-week-old female C3H/HeN mice, were obtained from Orient Bio, Inc. (Seongnam, South Korea). All animals were maintained and used in accordance with the Guidelines for the Care and Use of Laboratory Animals of the Institute of Laboratory Animal Resources, Seoul National University.

2.8. *In vivo* acute toxicity tests of GO and pGO nanosheets

For *in vivo* acute toxicity evaluation, GO or pGO nanosheets were dispersed in 5% glucose solution and intravenously injected into the tail veins of healthy female Balb/c mice (Orient Bio, Inc.). Their survival at 24 h post-injection was recorded (n =10).

2.9. *In vivo* molecular imaging

The *in vivo* biodistribution of Ce6 to tumor tissues was tested by molecular imaging. Five-week-old athymic nude mice (Orient Bio, Inc.) were subcutaneously inoculated in the dorsal left side with 1×10^6 SCC7 cells, and tumors were allowed to become established over time. When the tumor volume reached 100 mm^3, Ce6 (10 mg/kg) was intravenously administered in free form or on pGO nanosheets. After 1, 24, and 48 h, the delivery efficiency of Ce6 was assessed using a Xenogen IVIS-200 system (Perkin Elmer Inc., Waltham, MA, USA) with the built-in Cy5.5 filter set.

2.10. *In vivo* photodynamic anticancer activity test

The photodynamic anticancer effects of Ce6 alone or combination with Dox

on pGO nanosheets were tested using SCC7-bearing mice. C3H/HeN mice (7-week-old, male; Orient Bio, Inc.) were subcutaneously injected in the dorsal left side with 1×10^6 SCC7 cells. When the tumor volume reached 100 mm^3, the mice were subjected to intravenous administration of Ce6/Dox/pGO. For systemic injection, mice were treated with pGO nanosheets alone (40 mg/kg), 10 mg/kg of Ce6 on pGO, 5 mg/kg of Dox on pGO, or with 10 mg/kg of Ce6 and 5 mg/kg of Dox on pGO every 3 days beginning on day 7, for a total of five injections. One hour post-administration, the mice were anesthetized, positioned in a mouse holder, and illuminated with 660 nm for 30 min using a LED lamp at a distance of 5 cm, as previously described [5]. The mouse holder had a 10-mm-diameter hole positioned over the tumor site, and all other areas were covered with aluminum foil to minimize the exposure of mice to LED light. To study the photodynamic anticancer efficacy, tumor tissues were extracted on day 29, and sections were subjected to hematoxylin and eosin staining.

2.11. Statistics

ANOVA was used to analyze experimental data with a Student-Newman-Keuls test for post-hoc pairwise comparisons. All statistical analyses were done using the SigmaStat software (version 3.5, Systat Software, Richmond, CA, USA), and a p-value < 0.05 was considered significant.

3. Results

3.1. Preparation and safety of GO and pGO nanosheets

GO nanosheets were generated from graphite using Hummers' method [9], and used to synthesize pGO nanosheets. Exfoliated GO nanosheets generated were turned into pGO nanosheets by the addition of PEG via amide formation between the –COOH group on the GO nanoparticle surface and the $–NH_2$ group of NH_2-PEG. The existence of the appropriate functional groups was confirmed by analysis of FT-IR spectra (Fig. II-1). Unlike graphite (Fig. II-1A), GO nanosheets (Fig. II-1B) have –OH (broad peak from 3000 cm^{-1}~3600 cm^{-1}), C=O (1719 cm^{-1}) and C=C (1580 cm^{-1}) functional groups [11]. For the pGO nanosheets (Fig. II-1C), the amide linkage of PEG to GO was confirmed by the CH_2 vibrations (~2900 cm^{-1}) of the PEG molecule, and a characteristic NH-CO stretching vibration (~1627 cm^{-1}).

The biocompatibilities of GO and pGO nanosheets were similar *in vitro* but differed substantially *in vivo*. Our *in vitro* cytotoxicity studies showed that after 24 h of treatment with 40 μg/ml of nanosheets, the viability was 92.8 ± 6.8 % for cells treated with pGO nanosheets and 86.7 ± 4.2 % for cells treated with GO nanosheets, which was not significantly different (Fig. II-2A). However, our *in vivo* experiments showed that pGO nanosheets were far less toxic than GO nanosheets (Fig. II-2B). The survival rate of mice was 20% after an intravenous bolus injection with GO nanosheets at a dose of 40 mg/kg, and decreased to 10% at 80 mg/kg. In contrast, mice injected with pGO nanosheets showed 100% survival

at a dose of 80 mg/kg.

3.2. Physicochemical characterization of drug-loaded pGO nanophysisorplexes

Loading of Dox or Ce6 did not significantly affect the mean size of the pGO nanosheets. The AFM analysis revealed that thickness of pGO nanosheets was found to 1 nm (Fig. II-3B). The size of Ce6/Dox/pGO nanophysisorplexes in which pGO nanosheets were complexed to Dox and Ce6 was 148 ± 18 nm (Fig. II-3C). Similarly, the polydispersity index values were not affected by drug loading onto pGO nanosheets (0.21 ± 0.02 for pGO nanosheets and 0.23 ± 0.01 for Ce6/Dox/pGO nanophysisorplexes). Based on the fluorescence quenching property of graphene [12], the loading of Dox and Ce6 onto pGO nanosheets was confirmed by fluorescence spectroscopy. In the case of the Ce6/pGO nanosheets, the fluorescence intensity of Ce6 loaded onto pGO was highly quenched when compared to an equivalent concentration of free Ce6 (Fig. II-3D). Similarly, the fluorescent intensity of Dox was substantially quenched upon loading onto pGO nanosheets (Fig. II-3E). The loading efficiencies of Ce6 and Dox onto pGO nanosheets were 51.9 ± 5.1 % and 61.7 ± 4.4 %, respectively. The loading of Dox and Ce6 onto pGO nanosheets was supported by the alteration of zeta potential values (Fig. II-3F). The zeta potential of pGO nanosheets (–41.5 ± 0.2 mV) was slightly decreased after Ce6 loading, but increased upon Dox loading. In the case of Ce6/Dox/pGO nanosheets, the zeta potential was (–42.6 ± 5.8 mV) similar to the value of pGO nanosheets.

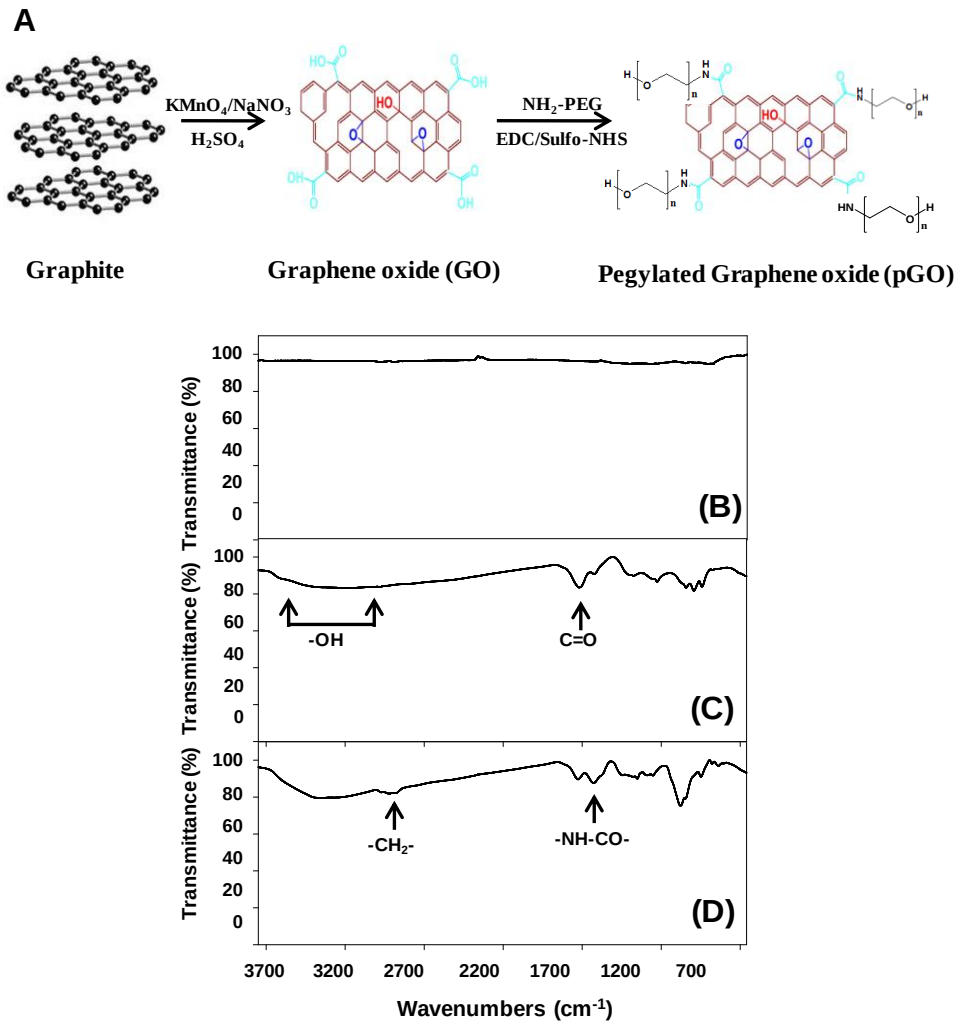

Fig. II-1. Synthesis schemes and FT-IR spectra of GO and pGO nanosheets.

Synthesis schemes for GO and pGO nanosheets (A). The chemical structures of graphite (B), GO (C) and pGO (D) were analyzed by infrared spectroscopy.

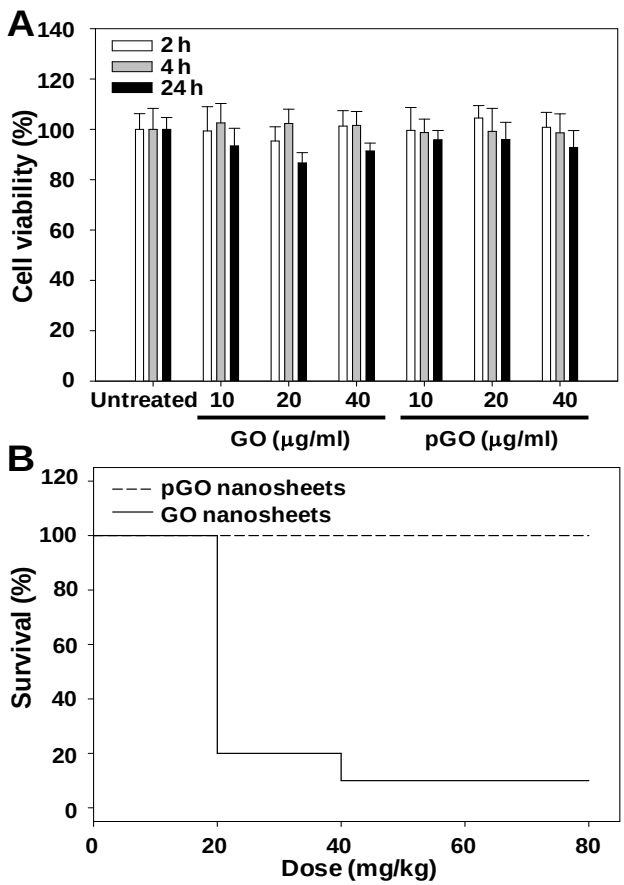

Fig. II-2. Cytotoxicity and *in vivo* safety of GO and pGO nanosheets.

(A) SCC7 cells were treated with various concentrations of GO or pGO nanosheets. After incubations for various periods, cell viability was measured by MTT assay. The results are the mean ± SE of four independent experiments. (B) Balb/c mice were intravenously injected with various doses of GO or pGO nanosheets (n = 10), and survival was assessed 1 day later.

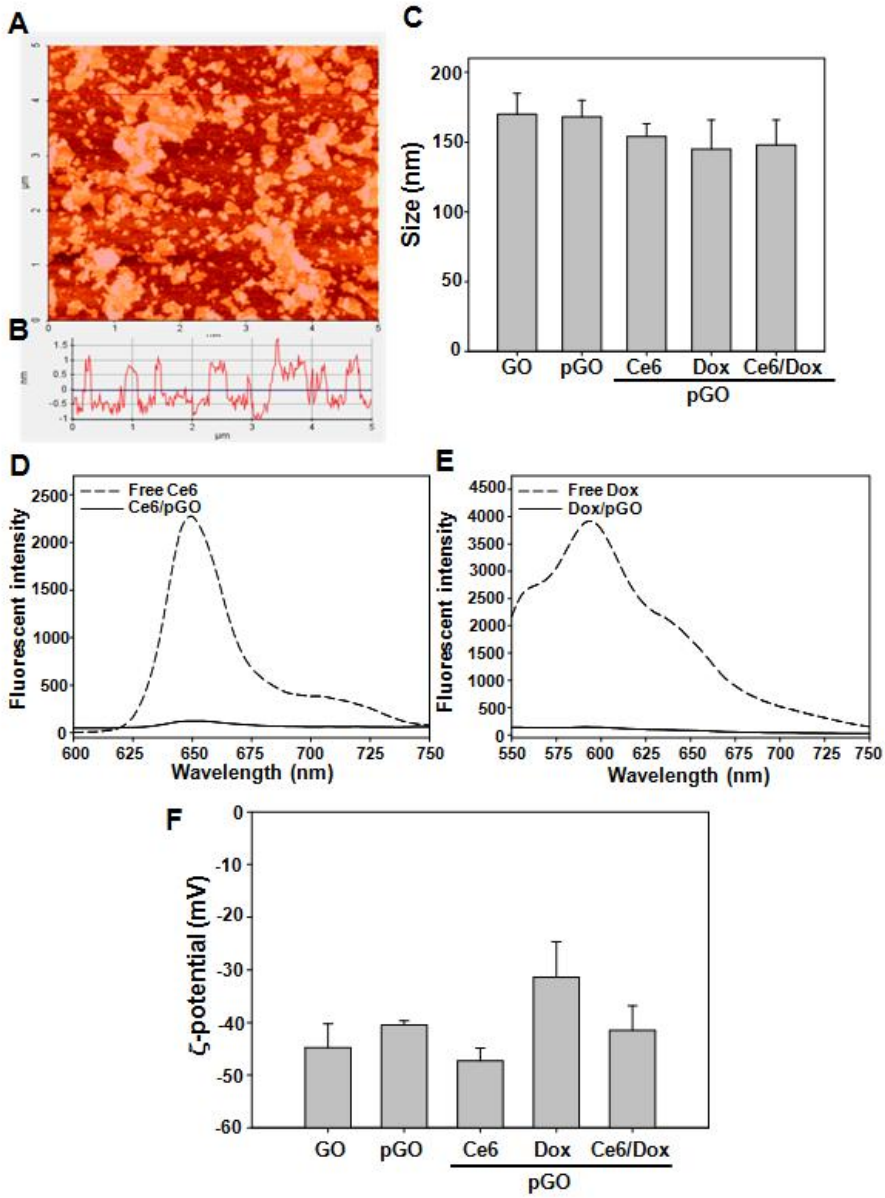

Fig. II-3. Characterization of pGO and nanophysisorplexes.

The AFM topography (A) and thickness (B) of pGO nanosheets are presented. (C) The sizes of GO, pGO, Ce6/pGO, Dox/pGO, and Ce6/Dox/pGO were measured by dynamic light scattering. Ce6 or Dox was complexed with pGO by π-π interaction.

Interactions between pGO and drugs were analyzed by fluorescent spectroscopy as compared with free Ce6 (D) or Dox (E). The zeta potentials (F) of GO, pGO, Ce6/pGO, Dox/pGO, and Ce6/Dox/pGO were observed by laser Doppler microelectrophoresis.

3.3. Enhanced cellular uptake of Ce6 delivered by pGO nanosheets

To examine the cellular delivery of Ce6, cell nuclei were stained with DAPI and fluorescence was assessed. Confocal microscopy revealed that untreated cells (Fig. II-4A) and those treated with plain pGO nanosheets (Fig. II-4B) showed no significant fluorescence in the cytoplasm. Cells treated with free Ce6 (Fig. II-4C) showed low levels of red fluorescence (representing Ce6) in the cytoplasm, whereas cells treated with Ce6/pGO (Fig. II-4D) clearly showed red fluorescence in the cytoplasm. This increased cellular delivery of Ce6 by pGO nanosheets was confirmed by flow cytometry (Fig. II-4E), in which 96.2 ± 1.7 % of cells treated with Ce6 on pGO nanosheets were Ce6-positive.

3.4. The anticancer synergism of Ce6 and Dox together

To examine the potential synergistic anticancer effects of Ce6 and Dox together *in vitro*, we first examined the dose-response profiles of each drug alone in SCC7 cells (Fig. II-5A). The doses capable of providing a 50% cancer cell-killing effect (ED_{50}) for Ce6 and Dox were 6.6 μM and 1.2 μM, respectively (Fig. II-5A). Co-treatment of cells with Dox and Ce6 at molar ratios of 1:2, 1:4, and 1:8 provided difference combination index (CI) values, which were calculated by the Chou-Talalay method [13]. CI values were calculated for ED_{50}, a dose providing a 75% cancer cell-killing effect (ED_{75}), and a dose providing a 90% cancer cell-killing effect (ED_{90}). The results calculated for ED_{90} revealed that co-treatment with Dox and Ce6 at a molar ratio of 1:8 had a CI value of 1.013, indicating that there was no synergism at this dose (Fig. II-5B). For all other doses,

however, the CI values ranged from 0.3 to 0.7, indicating the presence of strong synergism. The Dox-to-Ce6 molar ratio of 1:2 yielded the lowest CI values for ED_{50}, ED_{75}, and ED_{90} (Fig. II-5B). Based on these findings, we conclude that Dox and Ce6 had synergistic effects, and we selected the Dox-to-Ce6 ratio of 1:2 for use in subsequent experiments.

3.5. *In vitro* anticancer effects of Ce6/Dox/pGO nanophysisorplexes

We next examined whether the photodynamic anticancer effects after LED illumination could be enhanced by the co-delivery of Dox and Ce6 by pGO nanosheets. SCC7 cells were treated with Ce6/pGO, Dox/pGO, or Ce6/Dox/pGO. To evaluate the photodynamic anticancer effects, the survival of cancer cells in each group was compared in the absence and presence of LED illumination. In the absence of illumination, no significant photodynamic anticancer effect was observed in any group (Fig. II-5C). Following illumination with 660 nm LED light, Ce6/pGO-treated cells showed significantly lower survival compared to the non-illuminated group. In contrast, Dox/pGO-treated cells did not show survival differences with or without illumination. Ce6/Dox/pGO nanophysisorplexes did not exert any anticancer effect in the absence of light illumination. Following illumination, however, the Ce6/Dox/pGO nanophysisorplexes showed higher anticancer effects than the Ce6/pGO or Dox/pGO nanophysisorplexes (Fig. II-5C). Thus, our results indicate that the co-delivery of Dox and Ce6 by pGO nanosheets exert significantly higher photodynamic anticancer effects than the delivery of Ce6 alone by pGO nanosheets.

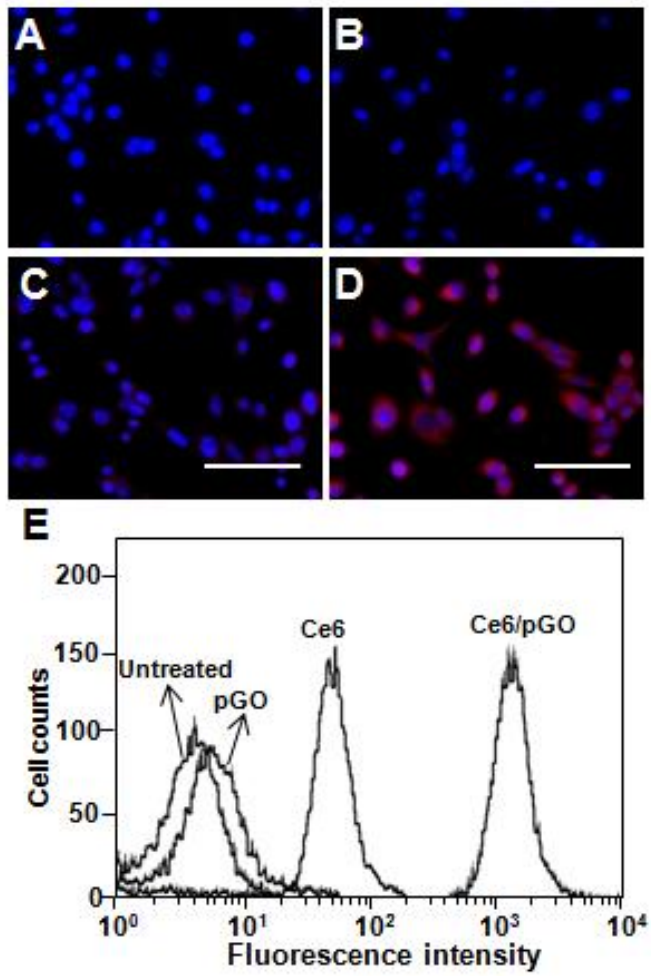

Fig. II-4. Cellular uptake of pGO nanophysisorplexes.

SCC7 cells were left untreated (A), or were treated with pGO alone (B), free Ce6 (C), or Ce6/pGO nanophysisorplexes (D). After incubation for 1 h, cellular fluorescence was observed by confocal microscopy and quantified by flow cytometry (E). Scale bar is 50 μm.

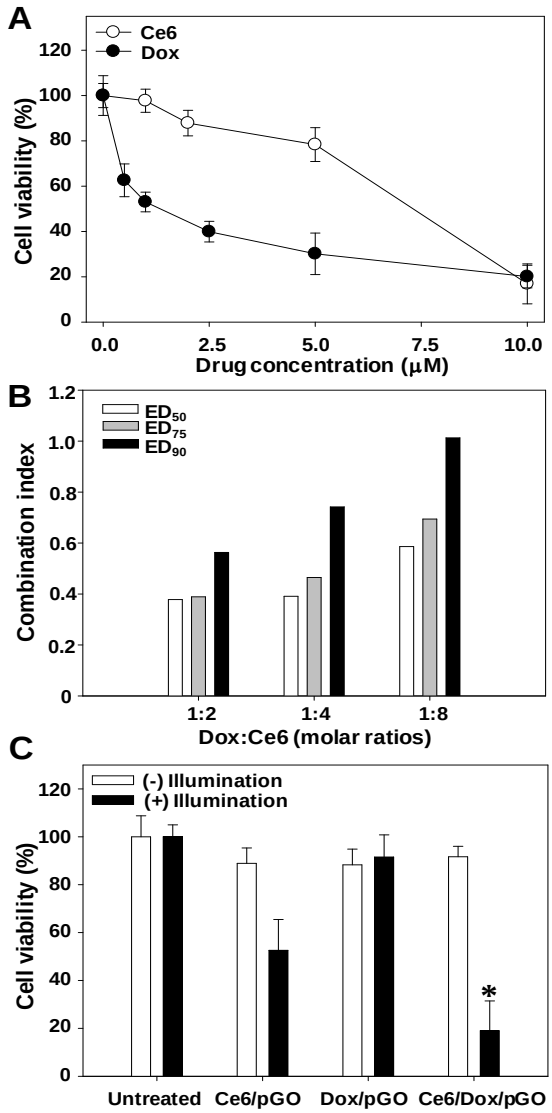

Fig. II-5. Synergistic anticancer effect of Ce6 and Dox combination *in vitro*.

SCC7 cells were co-treated with free Ce6 and Dox at various concentrations, and after 24 h, cell viability was measured by MTT assay (A). The results are the mean ± SE of four independent experiments. Based on the dose-response curves of Ce6

and Dox at various molar ratio combinations, the combination index values were calculated for ED_{50}, ED_{75}, and ED_{90} (B). SCC7 cells were treated with Dox (2.5 μM) and Ce6 (5.0 μM) in pGO nanophysisorplexes with or without illumination by a 660 nm LED light (C). After incubation for 0.5 h, cell viability was measured by MTT assay. The results are the mean ± SE of four independent experiments. *Significantly lower ($p < 0.05$) compared to the other groups (assessed by ANOVA and the Student-Newman-Keuls test).

3.6. Tumor tissue accumulation of pGO nanophysisorplexes

In tumor-bearing mice, pGO nanosheets showed higher distribution to tumor tissues. The biodistribution of Ce6/pGO nanosheets in mice was visualized using Ce6 fluorescence signals (Fig. II-6A-C). At 1 h (Fig. II-6A) after intravenous injection to SCC7 tumor-bearing mice, the Ce6/pGO signal was observed in tumor tissues and other organs. With increasing time, the retention of pGO in tumor tissues became notable. At 48 h post-injection (Fig. II-6C), the pGO signal was higher in tumor tissues than in other tissues. The delivery of Ce6 using pGO significantly enhanced the tumor retention as compared to free Ce6 at 48 h post-dose (Fig. II-6E).

3.7. *In vivo* photodynamic anticancer effects of Ce6 and Dox co-delivered by pGO nanophysisorplexes

We next examined whether the co-delivery of Ce6 and Dox via pGO nanophysisorplexes could potentiate the photodynamic antitumor activities in SCC7-bearing mice. The systemic co-delivery of Ce6 and Dox on pGO nanophysisorplexes provided the highest photodynamic anticancer effects (Fig. II-7A). There was no significant difference in the anticancer effects of Ce6/pGO and Dox/pGO, with the Ce6/pGO-treated group showing a 31% reduction in tumor volume on day 28. In contrast, the Ce6/Dox/pGO-treated group showed a 73% reduction in tumor volume compared to untreated mice on day 28. Hematoxylin-eosin staining showed that the tumor tissues of mice intravenously treated with pGO alone (Fig. II-7C), Ce6/pGO (Fig. II-7D), and Dox/pGO (Fig.

II-7E) had tumor cell nuclei similar to those seen in the untreated group (Fig. II-7B). In contrast, tumor tissue sections from mice systemically treated with Ce6/Dox/pGO contained tumor cells in which most of the cell nuclei had disappeared (Fig. II-7F).

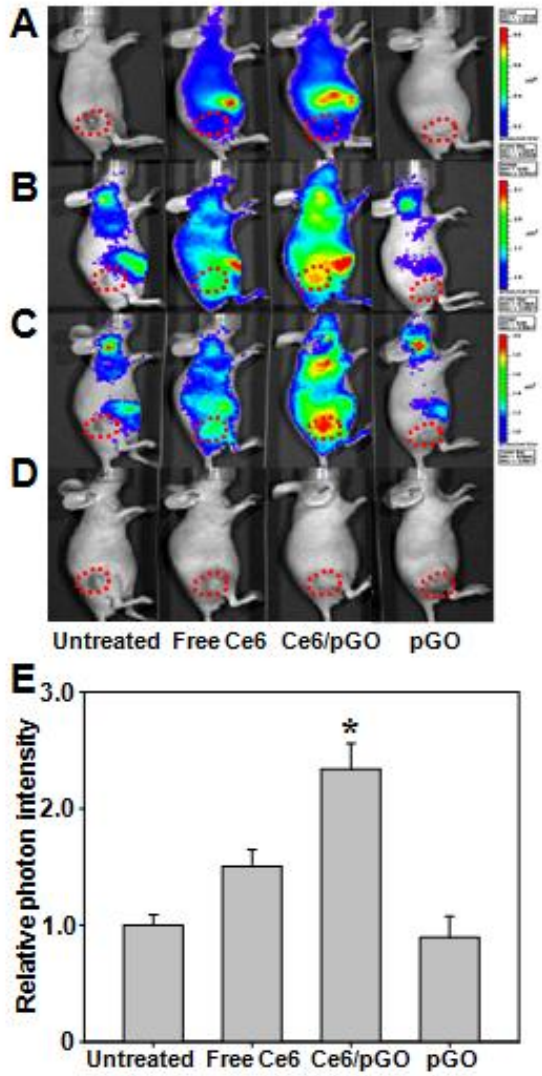

Fig. II-6. *In vivo* biodistribution of pGO nanophysisorplexes.

SCC7-bearing mice were systemically treated with pGO, free Ce6, Ce6/pGO, or with Ce6/Dox/pGO (Ce6 10 mg/kg and Dox 5 mg/kg). (A) After 1 h, 24 h and 48 h, the *in vivo* distributions of Ce6 fluorescence were visualized using a molecular

imaging system. (B) Relative photon counts of tumor sites in comparison with untreated group were quantitated at 48 post-dose by *in vivo* imaging system. *Significantly higher ($p < 0.05$) compared to the other groups (assessed by ANOVA and the Student-Newman-Keuls test).

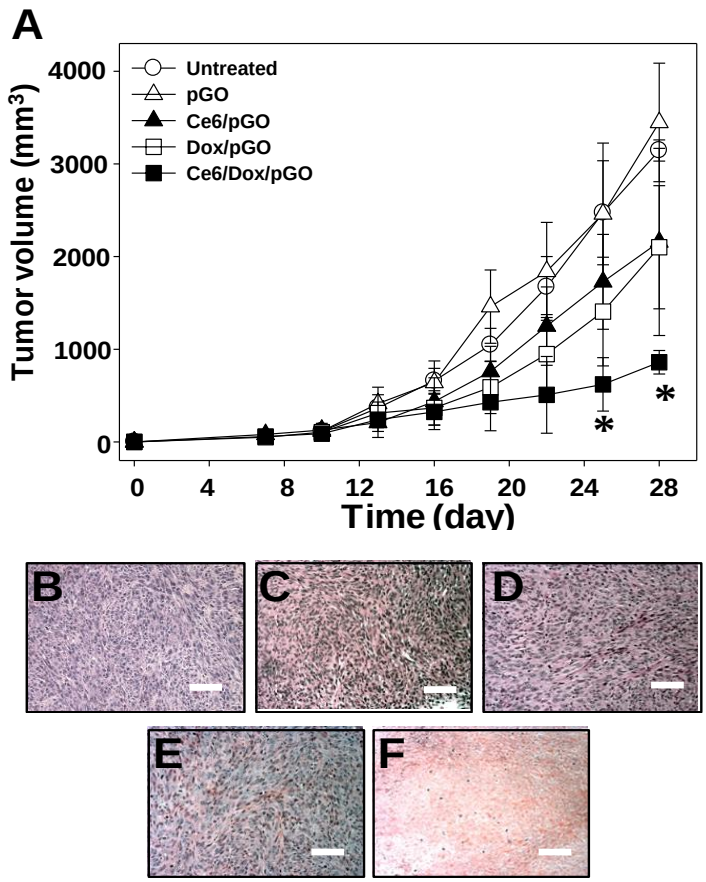

Fig. II-7. Photodynamic anticancer effects of pGO nanophysisorplexes.

SCC7-bearing mice were intravenously treated with pGO alone or in complexes with Ce6 (10 mg/kg), Dox (5 mg/kg), and Ce6/Dox/pGO every 3 days beginning on day 7. On day 29, tumor tissues were extracted and sectioned for hematoxylin and eosin staining (B, untreated; C, pGO; D Ce6/pGO; E, Dox/pGO; F, Ce6/Dox/pGO). Scale bar, 100 μm. *Significantly lower ($p < 0.05$) compared to the other groups (assessed by ANOVA and the Student-Newman-Keuls test).

4. Discussion

In this chapter, we demonstrated that pGO nanosheets can be used as co-delivery vehicles for chemotherapeutics and photosensitizers to enhance tumor localization and photodynamic antitumor therapeutic effects. We observed that pGO nanosheets increased the cellular uptake and tumor tissue accumulation of Ce6, compared to treatment with free drugs. Moreover, the pGO nanosheet-based co-delivery of Ce6 and Dox showed synergistic anticancer effects *in vitro* and *in vivo*.

Both Ce6 and Dox were loaded onto pGO nanosheets with loading efficiencies of more than 50%. Graphene and its derivatives can serve as carriers for many drugs due to their ultrahigh surface areas (~2600 m^2/g), and they have high loading capacities thanks to π-π stacking and/or hydrophobic interactions [14]. The high loading efficiencies of Dox and Ce6 onto pGO nanosheets might be attributed to the large aromatic structures of these drugs, which may enable π-π stacking and hydrophobic interactions with nanosheets surfaces. Previously, high loading of Dox was reported on carbon nanotubes and graphene oxide, and the loading of Ce6 onto graphene oxide was reported to occur via π-π stacking and hydrophobic interactions [8, 15-17].

Compared to GO nanosheets, pGO nanosheets showed a much higher safety in our acute toxicity test, with 100% of mice surviving at a dose of 80 mg/kg. Previously, only limited information was available regarding the toxicological profiles of graphene-based nanomaterials. Little or no cytotoxicity by GO

nanosheets has been reported in cell lines, such as L929 cells, A549 human lung cancer cells and human fibroblasts [18-20]. However, we herein found much higher survival among mice that received a single dose of pGO nanosheets compared to GO nanosheets. Such a higher safety of pGO might be due to the higher stability of PEG-coated nanosheets in serum and reduced aggregation in circulation. Consistent with this, a recent study reported that the *in vivo* safety of GO nanosheets could be improved by dextran functionalization [21].

Regarding the *in vivo* fate and potential toxicity of pGO, there is limited understanding. It has been reported that the *in vivo* behavior and toxicity of graphene family materials could be affected by physicochemical properties such as surface functional groups, hydrophobicity, charges, sizes, stiffness, and structural defects [22-24]. A recent study reported that radiolabelled pGO mainly accumulated in the liver and spleen after intravenous administration to mice [25]. The gradual discharge of pGO was observed in all organs over time, and the excretion of pGO was observed in both fecal and urine routes. Moreover, the study revealed that there was no sign of notable toxicity for 90 days by blood chemistry, hematological and histological examinations after a single intravenous dose of pGO at a dose of 20 mg/kg. In our study, we observed 100% survival of mice one day after intravenous administration of pGO up to 80 mg/kg. Although we evaluated the safety of pGO only focusing on the survival, it still needs to be tested whether pGO at 80 mg/kg dose could cause appreciable toxicity at long-term exposure. Moreover, the toxicity of pGO after repeated dosing should be studied in the future.

We observed inconsistency between AFM topography image and DLS size data of pGO nanosheets (Fig. II-3). Although DLS data (Fig. II-3C) showed polydispersity values of 0.21 ± 0.02 for pGO nanosheets, the AFM image (Fig. II-3A) revealed certain levels of heterogeneity. The discrepancy between two data might be in part due to the different detection technologies for two dimensional nanosheets rather than three dimensional nanoparticles. The AFM data reveal the thickness (Fig. II-3B) and 2 dimensional shapes of nanosheets (Fig. II-3A). In the AFM data (Fig. II-3B), the thickness was found to be nearly uniform size of 1 nm. Unlike AFM data, the DLS data could not give information on the thickness of 2 dimensional nanosheets, but provide the three dimensional and statistical mean values of pGO nanosheets.

Our *in vitro* cellular uptake data revealed that pGO nanosheets could enhance the delivery of Ce6 to cells. pGO nanosheets alone could be efficiently taken up by the cells (data not shown). The higher Ce6 fluorescence after delivery on pGO nanosheets and the cellular uptake of pGO nanosheets alone supports that the enhanced cellular Ce6 levels were mediated by pGO nanosheets. Recent studies reported that the extent [26] and kinetics [27] of pGO cellular uptake differed depending on cell types. The cellular uptake mechanisms for graphene nanosheets are not yet clearly known. Liu et al. previously reported that endocytosis is a likely mechanism for the cellular uptake of pGO nanosheets [4]. Using surface-enhanced Raman scattering spectroscopy, Huang and colleagues suggested that the internalization of GO by Ca Ski cells is mainly via clathrin-mediated endocytosis and energy-dependent process [28]. However, a recent controversial report based

on temperature-independent uptake patterns argued that the efficient uptake of pGO nanosheets by HeLa cells may rely on direct penetration of cell membranes rather than endocytosis [29]. A recent mechanism study using oxidized and pegylated graphene nanoribbons reported that the pegylated graphene nanoribbons entered HeLa cells via both endocytosis and macropinocytosis pathways [26]. The study showed that larger aggregates of pegylated graphene nanoribbons were taken up by the macropinocytotic pathway, whereas smaller aggregates were internalized by the endocytosis. Their transmission electron microscopy revealed the intracellular trafficking of internalized graphene nanoribbons in vesicular structures similar to early endosomes. Based on these previous findings, it is likely that the cellular internalization pathways of graphene family nanomaterials might be affected by the size and surface properties. The cellular internalization mechanisms of our pGO nanosheets need to be studied further. However, unlike the previous report of Peng et al. [29], we did not observe the temperature-independent efficient cellular uptake of pGO nanosheets in SCC7 cells (data not shown).

The cellular fluorescence signals of Ce6 that we observed after delivery on pGO nanosheets may indicate that Ce6 is liberated from pGO nanosheets in the cells, thereby recovering its own fluorescence. The intracellular trafficking of pGO to endosome-like vesicles was recently observed using transmission electron microscopy [26]. Given the rapid fusion kinetics of endosomes with lysosomes after endocytosis of nanoparticles [30], it is likely that the fusion may have occurred in 1 h after endocytosis. In the acidic lower pH of endolysosomes, the

negative charges of pGO may increase due to the carboxyl groups on pGO surfaces. The possible increase in the electrostatic repulsion between the negatively charged carboxyl groups on pGO and the anionic Ce6 might have promoted the liberation of Ce6 from pGO nanosheets, and resulted in dequenching effects.

We further examined the co-delivery of Dox to increase the photodynamic therapeutic effect of Ce6. Both combination and dose-reduction index values were used to select the ratio of Ce6 and Dox, and the combination index was used to evaluate synergism via dose-addition isobole analysis, a widely used approach for the assessment of pharmacodynamic drug interactions [31]. Recently, various nanocarriers have been studied for the co-delivery of Dox and photosensitizers. For example, multilayer polymeric capsules were studied as a co-delivery carrier for Dox and the photosensitizer, porphyrin [32]. Polymeric micelles entrapping a photosensitizer were reported to increase the therapeutic index of Dox in Dox-resistant tumor-bearing mice [33]. Furthermore, the use of alginate nanoparticles for the co-delivery of Dox and a photosensitizer was reported to enhance cellular delivery and inhibit the efflux of Dox, resulting in synergistic anticancer effects [34].

Unlike the previously reported polymeric micelles and alginate nanoparticles, pGO nanosheets may have a unique advantage, photothermal effect, for co-delivery of Dox with photosensitizer. Due to the strong optical absorbance of graphene in the NIR region, the graphene nanosheets can generate heat after near-infrared radiation, and exert anticancer effect. As compared to other carbon-based materials such as single-walled carbon nanotubes, graphene

nanosheets were shown to provide higher photothermal effect, and anticancer effect *in vitro* [35]. Graphene may exert the photothermal apoptotic and necrotic cell killing by oxidative stress and mitochondrial membrane depolarization [35]. A recent study reported the *in vivo* photothermal anticancer effect of pGO nanosheets in mice [36]. In the study, intravenously administered pGO nanosheets provided tumor ablation after low-power NIR laser irradiation on the tumor. The *in vivo* photothermal effects of graphene could be further optimized by modulating the surface chemistry and sizes. Yang and colleagues reported that ultra-small reduced pGO improved *in vivo* photothermal anticancer effects in mice [37]. Given the photothermal anticancer effects of pGO, the addition of photosensitizers and chemotherapeutics onto pGO may provide more effective anticancer treatment, which has not been achieved by other synthetic and natural polymeric nanocarriers.

Here, we found that the tumor accumulation of Ce6-loaded pGO nanosheets was higher than that of free Ce6 (Fig. II-4). The main driving force of tumor localization via pGO nanosheets is believed to be their enhanced permeability and retention in tumor tissues [38]. Our observations agree with a prior report of enhanced tumor distribution of pGO nanosheets in 4T1 and U87MG tumor-bearing mice 1 day after administration [37]. Unlike our observations and the cited report, however, Hong and colleagues reported that or ^{64}Cu-GO functionalized with multi-arm PEG had higher distributions to the liver than to 4T1 tumor tissues at 1 day after administration [39,40]. This discrepancy in the biodistribution patterns of PEG-functionalized nanosheets remains to be clarified, but we speculate that the use of linear or multi-arm PEG might affect the distribution of pGO.

We observed more effective photodynamic anticancer effects following the systemic co-delivery of Dox and Ce6 using pGO nanosheets, likely due to the higher tumor accumulation of the drugs via pGO nanosheets. Moreover, the enhanced cellular delivery of drugs observed in our *in vitro* cellular uptake study is likely to contribute to these increased anticancer effects. Finally, the combination of Ce6 with Dox at a synergistic ratio may contribute to the enhanced efficacy of photodynamic anticancer therapy. Although we co-delivered photosensitizers and chemotherapeutics in this study, pGO nanosheets should also be able to serve as multimodal nanocarriers, and the pGO nanoparticle-based co-delivery of photosensitizers with diagnostics may be applicable for theranostic development in the near future.

5. References

[1] Geim AK, Novoselov KS. The rise of graphene. Nat Mater 2007; 6:183-91.

[2] Avouris P, Chen Z, Perebeinos V. Carbon-based electronics. Nat Nanotechnol 2007; 2: 605-15.

[3] Sun X, Liu Z, Welsher K, Robinson JT, Goodwin A, Zaric S, Dai H. Nano-graphene oxide for cellular imaging and drug delivery. Nano Res 2008; 1: 203-12.

[4] Liu Z, Robinson JT, Sun X, Dai H. PEGylated nanographene oxide for delivery of water-insoluble cancer drugs. J Am Chem Soc 2008; 130: 10876-7.

[5] Shim G, Lee S, Kim YB, Kim CW, Oh YK. Enhanced tumor localization and retention of chlorin e6 in cationic nanolipoplexes potentiate the tumor ablation effects of photodynamic therapy. Nanotechnology 2011; 22: 365101.

[6] Youssef T, Fadel M, Fahmy R, Kassab K. Evaluation of hypericin-loaded solid lipid nanoparticles: physicochemical properties, photostability and phototoxicity. Pharm Dev Technol 2012; 17:177-86.

[7] Zhou L, Wang W, Tang J, Zhou JH, Jiang HJ, Shen J. Graphene oxide noncovalent photosensitizer and its anticancer activity *in vitro*. Chemistry 2011; 17: 12084-91.

[8] Tian B, Wang C, Zhang S, Feng L, Liu Z. Photothermally enhanced

photodynamic therapy delivered by nano-graphene oxide. ACS Nano 2011; 5: 7000-9.

[9] Hummers WS, Offeman RE. Preparation of graphitic oxide. J Am Chem Soc 1958;80: 1339.

[10] Yu YL, Su KJ, Chen CJ, Wei CW, Lin CJ, Yiang GT, et al. Synergistic anti-tumor actiuvity of isochaihulactone and paclitaxel on human lung cancer cells. J Cell Physiol 2012; 227: 213-22.

[11] Hontoria-Lucas C, López-Peinado AJ, López-González JdD, Rojas-Cervantes ML, Martín-Aranda RM. Study of oxygen-containing groups in a series of graphite oxides: physical and chemical characterization. Carbon 1995; 33:1585-92.

[12] Lu CH, Yang HH, Zhu CL, Chen X, Chen GN. A graphene platform for sensing biomolecules. Angew Chem Int Edit 2009; 48: 4785-7.

[13] Park BJ, Whichard ZL, Corey SJ. Dasatinib synergizes with both cytotoxic and signal transduction inhibitors in heterogeneous breast cancer cell lines – Lessons for design of combination targeted therapy. Cancer Lett 2012; 320: 104-10.

[14] Stoller MD, Park S, Zhu Y, An J, Ruoff RS. Graphene-based ultracapacitors. Nano Lett 2008; 8: 3498-502.

[15] Liu Z, Sun X, Nakayama-Ratchford N, Dai, H. Supramolecular chemistry on water-soluble carbon nanotubes for drug loading and delivery. ACS Nano 2007; 1: 50-6.

[16] Yang X, Zhang X, Liu Z, Ma Y, Huang Y, Chen Y. High-efficiency

loading and controlled release of doxorubicin hydrochloride on graphene oxide. J Phys Chem C 2008; 112: 17554-8.

[17] Huang P, Xu C, Lin J, Wang C, Wang X, Zhang C, et al. Folic acid-conjugated graphene oxide loaded with photosensitizers for targeting photodynamic therapy. Theranostics 2011; 1: 240-50.

[18] Wojtoniszak M, Chen X, Kalenczuk RJ, Wajda A, Lapczuk J, Kurzewski M. et al. Synthesis, dispersion, and cytocompatibility of graphene oxide and reduced graphene oxide. Colloid. Surface B 2012; 89:79-85.

[19] Chang Y, Yang ST, Liu JH, Dong E, Wang Y, Cao A. et al. H. *In vitro* toxicity evaluation of graphene oxide on A549 cells. Toxicol Lett 2011; 200: 201-10.

[20] Liao KH, Lin YS, Macosko CW, Haynes CL. Cytotoxicity of graphene oxide and grapene in human erythrocytes and skin fibroblasts. ACS Appl Mat Inter 2011; 3: 2607-15.

[21] Zhang X, Yin J, Peng C, Hu W, Zhu Z, Li W et al. Distribution and biocompatibility studies of graphene oxide in mice after intravenous administration. Carbon 2011; 49: 986-95.

[22] Sanchez VC, Jachak A, Hurt RH, Kane AB. Biological interactions of graphene-family nanomaterials: an interdisciplinary review. Chem Res Toxicol 2012; 25:15-34.

[23] Yang K, Li Y, Tan X, Peng R, Liu Z. Behavior and Toxicity of Graphene and Its Functionalized Derivatives in Biological Systems. Small 2013; 9:1492-503.

[24] Bussy C, Ali-Boucetta H, Kostarelos K. Safety considerations for graphene: lessons learnt from carbon nanotubes. Acc Chem Res 2013; 46: 692-701.

[25] Yang K, Wan J, Zhang S, Zhang Y, Lee ST, Liu Z. *In vivo* pharmacokinetics, long-term biodistribution, and toxicology of PEGylated graphene in mice. ACS Nano 2011; 5: 516-22.

[26] Mullick Chowdhury S, Lalwani G, Zhang K, Yang JY, Neville K, Sitharaman B. Cell specific cytotoxicity and uptake of graphene nanoribbons. Biomaterials 2013; 34: 283-93.

[27] Vila M, Portolés MT, Marques PA, Feito MJ, Matesanz MC, Ramírez-Santillán C, et al. Cell uptake survey of pegylated nanographene oxide. Nanotechnology 2012; 23: 465103.

[28] Huang J, Zong C, Shen H, Liu M, Chen B, Ren B, et al. Mechanism of cellular uptake of graphene oxide studied by surface-enhanced Raman spectroscopy. Small 2012; 8:2577-84.

[29] Peng C, Hu W, Zhou Y, Fan C, Huang, Q. Intracellular imaging with a graphene-based fluorescent probe. Small 2010; 6:1686-92.

[30] Oh YK, Swanson JA. Different fates of phagocytosed particles after delivery into macrophage lysosomes. J Cell Biol 1996; 132: 585-93.

[31] Loewe S. The problem of synergism and antagonism of combined drugs. Arzneimittel-Forsch 1953; 3:285-90.

[32] Son KJ, Yoon HJ, Kim JH, Jang WD, Lee Y, Koh WG. Photosensitizing hollow nanocapsules for combination cancer therapy. Angew Chem Int Edit 2011; 50:11968-71.

[33] Lu HL, Syu WJ, Nishiyama N, Kataoka K, Lai PS. Dendrimer phtahlocyanine-encapsulated polymeric micelle-mediated photochemical internalization extends the efficacy of photodynamic therapy and overcomes drug resistance *in vivo*. J Control Release 2011;155:458-64.

[34] Khdair A, Chen D, Patil Y, Ma L, Dou QP, Shekhar MP, et al. Nanoparticle-mediated combination chemotherapy and photodynamic therapy overcomes tumor drug resistance. J Control Release 2010;141: 137-44.

[35] Markovic ZM, Harhaji-Trajkovic LM, Todorovic-Markovic BM, Kepić DP, Arsikin KM, Jovanović SP, et al. *In vitro* comparison of the photothermal anticancer activity of graphene nanoparticles and carbon nanotubes. Biomaterials 2011; 32:1121-29.

[36] Yang K, Zhang S, Zhang G, Sun X, Lee ST, Liu Z. Graphene in mice: ultrahigh *in vivo* tumor uptake and efficient photothermal therapy. Nano Lett 2010; 10: 3318-23.

[37] Yang K, Wan J, Zhang S, Tian B, Zhang Y, Liu Z. The influence of surface chemistry and size of nanoscale graphene oxide on photothermal therapy of cancer using ultra-low laser power. Biomaterials 2012;33: 2206-14.

[38] Matsumura Y, Maeda H. A new concept for macromolecular therapeutics in cancer chemotherapy: mechanism of tumoritropic accumulation of proteins and the antitumor agent Smancs 1. Cancer Res 1986; 46: 6387-92.

[39] Hong H, Yang K, Zhang Y, Engle JW, Feng L, Yang Y, et al. *In vivo*

targeting and imaging of tumor vasculature with radiolabeled antibody-conjugated nanographene. ACS Nano 2012; 6: 2361-70.

[40] Hong H, Zhang Y, Engle JW, Nayak TR, Theuer CP, Nickles RJ. *In vivo* targeting and positron emission tomography imaging of tumor vasculature with ^{66}Ga-labeled nano-graphene. Biomaterials 2012; 33: 4147-56.

Chapter III

Cholesteryl hyaluronic acid-coated, reduced graphene oxide nanosheets for anticancer drug delivery

1. Introduction

Graphene-based nanosheets have drawn considerable recent attention as a new material for biomedical applications. Because of their mechanical, thermal, chemical and optical properties [1-3], graphene-based nanosheets have been explored as drug-delivery vehicles, biosensors, and imaging modalities [4, 5]. The use of graphene-based nanosheets in biomedical applications, however, has been hampered by the instability of these nanosheets under physiological conditions and concerns about their *in vivo* safety.

A number of strategies for modifying and functionalizing graphene with synthetic polymers have been applied in an effort to improve the physiological stability of graphene-based nanosheets. Polyethylene glycol (PEG) has been used to modify graphene nanosheets via non-covalent or covalent methods for imaging [6] and drug delivery [7, 8]. Graphene oxide (GO) nanosheets have been chemically modified with six-armed PEG to increase stability in physiological solutions for delivery of aromatic anticancer chemicals [9]. Modification of GO nanosheets with linear PEG was reported to increase the *in vivo* safety of these nanosheets and allow the delivery of anticancer drugs to tumor tissues [8]. In addition to PEG, dextran [10] has been studied to stabilize GO nanosheets. Although these approaches have achieved some success in increasing the stability and safety of graphene-based nanosheets *in vivo*, surface modifications using tumor cell-recognizing moieties are still required to improve distribution to the tumor.

The overexpression of CD44 receptors has been observed in many types of tumor cells [11], and studied as a target for improved delivery of anticancer therapeutics [12]. Hyaluronic acid (HA) is known to be the ligand molecule of CD44 receptors [13, 14]. Self-assembled [15] and photo-crosslinked HA [16] nanoparticles have been reported to distribute to the tumor tissues via CD44 receptors with enhanced stability.

In this chapter, we tested whether HA could be used to increase graphene-based nanosheets stability and safety, and enhance the tumor-targeted distribution of anticancer drugs to CD44-overexpressing cancer cells.

2. Materials and methods

2.1. Synthesis of cholesteryl hyaluronic acid (CHA)

As shown in Fig. III-1, cholesteryl hyaluronic acid (CHA) was synthesized by linking the amino group of cholesteryl-2-aminoethylcarbamate (CAEC) with the carboxyl group of HA, according to a previously reported method [17]. CAEC for conjugation of the cholesterol moiety to HA was synthesized by dissolving 3.72 ml of ethylenediamine (55.66 mmol; Sigma-Aldrich, St. Louis, MO, USA) in 10 ml of anhydrous dichloromethane (DCM; Sigma-Aldrich), followed by addition of 10 ml of cholesteryl chloroformate (0.5 g, 1.13 mmol; Sigma-Aldrich) in anhydrous DCM and stirring on ice for 1 h. The reaction mixture was then washed three times with triple-distilled water (TDW) and dried over anhydrous magnesium sulfate (Samchun Pure Chemical Co., Pyeongtaek, Gyeonggi-do, South Korea). After removal of the organic solvent by evaporation under vacuum, a mixture of DCM and methanol (1:1, v/v) was added to the residue, and the filtrate containing CAEC was collected. The synthesis of CAEC was confirmed by ^{1}H-NMR using a Bruker Avance-500 MHz FT-NMR spectrometer (Bruker, Billerica, MA, USA). The molecular weight of CAEC was measured by electrospray ionization mass spectrometry (ESI-MS) using a Finnigan Mat Lcq mass spectrometer (Thermo Fisher Scientific, Inc., Waltham, MA, USA). ^{1}H-NMR analysis of CAEC revealed the following values: 0.67, 1.01 (s, each 3H, CH_3), 0.86 (d, 6H, CH_3), 0.92 (d, 3H, CH_3), 1.83-2.02 (m, 5H), 2.25-2.35 (m, 2H), 2.82 (t, 2H, NH_2CH_2), 3.21 (q, 2H, $NHCH_2$), 4.50 (m, 1H, OCH), and 5.37 (d, 1H, CHC) (Fig. III-1D). ESI-MS

analysis showed an m/z value of 473.26 for CAEC (Fig. III-1E).

Before the condensation reaction, HA (214 kDa; Lifecore Biomedical, Chaska, MN, USA) was converted to the tetrabutylammonium salt of HA (HA-TBA) using a cation exchange resin (Dowex 50WX8, Sigma-Aldrich), according to a previously reported method [18]. HA-TBA was used to increase the solubility of HA in dimethyl sulfoxide, the organic solvent used for the condensation reaction. After dissolving 100 mg of HA-TBA in 10 ml of dimethyl sulfoxide, 0.33 ml of CAEC (20 mg/ml) in a mixture of DCM and methanol (1:1, v/v) was added to the solution and stirred for 30 min at room temperature. Thereafter, 4.2 mg of 4-(4,6-dimethoxy-1,3,5-triazin-2-yl)-4-methylmorpholinium chloride (DMT-MM; Alfa Aesar, Ward Hill, MA, USA), a condensation reagent, in 0.5 ml of dimethyl sulfoxide was added. The molar feed ratio of glucuronic acids of HA:CAEC:DMT-MM was 100:5:6. After stirring for 24 h at room temperature, the reaction mixture was sequentially dialyzed against 50% methanol for 24 h, 150 mM NaCl for 24 h, and finally against TDW for 24 h. After dialysis, the resulting CHA was stored at 4 ℃ until use.

2.2. Preparation of rGO nanosheets

rGO nanosheets were synthesized from GO nanosheets according to a previously reported method [19], with slight modifications. In brief, to 2.0 ml of GO nanosheets (5 mg/ml) in TDW was added 8.0 ml of TDW, 0.5 ml of ammonia solution (28 w/w % in water; Junsei Chemical, Tokyo, Japan), and 5.0 ml of hydrazine monohydrate (64 w/w % in water; Sigma-Aldrich). The resulting

mixture was stirred at 80 ℃ for 10 min. After cooling to room temperature, excess hydrazine and ammonia was removed by dialysis (MWCO 100K; Spectrum Laboratories, Inc., Rancho Dominguez, CA, USA) against TDW. The obtained rGO nanosheets were stored at 4 ℃ until use.

2.3. Preparation and characterization of CHA-rGO nanosheets

For coating surfaces with CHA, rGO nanosheets in TDW (1 mg/ml) were mixed with the same volume of CHA solution (2 mg/ml). After sonication for 30 min, the mixture was dialyzed (MWCO 1000K; Spectrum Laboratories, Inc., Rancho Dominguez, CA, USA) against TDW for 24 h to remove extra free CHA. CHA-rGO was identified by Fourier transform infrared (FT-IR) spectroscopy (Nicolet 6700, Thermo Fisher scientific, Inc.).

The topography, thickness, and lateral size of rGO nanosheets with or without CHA coating were measured using atomic force microscopy (AFM, XE-150; PSIA Inc., Santa Clara, CA, USA) in non-contact mode. The AFM samples were prepared by immersing SiO_2-covered Si substrate in aqueous solutions of rGO or CHA-rGO overnight and drying under N_2 gas. The graft ratio of the cholesteryl group (per 100 HA units) was calculated from the integration ratio between the peak of the N-acetyl group in HA (δ=1.96, 3H, $COCH_3$) and that of methyl groups in cholesterol (δ=0.79, 3H, CH_3) in the ^{1}H-NMR spectrum (Fig.1C).

2.4. Stability test of rGO and CHA-rGO nanosheets

The stability of rGO and CHA-rGO nanosheets was tested in various media,

including TDW, phosphate-buffered saline (PBS; 50 mM, pH 7.4), and cell culture media (RPMI-1640; Gibco BRL Life Technologies, Carlsbad, CA, USA). An aliquot (0.2 ml) of rGO or CHA-rGO in TDW (rGO content, 0.5 mg/ml) was added to 0.8 ml of TDW, PBS or cell culture media, and the solutions were allowed to stand for 7 days. The stability of CHA-rGO nanosheets in various media was evaluated during this period by monitoring the mixtures for the appearance of precipitates using a digital camera (Canon PC1089, Canon Inc, Tokyo, Japan).

2.5. Preparation of physisorbed complexes of CHA-rGO nanosheets with Dox

Physisorbed complexes of Dox with rGO (rGO/Dox) or CHA-rGO (CHA-rGO/Dox) nanosheets, defined as nanophysisorplexes, were formed by adding 0.5 ml of Dox aqueous solution (0.5 mg/ml, Sigma-Aldrich) to 1 ml of rGO or CHA-rGO nanosheets in TDW and stirring for 2 h at room temperature. Free Dox was then removed using a PD-10 desalting column (GE Healthcare, Buckinghamshire, UK). The extent of Dox loading onto rGO and CHA-rGO nanosheets was determined by measuring the loss of Dox autofluorescence at 485 nm caused by the quenching of adsorbed Dox using a fluorescence microplate reader (Gemini XS, Molecular device, Sunnyvale, CA, USA).

The zeta potential values of rGO and CHA-rGO nanosheets, with or without Dox loading, were determined using an ELS-8000 instrument (Photal, Osaka, Japan). The samples were diluted with TDW, and zeta potential values were determined by laser Doppler microelectrophoresis at an angle of 22 °.

2.6. Cytotoxicity measurement of rGO and CHA-rGO nanosheets

The cytotoxicity of rGO and CHA-rGO nanosheets was determined using MTT assays. KB epidermal carcinoma cells were purchased from the American Type Culture Collection (Rockville, MD, USA) and cultured in RPMI-1640 medium supplemented with 10% fetal bovine serum, 100 units/ml penicillin, and 100 mg/ml streptomycin. For cell viability measurements, KB cells were seeded onto 48-well plates at a density of 6×10^4 cells/well. After overnight incubation, cells were exposed to different concentrations of rGO or CHA-rGO nanosheets for 24h. The viability of treated cells was measured by MTT assay as described previously [8]. The absorbance of the insoluble formazan product was measured at 570 nm using a microplate reader (Sunrise Basic; TECAN, Männedorf, Switzerland).

2.7. Cellular uptake test of Dox delivered by CHA-rGO nanosheets

The cellular uptake of Dox was tested in CD44-positive KB cells using confocal microscopy. The expression of CD44 on the surface of KB cells was confirmed by CD44 antibody staining. KB cells were incubated for 1 h at 4 ℃ with a fluorescein isothiocyanate (FITC)-conjugated rat anti-CD44 monoclonal antibody (Abcam, Cambridge, UK) at a 1:50 dilution. Goat FITC-labeled IgG1 antibody (Abcam, Cambridge, UK) was used as an isotype control. CD44-positive cell populations were identified using a BD FACSCalibur system equipped with Cell Quest Pro software (BD Bioscience, San Jose, CA, USA). KB cells were seeded onto cover glasses at a density of 8×10^4 cells/well in 24-well plates. The

next day, cells were treated with rGO/Dox or CHA-rGO/Dox at a concentration of 10 μM Dox. In competition assay experiments, cells were pre-incubated with 10 mM HA for 2 h prior to treatment with Dox. After incubating for various times, cells were washed and fixed with 4% paraformaldehyde in PBS for 15 min, and stained with 4',6-diamidino-2-phenylindole dihydrochloride. The fluorescence of cellular Dox was observed using a confocal laser-scanning microscope (LSM 5 Exciter; Carl Zeiss, Inc., Jena, Germany).

2.8. *In vitro* antitumor efficacy study of Dox in CHA-rGO nanosheets

The *in vitro* antitumor efficacy of CHA-rGO/Dox was tested using MTT assays. KB cells were seeded into 48-well plates at a density of 6×10^4 cells/well. The next day, cells were treated with Dox in free form or in complexes with rGO or CHA-rGO nanosheets. In some experiments, cells were pre-treated with 10 mM HA 2 h before treatment with Dox. After 24 h, cell viability was measured by MTT assay.

2.9. Acute toxicity test of rGO and CHA-rGO nanosheets

Five-week-old female Balb/c and athymic nude mice, obtained from Orient Bio Inc. (Seongnam, Kyonggi-do, South Korea), were used for acute toxicity tests. All animals were maintained and used in accordance with the Guidelines for the Care and Use of Laboratory Animals of the Institute of Laboratory Animal Resources, Seoul National University. Various amounts of rGO or CHA-rGO nanosheets were dispersed in a 5% glucose solution and intravenously injected into

the tail veins of mice. The survival of mice at 24 h post-injection was recorded for each group (n = 5).

2.10. *In vivo* molecular imaging

The *in vivo* distribution of DSPE-PEG_{5000}-Alexa Fluor 680-modified CHA-rGO/Dox nanosheets to tumor tissues was tested by molecular imaging. Five-week-old athymic nude mice (Orient Bio, Inc.) were subcutaneously inoculated at both dorsal sides with 2×10^6 KB cells. After tumors had become established, Dox (2 mg/kg) was intravenously administered in free form or in rGO or CHA-rGO nanosheets. After 1, 24 and 48 h, delivery efficiency was assessed using a Xenogen IVIS-200 system (Perkin Elmer Inc., Waltham, MA, USA) with the built-in Cy5.5 filter set.

2.11. *In vivo* antitumor activity test

The antitumor effects of Dox were tested using KB tumor-bearing mice. Five-week-old athymic nude mice (Orient Bio, Inc.) were subcutaneously injected at the dorsal right side with 2×10^6 KB cells. When tumor volumes reached 150-180 mm^3, mice were intravenously administered CHA-rGO. For systemic injection, mice were treated with 2 mg of Dox in free form or in nanophysisorplexes with rGO (5 mg/kg) or CHA-rGO/Dox (15 mg/kg) nanosheets every 3 d for a total of five injections. For histopathological analyses, tumor tissues were excised and weighed on day 24, and sections were stained with hematoxylin and eosin.

2.12. Statistics

Analysis of variance (ANOVA) with Student-Newman-Keuls post-hoc test was used for statistical evaluation of experimental data. All statistical analyses were done using SigmaStat software (version 3.5, Systat Software, Richmond, CA, USA); a p-value < 0.05 was considered significant.

3. Results

3.1. Synthesis and characterization of rGO and CHA-rGO nanosheets

CHA was synthesized by condensation of the amine group of CAEC and the carboxyl group of HA. The synthesis schemes for CAEC and CHA are summarized in Fig. 1A and 1B, respectively. CAEC was synthesized by coupling ethylenediamine to cholesteryl chloroformate (yield: 85.0 ± 3.6%) (Fig. III-1A). The graft ratio of the cholesteryl group (per 100 HA units) was 3.5 ± 0.4%. The ^{1}H-NMR spectrum of CHA showed the characteristic peaks of cholesterol (0.79 ppm) and HA polysaccharide skeleton (3.3–3.8 ppm). The graft ratio of the cholesteryl group (per 100 HA units), calculated from the integration ratio between the peak of the N-acetyl group in HA (δ=1.96, 3H, $COCH_3$) and that of the methyl group in cholesterol (δ=0.79, 3H, CH_3) in the ^{1}H-NMR spectrum, was 3.5 ± 0.4% (Fig. III-1C).

Plain rGO nanosheets were prepared from GO by hydrazine reduction under controlled conditions [19]. Upon reduction of GO nanosheets to rGO nanosheets, the brownish aqueous solution darkened. The FT-IR spectrum of rGO (Fig. III-3B) revealed that the hydroxyl (broad peak from 3000 to 3600 cm^{-1}) and carboxyl (1730 $cm^{-1)}$ functional groups in GO nanosheets were substantially removed by hydrazine reduction. UV-visible spectra (Fig. III-2) showed a redshift of the characteristic GO peak from 230 nm to 270 nm in plain rGO nanosheets. The thickness and lateral size of plain rGO nanosheets, revealed by AFM (Fig. III-3E), were 3.0 ± 0.7 nm and 101.8 ± 4.9 nm, respectively.

Surface coating of rGO by CHA was confirmed by FT-IR spectroscopy (Fig. III-3D). The typical peaks of the hyaluronan backbone (-OH, -COOH and -C-O-C-) and cholesterol (-CH) indicated the presence of CHA in the final product. The lateral size of CHA-rGO sheets was 180.0 ± 18.2 nm (Fig. III-3F).

3.2. Stability of rGO and CHA-rGO nanosheets

CHA-rGO showed higher stability in saline buffers and cell culture media compared with plain rGO nanosheets. The plain rGO nanosheets aggregated after dispersion in PBS and RPMI-1640 medium supplemented with 10% fetal bovine serum (Fig. III-3I). Unlike plain rGO nanosheets, CHA-rGO nanosheets did not form aggregates in PBS or media and their stable dispersion was maintained at least for 7 days (Fig. III-3J).

3.3. Cytotoxicity and *in vivo* safety of plain rGO and CHA-rGO nanosheets

The *in vitro* cytotoxicity profiles of plain rGO and CHA-rGO nanosheets were not significantly different (Fig. III-4A). After a 24-h treatment with 10 mg/ml of rGO nanosheets, cell viability was 80.0% ± 5.7% for plain rGO and 89.0% ± 5.1% for CHA-rGO nanosheets. Increasing the concentration of nanosheets to 40 mg/ml decreased cell viability to 76.8% ± 4.0% for plain rGO and 80.6% ± 3.7% for CHA-rGO nanosheets.

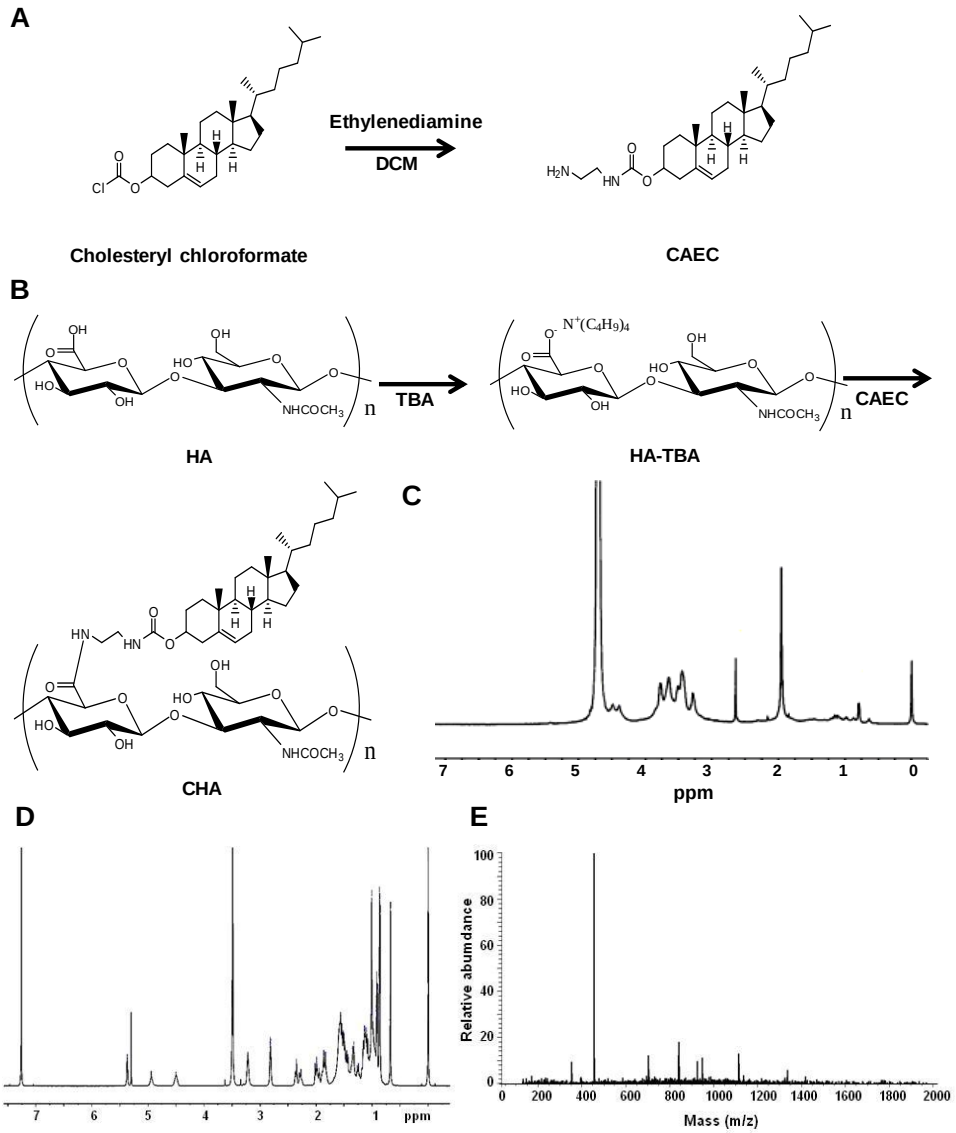

Fig. III-1. Synthesis scheme and characterization of CHA.

Synthesis schemes for CAEC (A) and CHA (B). (C) ^{1}H-NMR data for CHA. Confirmation of the synthesis of CAEC by ^{1}H-NMR (D) and ESI-MS (E).

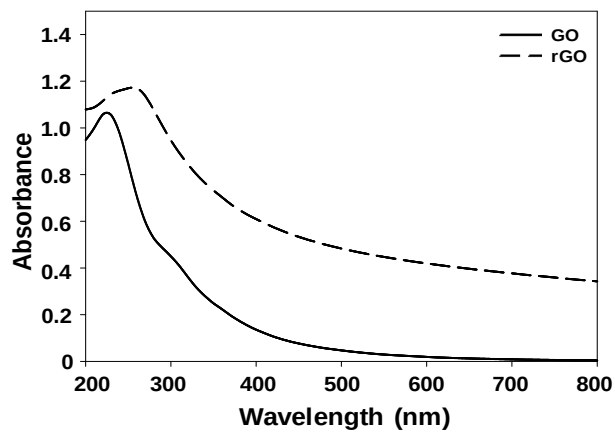

Fig. III-2. UV-Vis absorbance of GO and rGO.

UV-visible spectra of GO and rGO were recorded by UV/Vis spectrometer.

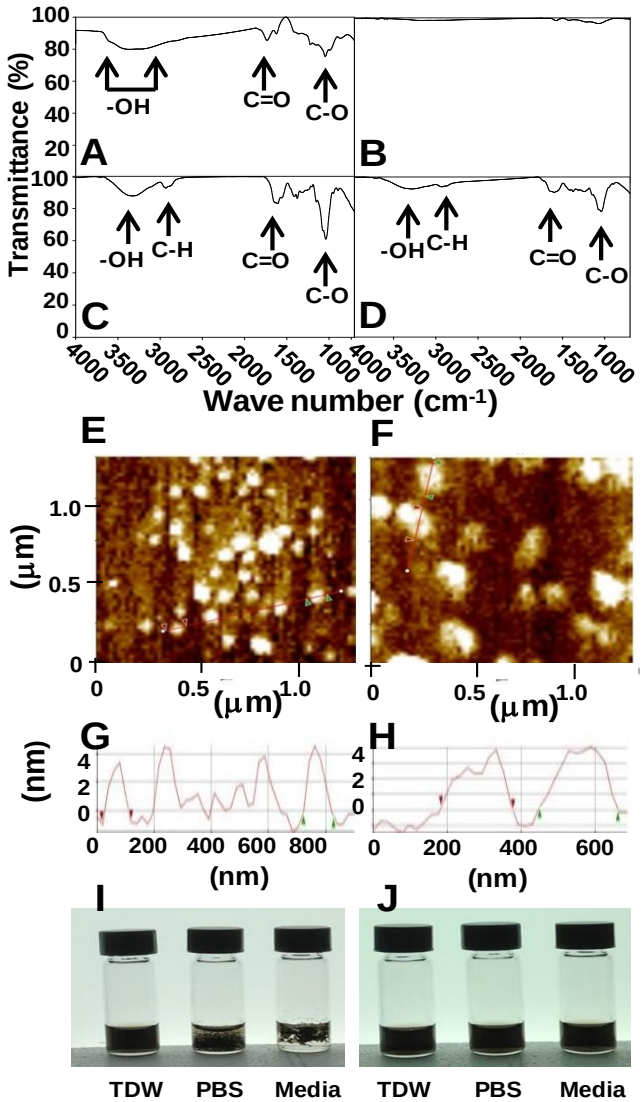

Fig. III-3. Characterization of rGO and CHA-rGO nanosheets.

(A-D) FT-IR spectra of GO nanosheets and their derivatives. The chemical structures of GO (A) and rGO (B) nanosheets, and CHA (C) and CHA-rGO nanosheets (D) were analyzed by infrared spectroscopy. (E-J) AFM topographic

images of rGO (E) and CHA-rGO (F) nanosheets, and thicknesses of rGO (G) and CHA-rGO (H) nanosheets. The stability of rGO (I) and CHA-rGO (J) nanosheet suspensions was evaluated in TDW, PBS, and RPMI media supplemented with 10% fetal bovine serum.

Unlike *in vitro* cytotoxicity results, the *in vivo* safety profiles of plain rGO and CHA-rGO nanosheets were significantly different (Fig. III-4B). After intravenous administration of plain rGO nanosheets in mice, the survival rate was 40% at a dose of 40 mg/kg. In contrast, the survival rate of mice injected with 40 mg/kg CHA-rGO nanosheets was 100%.

3.4. Characterization of rGO/Dox and CHA-rGO/Dox nanosheets

Compared with rGO, CHA-rGO provided higher loading capacity of Dox. The Dox loading behavior of rGO and CHA-rGO nanosheets was evaluated by fluorescence spectroscopy, exploiting the fluorescence-quenching property of graphene [20]. As the weight ratio of Dox to rGO decreased, the fluorescence intensity of Dox gradually decreased owing to the quenching of adsorbed Dox. The greatest quenching of Dox fluorescence was observed at a rGO:Dox weight ratio of 1:0.5 (Fig. III-5A). Similarly, the quenching of Dox increased as the weight ratio of Dox to CHA-rGO decreased (Fig. III-5B). Unlike plain rGO nanosheets, CHA-rGO nanosheets showed almost complete quenching of Dox fluorescence at a rGO:Dox weight ratio of 1:2, indicating a higher Dox loading capacity in CHA-rGO than plain rGO nanosheets (Fig. III-5C). At this weight ratio, the loading efficiencies of plain rGO and CHA-rGO nanosheets were 43.5% ± 2.1% and 90.9% ± 2.8%, respectively.

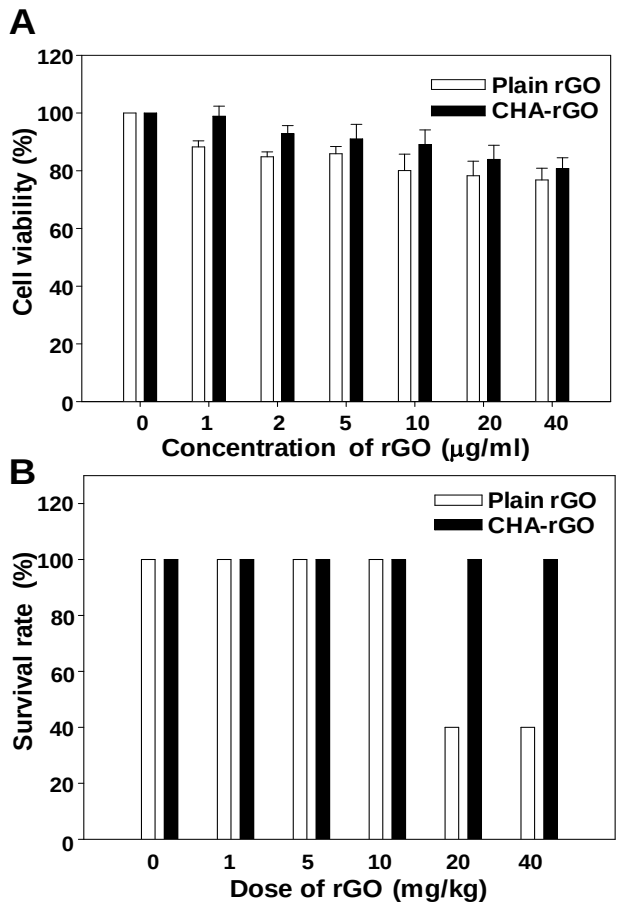

Fig. III-4. Cytotoxicity and *in vivo* safety of plain rGO and CHA-rGO nanosheets.

(A) KB cells were treated with different concentrations of plain rGO or CHA-rGO nanosheets. After incubating for 24 h, cell viability was measured by MTT assay. The results are expressed as means ± SE of four independent experiments. (B) Balb/c mice were intravenously injected with different doses of plain rGO or CHA-rGO nanosheets (n = 5), and survival was assessed 1 d later.

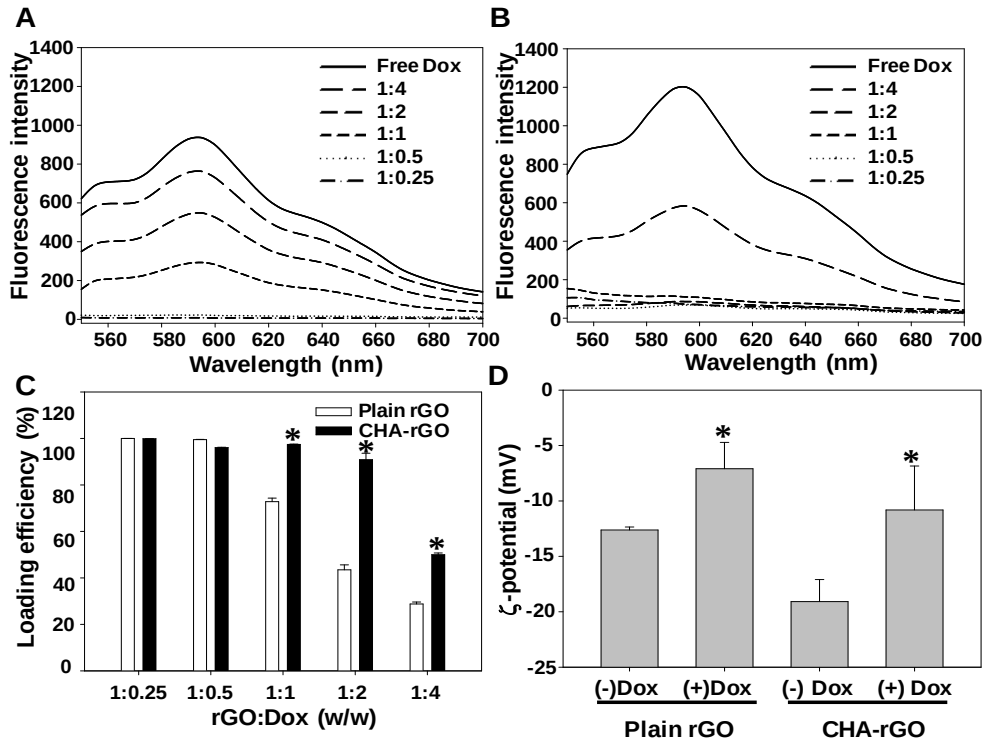

Fig. III-5. Interactions between Dox and plain rGO or CHA-rGO nanosheets.

Dox can adhere to plain rGO (A) and CHA-rGO (B) nanosheets through π-π interactions. Interactions between plain rGO or CHA-rGO and Dox were analyzed by fluorescence spectroscopy with various weight ratios. (C) The loading efficiency of Dox in physisorplexes with plain rGO or CHA-rGO was measured. *: Significantly higher than plain rGO group. (D) The zeta potentials of rGO, rGO/Dox, CHA-rGO, and CHA-rGO/Dox were determined by laser doppler microelectrophoresis. *: Significantly higher than (-)Dox group.

The zeta potential of CHA-rGO nanosheets was significantly lower than that of rGO nanosheets (Fig. III-5D). Upon coating with Dox at a rGO:Dox at a weight ratio of 1:0.5, the zeta potential values of Dox nanophysisorplexes of both plain rGO and CHA-rGO increased.

3.5. Cellular uptake of Dox delivered in CHA-rGO nanosheets

In KB cells, the uptake of Dox in CHA-rGO was mediated by CD44 receptors. The expression of CD44 on the surface of KB cells was confirmed by flow cytometric analysis of cells labeled with fluorescent anti-CD44 receptor antibody, which revealed a high fraction of fluorescence-positive cells (data not shown). Untreated KB cells and KB cells labeled with anti-isotype IgG1 antibody (data not shown), used as a control, showed a negligible fraction of fluorescence-positive cells. Confocal microscopy showed that the cellular uptake of Dox in CHA-rGO nanophysisorplexes (Fig. III-6A, III-6D) was greater than that in rGO physisorplexes (Fig. III-6C). The cellular uptake of Dox in CHA-rGO physisorplexes was decreased in the presence of competing HA in the culture medium (Fig. III-6E), indicating the CD44 dependence of this uptake.

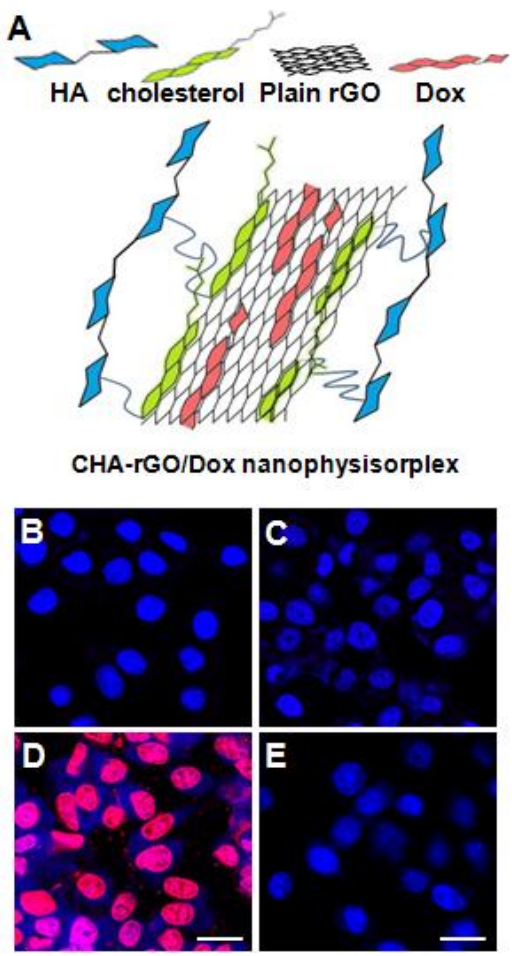

Fig. III-6. CD44-mediated cellular uptake of CHA-rGO nanophysisorplexes.

The scheme of CHA-rGO/Dox nanophysisorplexes is shown in (A). Cells were left untreated (B) or were treated with plain rGO/Dox (C) or CHA-rGO/Dox (D, E). CD44-mediated delivery was confirmed by pre-incubating without (D) or with (E) HA before CHA-rGO/Dox treatment. After incubating for 30 min, intracellular Dox autofluorescence was observed by confocal microscopy. Scale bar is 20 μm.

3.6. *In vitro* anticancer effects of Dox delivered by CHA-rGO nanosheets

Consistent with the results of cellular uptake experiments, Dox-loaded CHA-rGO nanosheets exerted a greater anticancer effect than Dox-loaded rGO nanosheets, and this enhanced anticancer effect was decreased in the presence of HA. After a 24-h treatment with 5 μM Dox in plain rGO/Dox and CHA-rGO/Dox, KB cell viability was 68.7% ± 1.6% and 28.4% ± 1.6%, respectively ($p < 0.05$). Upon pretreatment with free HA, KB cell viability was 48.5% ± 2.2% (Fig. III-7).

3.7. *In vivo* tumor tissue distribution of CHA-rGO/Dox nanophysisorplexes

After systemic administration, the tumor distribution of CHA-rGO/Dox physisorplexes was greater than that of rGO/Dox physisorplexes (Fig. III-8). At 1 h post-dose, the distribution of both rGO/Dox and CHA-rGO/Dox physisorplexes to the tumor sites was observed (Fig. III-8B). At 24 h (Fig. III-8C) and 48 h (Fig. III-8D) post-dose, the retention of physisorplexes differed between rGO/Dox and CHA-rGO/Dox, with CHA-rGO/Dox showing greater retention in tumor tissues. The highest intensity of fluorescence in tumor tissues was observed at the group treated with CHA-rGO/Dox (Fig. III-8E). At 48 h post-dose, photon count data showed that the tumor retention of CHA-rGO/Dox was 4-fold higher than that of rGO/Dox nanophysisorplexes (Fig. III-8F).

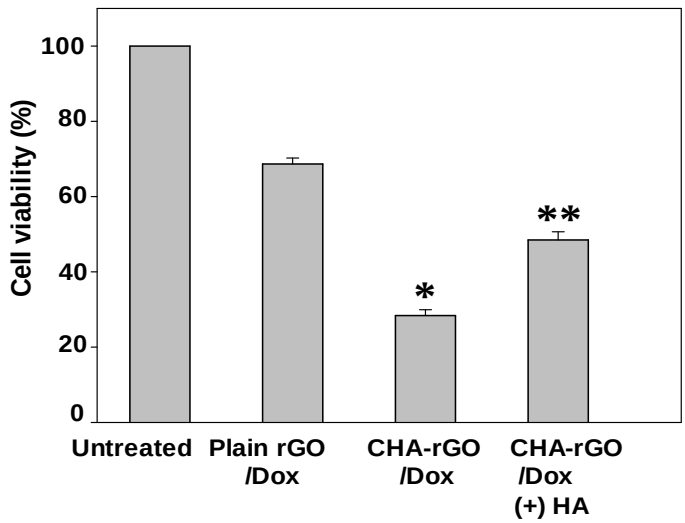

Fig. III-7. CD44-mediated anticancer effects of Dox delivered by CHA-rGO nanophysisorplexes.

Cells were left untreated or treated with plain rGO/Dox or CHA-rGO/Dox. CD44-mediated delivery was confirmed by pre-incubating without or with HA before CHA-rGO/Dox treatment. Cancer cell killing efficacy was quantified by MTT assay after incubation for 24 h. The results are expressed as means ± SE of four independent experiments (*$p < 0.05$ compared to the plain rGO/Dox group, **$p < 0.05$ compared to the CHA-rGO/Dox group; ANOVA and Student-Newman-Keuls test).

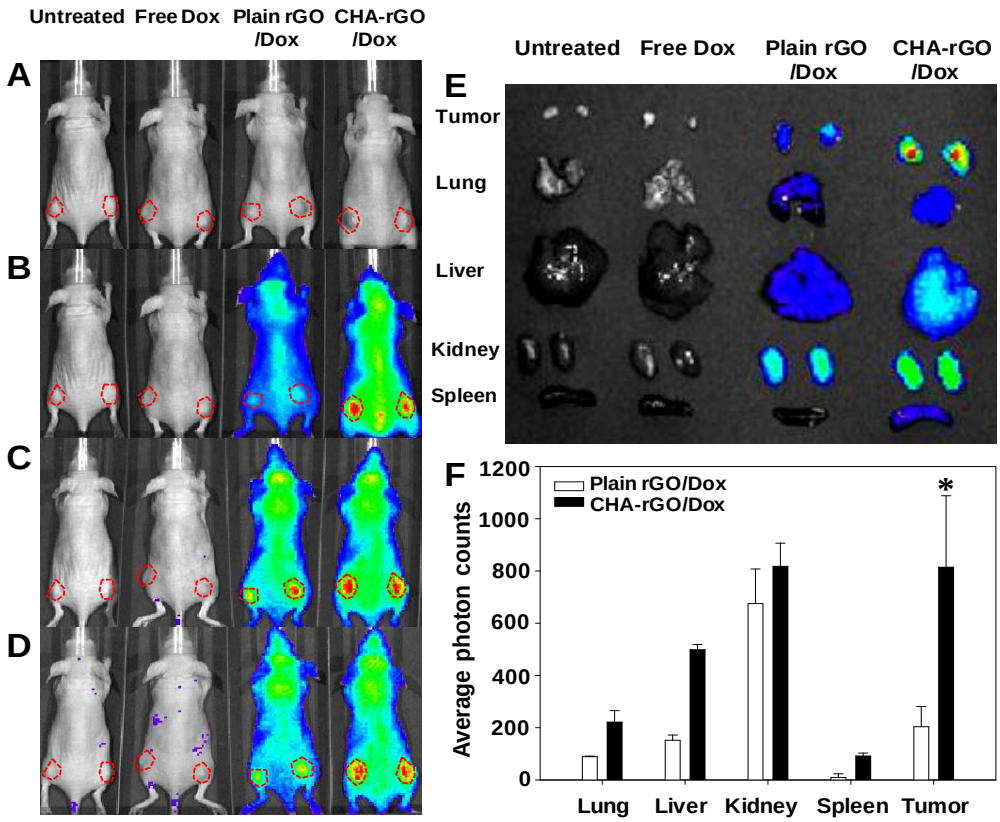

Fig. III-8. *In vivo* biodistribution of CHA-rGO nanophysisorplexes.

KB tumor-bearing mice (A) were treated systemically with free Dox, plain rGO/Dox, or CHA-rGO/Dox (Dox, 2 mg/kg). DSPE-PEG_{5000}-AlexaFluor680-modified rGO and CHA-rGO were prepared through hydrophobic interactions with the DSPE component. After 1 (B), 24 (C) and 48 h (D), the *in vivo* distribution of Alexa Fluor 680 fluorescence was visualized using a molecular imaging system. At 48 h post-dose, five organ tissues (tumor, lung, liver, kidney, and spleen) were excised for visualization (E) and quantification of average photon counts (F) using an *in vivo* imaging system. The results are expressed as means ± SD of three

independent experiments (*$p < 0.05$ compared to the rGO/Dox group ($n = 6$ tumors); ANOVA and Student-Newman-Keuls test).

3.8. *In vivo* antitumor effects of Dox delivered by CHA-rGO nanosheets

The antitumor activity of Dox was significantly enhanced by delivery using CHA-rGO nanosheets (Fig. III-9). On day 24 after tumor inoculation, tumor volumes were similar between free Dox and plain rGO/Dox-treated groups. The lowest tumor volume was observed for CHA-rGO/Dox nanophysisorplexes (Fig. III-9A). Tumor weights were lowest on day 24 after delivery of Dox using CHA-rGO nanosheets (Fig. III-9B, III-9C). There were no clear differences among the images of tumor cell nuclei between untreated (Fig. III-9D) and free Dox-treated tumor tissues (Fig. III-9E). In contrast, tumor cell nuclei were also found to have disappeared in the CHA-rGO/Dox-treated group (Fig. III-9G).

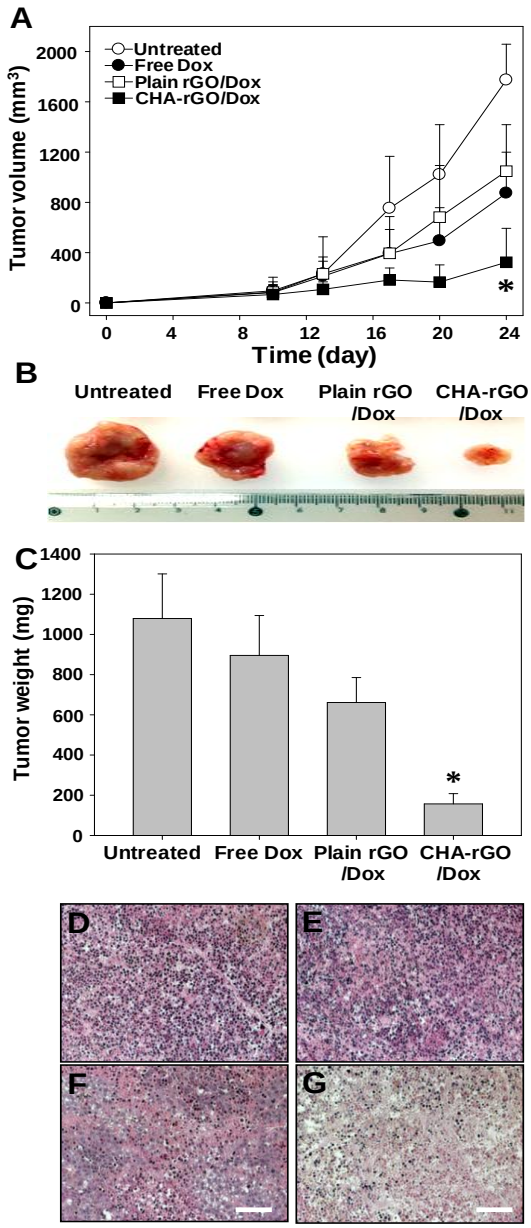

Fig. III-9. Anticancer effects of CHA-rGO nanophysisorplexes

KB tumor-bearing mice were intravenously treated with Dox alone or in complex with plain rGO or CHA-rGO (Dox, 2 mg/kg) every 3 days beginning on day 7. On

day 24, tumor tissues were excised for visualization (B) and weighing (C), and were sectioned for hematoxylin and eosin staining (D, untreated; E, free Dox; F, plain rGO/Dox; G, CHA-rGO/Dox). Scale bar, 100 mm. (*$p < 0.05$ compared to other groups; ANOVA and Student-Newman-Keuls test.)

4. Discussion

In this chapter, we demonstrated that CHA-rGO nanosheets can be used for delivery of anticancer drugs to tumor tissues. Compared to plain rGO nanosheets, CHA-rGO nanosheets exhibited enhanced Dox-loading capacity, stability in buffer, cellular uptake, and tumor retention *in vivo*.

For surface coating with CHA, we used rGO nanosheets, generated from GO nanosheets by hydrazine reduction, rather than GO nanosheets. Compared with GO nanosheets, rGO nanosheets offer advantages in terms of electronic conductivity and high near-infrared absorbance for a potential photothermal effect [21-24]. Owing to the decrease in polar functional groups upon reduction, the π-π stacking capacity of hydrophobic molecules on rGO nanosheets could be maximized compared with GO nanosheets. However, because of the salt effect of lyophobic colloids, such rGO nanosheets are extremely unstable in saline buffers and form precipitates immediately (Fig. III-3I). Thus, despite their advantages, plain rGO nanosheets would be of limited value for biomedical applications because of such stability issues.

The enhanced stability of CHA-rGO in various media (Fig. III-3J) would be due to the contribution of HA covering the surfaces of rGO nanosheets. To enhance the stability of rGO nanosheets and enhance their tumor cell-targeting ability, we used CHA as a coating material. The cholesterol moiety of CHA may serve as an anchoring molecule, attaching CHA to rGO nanosheets via hydrophobic interactions. The binding affinity of cholesterol for carbon-based

nanomaterials has been previously investigated [21, 22], and a cholanic acid derivative of HA has been used to coat the surfaces of carbon nanotubes [23]. HA is a highly water-soluble biopolymer which forms a coil structure by hydrogen bonding between hydroxyl groups [24]. HA has been widely used as a hydrophilic surface coating material of medical devices, and tissue engineering [25]. Surface coating of HA was reported to increase the hydrophilicity of polyhydroxyalkanoate-based scaffold [26]. Surfaces of polylactic acid-glycolic acid scaffold were coated with hydrophilic hyaluronic acid for cartilage tissue engineering [27]. In CHA-rGO, the presence of HA on rGO via cholesterol as an anchoring moiety could increase the hydrophilicity of nanosheets surfaces and result in the higher stability in aqueous media.

In this chapter, we observed that the HA moiety of CHA provided CD44 receptor-mediated cellular delivery of CHA-rGO nanosheets and enhanced the stability of rGO nanosheets in physiological solutions. HA has been previously reported to increase the tumor distribution of nanoparticles via interaction with CD44 receptors. For example, photo-crosslinked HA-based nanoparticles have been reported to increase the *in vivo* tumor tissue delivery of paclitaxel [16], and HA-based, self-assembling nanosystems have been designed for siRNA delivery to tumors expressing CD44 receptors [28]. In addition to promoting tumor distribution, we provide evidence that coating the surface of rGO with HA is additionally useful for stabilizing rGO under physiological conditions.

CHA-rGO nanosheets provided greater Dox loading capacity compared with rGO nanosheets (Fig. III-5C). Owing to their ultra-high planar surface area,

graphene-based nanosheets can adsorb aromatic drugs via π-π stacking and hydrophobic interactions, and thus exhibit a high loading capacity [10,29]. Additional electrostatic interactions between the negatively charged carboxyl groups of HA on CHA-rGO and the positively charged Dox may further contribute to the greater Dox loading capacity of CHA-rGO nanosheets. The increase in zeta potential values of CHA-rGO upon complexation with Dox supports the possibility of electrostatic interactions (Fig. III-5D).

The main pathway of CHA-rGO/Dox uptake is likely CD44 receptor-mediated endocytosis upon binding of HA moieties to the cell surfaces. In support of this, we found that the cellular uptake of Dox in CD44 receptor-overexpressing KB cells was enhanced by delivery in CHA-rGO nanosheets compared with rGO nanosheets. Evidence for a CD44-mediated process is provided by our observation that the presence of HA reduced the cellular uptake of Dox in CHA-rGO nanosheets (Fig. III-6), consistent with competition between CHA-rGO and HA for cellular entry. Moreover, as would be expected for an endocytosis mechanism, which is a temperature-dependent process, the ability of KB cells to take up Dox in CHA-rGO nanosheets at 4℃ was poor (data not shown).

As a probe for *in vivo* molecular imaging of CHA-rGO nanosheets, we used DSPE-PEG_{5000}-AlexaFluor680, which is anchored via its hydrophobic phospholipid moiety onto the rGO surface via hydrophobic interactions. PEG was used in the probe as a spacer to prevent quenching of the fluorescent probe by rGO nanosheets through fluorescence resonance energy transfer. The presence of a PEG bridge can prevent graphene-induced quenching of conjugated fluorescein, a

modification that has been exploited for *in vitro* cellular imaging applications [6].

The *in vivo* antitumor effects of Dox were greatest in tumor-bearing mice treated with CHA-rGO/Dox physisorplexes. This greater antitumor efficacy of CHA-rGO/Dox reflects the higher distribution and prolonged retention of CHA-rGO/Dox in tumor sites. Our molecular imaging data revealed that the tumor retention of CHA-rGO/Dox 48 h post-injection was higher than that of plain rGO/Dox. The *in vivo* antitumor efficacy of CHA-rGO/Dox indicates that Dox can be released from CHA-rGO nanosheets and exert its anticancer effects at tumor sites.

Recently, HA has been used for surface modification of carbon-based nanomaterials such as graphene oxide [30] and single-walled carbon nanotubes [23]. Chemical conjugation of HA to graphene oxide was shown to enhance the delivery to tumor cells positive with CD44 receptors [30]. As compared to chemical conjugation, the physical coating of HA on rGO via cholesterol moiety as an anchor may provide simple and convenient new alternative in surface modification. Moreover, unlike the previous study, we used rGO for CHA coating. Compared with GO nanosheets, rGO nanosheets offer advantages in terms of electronic conductivity and high near-infrared absorbance for a potential photothermal effect [31-34]. Another study reported that the coating of single-walled carbon nanotubes with cholanic acid derivative of HA could provide higher distribution to tumor tissues expressing CD44 receptors [23]. Here, we showed that the surface coating of HA could not only enhance tumor distribution, but also significantly improve the *in vivo* safety profile of nanomaterials (Fig.

III-4B). Moreover, w provided evidence that CHA-rGO can be used as a potential theranostic platform for imaging (Fig. III-8) and anticancer drug delivery to tumor tissues (Fig. III-9).

5. References

[1] Park S, Ruoff RS. Chemical methods for the production of graphenes. Nat Nanotech 2009;4:217-24.

[2] Dreyer DR, Park S, Bielawski CW, Ruoff RS. The chemistry of graphene oxide. Chem Soc Rev 2010;39:228-40.

[3] Loh KP, Bao Q, Ang PK, Yang J. The chemistry of graphene. J Mater Chem 2010;20:2277-89.

[4] Wang Y, Li Z, Wang J, Li J, Lin Y. Graphene and graphene oxide: biofunctionalization and applications in biotechnology. Trends Biotechnol 2011;29:205-12.

[5] Yang K, Feng L, Shi X, Liu Z. Nano-graphene in biomedicine: theranostic applications. Chem Soc Rev 2013;42:530-47.

[6] Peng C, Hu W, Zhou Y, Fan C, Huang Q. Intracellular imaging with a graphene-based fluorescent probe. Small 2010; 6: 1686-92.

[7] Sun X, Liu Z, Welsher K, Robinson JT, Goodwin A, Zaric S, et al. Nano-graphene oxide for cellular imaging and drug delivery. Nano Res 2008;1:203-12.

[8] Miao W, Shim G, Lee S, Choe YS, Oh YK. Safety and tumor tissue accumulation of pegylated graphene oxide nanosheets for co-delivery of anticancer drug and photosensitizer. Biomaterials 2013;34:3402-10.

[9] Liu Z, Robinson JT, Sun X, Dai H. PEGylated nanographene oxide for delivery of water-insoluble cancer drugs. J Am Chem Soc

2008;130:10876-7.

[10] Kim YK, Kim MH, Min DH. Biocompatible reduced graphene oxide prepared by using dextran as a multifunctional reducing agent. Chem Commun 2011;47:3195-7.

[11] Zöller M. CD44: can a cancer-initiating cell profit from an abundantly expressed molecule? Nat Rev Cancer. 2011;11:254-67.

[12] Ghosh SC, Neslihan Alpay S, Klostergaard J. CD44: a validated target for improved delivery of cancer therapeutics. Expert Opin Ther Targets. 2012;16:635-50.

[13] Toole BP. Hyaluronan: from extracellular glue to pericellular cue. Nature reviews Cancer 2004;4:528-39.

[14] Avigdor A, Goichberg P, Shivtiel S, Dar A, Peled A, Samira S, et al. CD44 and hyaluronic acid cooperate with SDF-1 in the trafficking of human CD34+ stem/progenitor cells to bone marrow. Blood 2004;103:2981-9.

[15] Choi KY, Chung H, Min KH, Yoon HY, Kim K, Park JH, et al. Self-assembled hyaluronic acid nanoparticles for active tumor targeting. Biomaterials 2010;31:106-14.

[16] Yoon HY, Koo H, Choi KY, Chan Kwon I, Choi K, Park JH, et al Photo-crosslinked hyaluronic acid nanoparticles with improved stability for *in vivo* tumor-targeted drug delivery. Biomaterials 2013;34:5273-80.

[17] Nakai T, Hirakura T, Sakurai Y, Shimoboji T, Ishigai M, Akiyoshi K. Injectable hydrogel for sustained protein release by salt-induced association of hyaluronic acid nanogel. Macromol Biosci 2012;12:475-83.

[18] Oh EJ, Kim JW, Kong JH, Ryu SH, Hahn SK. Signal transduction of hyaluronic acid-peptide conjugate for formyl peptide receptor like 1 receptor. Bioconjugate Chem 2008;19:2401-8.

[19] Li D, Muller MB, Gilje S, Kaner RB, Wallace GG. Processable aqueous dispersions of graphene nanosheets. Nat Nanotech 2008;3:101-5.

[20] Lu CH, Yang HH, Zhu CL, Chen X, Chen GN. A graphene platform for sensing biomolecules. Angew Chem Int Edit 2009;48:4785-7.

[21] Ciani AJ, Gupta BC, Batra IP. Interaction of cholesterol with carbon nanotubes: A density functional theory study. Solid State Commun 2008;147**:**146-51.

[22] Chhikara BS, Misra SK & Bhattacharya S 2012. CNT loading into cationic cholesterol suspensions show improved DNA binding and serum stability and ability to internalize into cancer cells. Nanotechnology 23**,** 065101.

[23] Swierczewska M, Choi KY, Mertz EL, Huang X, Zhang F, Zhu L et al. A facile, one-step nanocarbon functionalization for biomedical applications. Nano Lett 2012;12: 3613-20.

[24] Ferguson EL, Roberts JL, Moseley R, Griffiths PC, Thomas DW. Evaluation of the physical and biological properties of hyaluronan and hyaluronan fragments. Int J Pharm 2011;420:84-92.

[25] Collins MN, Birkinshaw C. Hyaluronic acid based scaffolds for tissue engineering--a review. Carbohydrate polymers. 2013;92:1262-79

[26] Wang YW, Wu Q, Chen GQ. Reduced mouse fibroblast cell growth by increased hydrophilicity of microbial polyhydroxyalkanoates via

hyaluronan coating. Biomaterials 2003;24:4621-9.

[27] Chang NJ, Jhung YR, Yao CK, Yeh ML. Hydrophilic gelatin and hyaluronic acidtreated PLGA scaffolds for cartilage tissue engineering. J Appl Biomater Funct Mater 2013;11:45-52.

[28] Ganesh S, Iyer AK, Morrissey DV, Amiji MM. Hyaluronic acid based self-assembling nanosystems for CD44 target mediated siRNA delivery to solid tumors. Biomaterials 2013;34:3489-502.

[29] Zhang X, Yin J, Peng C, Hu W, Zhu Z, Li W, et al. Distribution and biocompatibility studies of graphene oxide in mice after intravenous administration. Carbon 2011;49:986-95.

[30] Li F, Park S-J, Ling D, Park W, Han JY, Na K, et al. Hyaluronic acid-conjugated graphene oxide/photosensitizer nanohybrids for cancer targeted photodynamic therapy. Journal of Materials Chemistry B. 2013;1:1678-86.

[31] Kim DJ, Sohn IY, Jung JH, Yoon OJ, Lee NE, Park JS. Reduced graphene oxide field-effect transistor for label-free femtomolar protein detection. Biosens Bioelectron 2013; 41**:** 621-6.

[32] Lobo DE, Fu J, Gengenbach T, Majumder M. Localized deoxygenation and direct patterning of graphene oxide films by focused ion beams. Langmuir 2012;28**:** 14815-21.

[33] Mihara S, Tsubota T, Murakami N, Ohno T. Improvement of electrical conductivity while maintaining a high-transmittance of graphene oxide/MWCNT film by hydrazine reduction. J Nanosci Nanotechnol

2012;12**:**6930-4.

[34] Robinson JT, Tabakman SM, Liang Y, Wang H, Casalongue HS, Vinh D, et al. Ultrasmall reduced graphene oxide with high near-infrared absorbance for photothermal therapy. J Am Chem Soc 2011;133:6825-31.

Chapter IV

Structure-dependent photothermal anticancer effects of carbon-based photoresponsive nanomaterials

1. Introduction

Although remarkable progress has been made in cancer treatment, conventional strategies, such as surgical resection, chemotherapy, radiotherapy, and their combinations have shown limited success toward cancer eradication over the past few decades. Photothermal therapy (PTT) for the treatment of solid tumors recently emerged as an attractive alternative approach to convert absorbed light into local heating through non-irradiative mechanisms [1]. Anticancer PTT is advantageous over surgical methods and chemotherapy because it permits spatial and temporal control, is minimally invasive, and results in few complications [2-4].

Near-infrared (NIR) light (700–1100 nm) is used in PTT because it penetrates deeply into the tissue and is absorbed only to a small degree by normal tissue [5, 6]. Light-absorbing agents that display a high degree of absorption in the NIR are generally involved in PTT processes to facilitate energy conversion from light to heat in localized tumor tissues. Experimentally tested photoresponsive light absorbers include gold [2, 7], and carbon nanomaterials such as carbon nanotubes [8] and graphene [9, 10].

Single-walled carbon nanotubes (SWCNT) and graphene nanosheets have been studied for their utility in photothermal cancer treatment. Intratumoral injection of phospholipid-polyethylene glycol-coated SWCNT [8] or polyethylene glycol-conjugated SWCNT [11] has been reported to destroy tumors upon irradiation with NIR laser. Intravenous injection of polyethylene glycol-conjugated

graphene nanosheets [9] has been shown to provide NIR laser-induced antitumor photothermal effects. Polyvinylpyrrolidone-coated graphene nanosheets were reported to induce photothermal death of human glioma cells [12].

Although previous studies described the potential utility of SWCNTs and graphene-based nanosheets in PTT, it is little studied whether the different geometry of these carbon-based nanomaterials could influence the biological and pharmacological effects. In this chapter, using amphiphilic triblock copolymer-functionalized SWCNT and graphene nanosheets, we tested whether the structure of carbon-based nanomaterials could affect their physical properties, *in vivo* fates, and photothermal anticancer effects.

2. Materials and methods

2.1. Preparation of carbon nanomaterials functionalized with poloxamer 407

Graphene nanosheets functionalized with poloxamer 407 (PGNS) were prepared by the aqueous-phase exfoliation of graphite in the presence of poloxamer 407 (Sigma-Aldrich, St. Louis, MO, USA), as described previously [13]. In brief, 50 mg graphite powder (Sigma-Aldrich) was suspended in 50 ml of a 1% w/v poloxamer 407 solution. The dispersions were sonicated over ice for 2 h using a horn ultrasonicator equipped with a 13 mm diameter probe (VCX 500, Sonics & materials, Inc., Newtown, CT, USA). The solutions were then centrifuged at 16,000 g for 30 min twice to remove aggregates. The resulting PGNS supernatants were collected and stored at 4 ℃ until use.

SWCNT non-covalently coated with poloxamer 407 (PSWCNT) were prepared by incubating single-walled carbon nanotubes in the presence of poloxamer 407 (Sigma-Aldrich), as described previously [13]. Briefly, SWCNT (Nanocs Inc., New York, NY, USA) were suspended in 50 ml of a 1% w/v poloxamer 407 solution. These dispersions were sonicated over ice for 2 h using a horn ultrasonicator equipped with a 13 mm diameter probe (VCX 500). The dispersions were then centrifuged at 16,000 g for 30 min twice to remove aggregates. The resulting PSWCNT supernatants were then collected and stored at 4 ℃ until use.

2.2. Characterization of the PGNS and PSWCNT

The UV-Vis spectra of the PGNS and SWCNT were recorded over the range 200–810 nm using a UV-Vis spectrophotometer (UV-3100, Shimadzu Corp, Tokyo, Japan). The concentrations of carbon in the PGNS and PSWCNT suspensions were determined from the extinction coefficient at 660 nm (6600 L g^{-1} m^{-1}) [14], and at 808 nm (4650 L g^{-1} m^{-1}) [15], respectively. The sizes and morphologies of the PGNS and PSWCNT were examined by transmission electron microscopy (JEM1010, Jeol Ltd, Tokyo, Japan).

2.3. Laser irradiation and photothermal imaging

Carbon nanomaterial-based suspensions of PGNS or PSWCNT were serially diluted with distilled water and irradiated using an 808 nm continuous wave NIR diode laser beam (BWT Beijing LTD, Beijing, China) with an output power of 1.2 W. The temperature and photothermal images of the carbon nanomaterial-based suspensions during laser irradiation were recorded using an infrared thermal imaging system every 30 seconds (FLIR T420, FLIR Systems Inc., Danderyd, Sweden).

2.4. *In vitro* cellular uptake study

The cellular uptakes of PGNS or PSWCNT were determined using confocal microscopy. The cellar uptake was visualized by labeling the PGNS and PSWCNT with 1,2-distearoyl-sn-glycero-3-phosphoethanolamine-N-poly(ethyleneglycol)$_{5000}$-Cy5.5 (DSPE-PEG$_{5000}$-Cy5.5) lipids. Murine SCC7 squamous carcinoma cells

(American Type Culture Collection, Rockville, MD, USA) were cultured in Dulbecco's modified Eagle medium (Gibco BRL life Technologies, Carlsbad, CA, USA) supplemented with 10% fetal bovine serum and 100 units/ml penicillin plus 100 μg/mL streptomycin (complete DMEM media). SCC7 cells were seeded onto a cover glass at a density of 1×10^5 cell/well in 12-well plates. When the cells reached 70% confluence, DSPE-PEG_{5000}-Cy5.5-labeled PGNS or PSWCNT suspensions with a carbon concentration of 10 μg/ml were added to each well. After 24 h, the cells were washed by cold phosphate-buffered saline (PBS), fixed with 4% paraformaldehyde for 15 min, and stained with 4',6-diamidino-2-phenylindole dihydrochloride (DAPI, Sigma-Aldrich). The fluorescence of the cells was observed using a confocal laser scanning microscope (LSM 5 Exciter; Carl Zeiss, Inc., Jena, Germany). Flow cytometry measurements were conducted by harvesting the cells and washing thrice with cold PBS containing 2% fetal bovine serum. The cells were analyzed using a BD FACSCalibur flow cytometer using the Cell Quest Pro software (BD Bioscience, San Jose, CA, USA).

2.5. Quantitative cell viability assay following NIR laser irradiation

SCC7 cells were seeded onto 12-well plates at a density of 1×10^5 cell/well. The following day, cells were treated with PGNS or PSWCNT at a carbon concentration of 20 μg/ml. After 24 h incubation at 37℃, the cells were washed twice with cold PBS and re-suspended in complete DMEM media. The cell suspensions were irradiated with an 808 nm continuous-wave NIR diode laser at an

output power of 1.2 W for various exposure periods. In some experiments, untreated SCC7 cell suspensions were mixed with PGNS or PSWCNT at various carbon concentrations and irradiated with the NIR laser. Immediately after irradiation, the cells were diluted 10-fold using complete DMEM media and transferred to 96-well plates for the cell viability assays. The cell viability was quantified using a Cell Counting Kit-8^{TM} (CCK8) according to the protocol provided by the manufacturer (Dojindo Molecular Technologies, Inc., Rockville, MD, USA). The values are expressed as a percentage of the cell viability measured in the control groups.

2.6. Animals

In vivo experiments were conducted using five-week old female Balb/c athymic nude mice supplied by Orient Bio. Lab. Animal Inc. (Seungnam, Kyonggi-do, South Korea, approved animal experimental protocol number SNU-130129-3-1). Animals were raised under standard pathogen-free conditions at the animal center for pharmaceutical research in the Seoul National University. All animal experiments were conducted in accordance with the Guidelines for the Care and Use of Laboratory Animals of the Institute of Laboratory Animal Resources, Seoul National University.

2.7. Pharmacokinetic study

The pharmacokinetic profiles of the PGNS and PSWCNT were determined by intravenously administering to the mice DSPE-PEG$_{5000}$-Cy5.5-labeled PGNS or

PSWCNT at a carbon dose of 5 mg/kg. The blood samples were collected at various time points after dosing. The fluorescence intensities in the blood were measured using an eXplore Optix System (Advanced Research Technologies Inc., Montreal, Canada). The excitation and emission spots were raster-scanned in 1 mm steps over the region of interest to generate the emission wavelength scans. A 670 nm pulsed laser diode was used to excite Cy5.5 molecules. Long wavelength fluorescence emission (600–700 nm) was detected using a fast photomultiplier tube (Hamamatsu Photonics, Hamamatsu, Japan) and a time-correlated single photon counting system (Becker and Hickl GmbH, Berlin, Germany). Finally, the non-compartmental pharmacokinetic parameters were calculated using the software program WinNonlin^{TM} (Scientific Consulting Inc., Lexington, KY, USA). The mean residence time (MRT) was calculated using the non-compartmental method by dividing the area under the momentum curve with AUC.

2.8. *In vivo* molecular imaging

The biodistribution of PGNS or PSWCNT in tumor-bearing mice were examined by molecular imaging. Mice were subcutaneously inoculated at the right dorsal side with 1×10^6 SCC7 cells, and tumors were allowed to grow over time. Suspensions of the carbon-based nanomaterials, DSPE-PEG_{5000}-Cy5.5-labeled PGNS and PSWCNT, were intravenously administered at a carbon dose of 5 mg/kg to the SCC7-bearing mice. At various time points post-dose, the tumor tissue distribution of the fluorescent PGNS or PSWCNT was assessed using the eXplore Optix System, as described above.

2.9. *In vivo* photothermal tumor ablation study

The photothermal anticancer effects of PGNS and PSWCNT were tested using SCC7 tumor-bearing nude mice. Five-week old athymic nude mice (Orient Bio, Inc.) were subcutaneously injected at the dorsal right side with 1×10^6 SCC7 cells. When the tumor volume reached 50–80 mm^3, the mice were subjected to intravenous administration of PGNS or PSWCNT at the same carbon dose of 5 mg/kg. One day post-administration, the mice were anesthetized and positioned in a mouse holder. The tumor sites were irradiated for 3 min with an 808 nm continuous wave NIR laser at an output power of 1.2 W. Light-induced temperature changes in the tumor region were recorded using a real-time infrared thermal imaging system (FLIR T420, FLIR Systems Inc., Danderyd, Sweden). The tumor sizes were measured in two dimensions using a slide caliper, and the tumor volume was calculated according to the equation $a \times b^2 \times 0.5$, where a is the largest and b is the smallest diameter. In some experiments, the tumor tissues were extracted after irradiation and fixed in 4% paraformaldehyde in PBS, embedded in paraffin, and sectioned at a thickness of 6 μm. The slides of the tumor tissue were stained with hematoxylin and eosin and were observed using optical microscopy. Survival was evaluated by monitoring the mice daily in each group after the administration of PGNS or PSWCNT.

2.10. Statistics

ANOVA techniques were used to statistically evaluate the experimental data. The Student–Newman–Keuls test was used as a post-hoc test. All statistical

analyses were performed using the SigmaStat software (version 3.5, Systat Software, Richmond, CA, USA), and a p-value of < 0.05 was considered significant.

3. Results

3.1. Characterization and thermal conductivity of carbon-based nanomaterials

PSWCNT and PGNS provided similar dispersions, UV spectra, and photothermal conductivity values (Fig. IV-1A). Both PSWCNT and PGNS were freely dispersed in fetal bovine serum (Fig. IV-1B). The absorption patterns of the UV-vis spectra of the two carbon-based nanomaterials showed peaks at 260-270 nm and tapered down at longer wavelengths. TEM measurements revealed the unique nanotube and nanosheet structures for PSWCNT (Fig. IV-1C) and PGNS (Fig. IV-1D), respectively. The photothermal properties of PSWCNT were similar to those of PGNS (Fig. IV-2). Regardless of the carbon-based nanomaterial structure, a dose-dependent increase in the temperature was observed in suspensions of PSWCNT or PGNS in proportion to the NIR laser (808 nm) irradiation time. Following 5 min NIR irradiation, the temperatures of the nanomaterial suspensions prepared with a carbon concentration of 10 μg/ml reached 48.0 ± 1.8 ℃ for the PSWCNT (Fig. IV-2A), and 52.1 ± 1.0 ℃ for the PGNS (Fig. IV-2B).

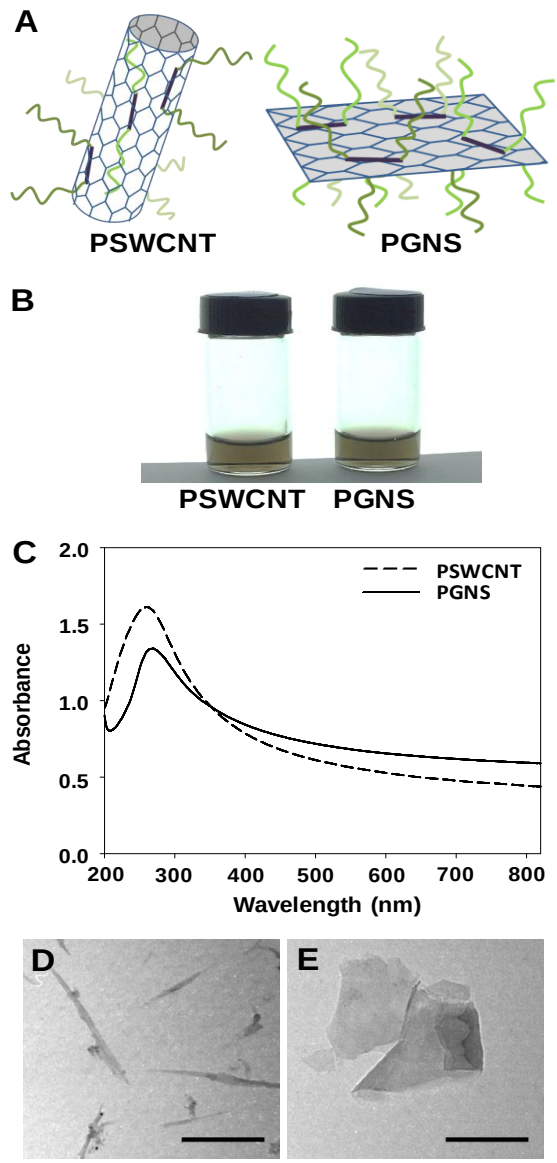

Fig. IV-1. Structure, dispersion, UV spectra and TEM images of the PSWCNT and PGNS.

PSWCNT or PGNS were prepared (A), and dispersed in fetal bovine serum (B). UV absorbance spectrum (C) and TEM images of the PSWCNT or PGNS (D). The scale bar indicates 500 nm.

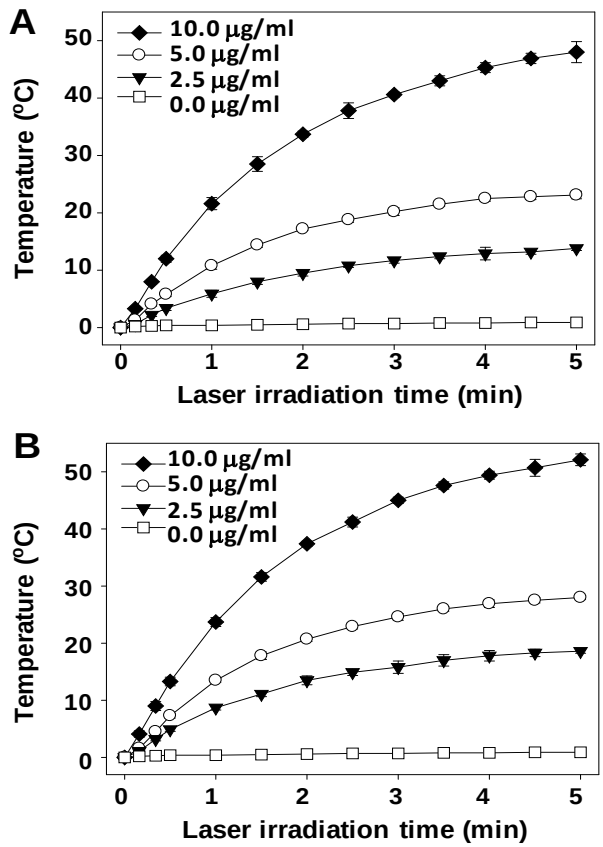

Fig. IV-2. Photothermal capacities of the PSWCNT and PGNS.

Upon irradiation with 808 nm laser, the temperature of PSWCNT (A) or PGNS (B) suspensions was measured by a real-time infrared thermal imaging.

3.2. Structure-dependent cellular uptake of photoresponsive carbon nanomaterials

Although the PGNS samples shared several physical properties with the PSWCNT samples, they displayed different degrees of cellular uptake. SCC7 cells took up PGNS to a greater degree than they took up PSWCNT (Fig. IV-3). One day post-treatment, the harvested cell pellets treated with PGNS or PSWCNT displayed clearly different colors (Fig. IV-3A). The cells treated with PSWCNT were gray in color, whereas the cells treated with PGNS were vivid black in color. These qualitative observations indicated the presence of higher amounts of carbon in the PGNS-treated cells. The cellular uptake of the carbon-based nanomaterials in each cell type was quantitatively measured by treating the cells with a fluorescent marker-labeled PSWCNT or PGNS. Consistent with the qualitative color observations, fluorescence microscopy images revealed higher fluorescence intensity in the cells treated with Cy5.5-labeled PGNS (Fig. IV-3C) as compared to the cells treated with Cy5.5-labeled PSWCNT (Fig. IV-3B). Flow cytometry measurements of the cells revealed a 4.4-fold higher fluorescence intensity of the Cy5.5 signal as compared to the Cy5.5-labeled PSWCNT (Fig. IV-3D, IV-3E).

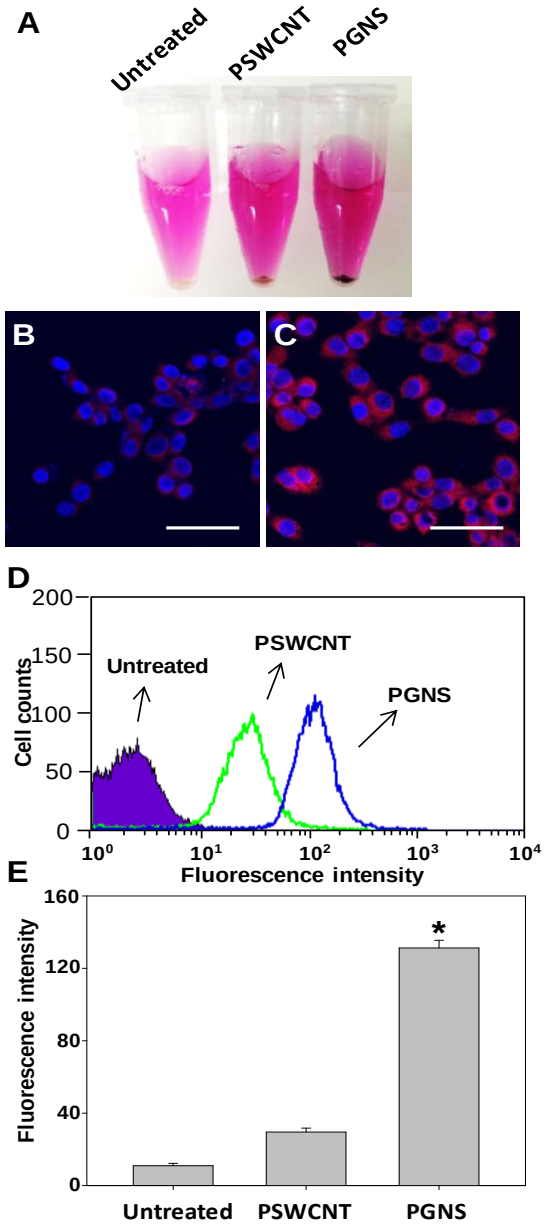

Fig. IV-3. Cellular uptake of the PSWCNT and PGNS.

SCC7 cells were left untreated or treated with PSWCNTT or PGNS. After 24 h, the appearances of the pellets formed from untreated, PSWCNT, or PGNS-treated

cells were photographed (A). Fluorescence confocal microscopy images of the SCC7 cells treated with DSPE-PEG_{5000}-Cy5.5-labeled PSWCNT (B) or PGNS (C). Representative flow cytometry data (D), and quantitation of the fluorescence cellular intensity data (E) are presented. The scale bar indicates 50 μm. *Significantly higher ($p < 0.05$) compared to the other groups (assessed by the ANOVA and the Student–Newman–Keuls test).

3.3. Carbon nanostructure effect on *in vitro* NIR laser-induced photothermal activity

The photothermal effects produced by irradiating the PSWCNT and PGNS in the treated cells were examined by real-time infrared thermal imaging (Fig. IV-4). The temperature of the cell suspension was observed to increase during the 2 min NIR laser (808 nm) irradiation time (Fig. IV-4A). The untreated cells showed an increase of temperature by 3.4℃ after 2 min irradiation (Fig. IV-4B). The temperature of the cells treated with PSWCNT increased with the irradiation time to a lower extent than did the temperature of the cells treated with PGNS. The cells treated with PSWCNT showed an increase of 14.5℃ after 2 min irradiation. By contrast, the cells treated with PGNS increased in temperature by 44.4℃ after 2 min irradiation (Fig. IV-4B).

3.4. Structure effect of carbon nanomaterials on *in vitro* NIR laser-induced anticancer activity

NIR laer-induced anticancer activity differed depending on the structure of photoresponsive carbon nanomaterials. In parallel with measuring the photothermal effects of the PSWCNT and PGNS, the viability of the tumor cells was monitored following NIR laser irradiation. The survival of the tumor cells after NIR laser irradiation was found to depend on the type of carbon nanomaterial present in the cells (Fig. IV-5). The irradiation of cells with a NIR laser over 2 min did not affect the viability of the untreated cells. The survival of the tumor cells treated with PSWCNT was similarly unaffected by the 2 min irradiation time,

displaying an 83.8 ± 2.1% survival. The survival of the tumor cells treated with PGNS, however, decreased significantly as the NIR laser irradiation time increased. After 2 min of NIR irradiation, the survival of the tumor cells treated with PGNS was 19.5 ± 3.3%.

3.5. Structure effect of carbon nanomaterials on pharmacokinetic profiles

Pharmacokinetic profiles of carbon nanomaterials were affected by their structures. PGNS differed from PSWCNT in the pharmacokinetic profile following intravenous administration to mice. The PGNS levels in the bloodstream over 48 h were significantly higher than the PSWCNT levels over the same period of time (Fig. IV-6). At 8 h post-administration, the blood level of PGNS was 11-fold higher than that of PSWCNT. Moreover, at 48 h after intravenous administration, the blood level of PGNS was 17-fold higher as compared to the level of PSWCNT. The area under the curve (AUC) value for PGNS was 158,327,416.5 35,156,119.5 photon counts· h/ml, a factor of 7.4 higher than the AUC value for PSWCNT, 21,281,433.2 4,770,082.5 photon counts ·h/ml. The mean residence time (MRT) of PGNS was 20.9 86 ± 1.2 h, a factor of 2.2 longer than the MRT of PSWCNT (9.7 ± 0.2 h).

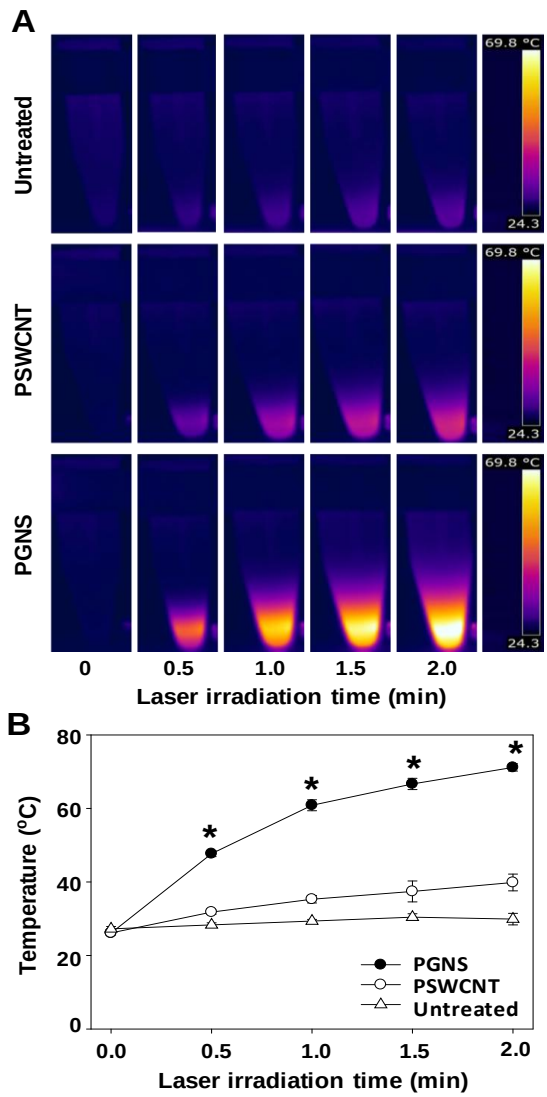

Fig. IV-4. Photothermal effects of the PSWCNT and PGNS.

Temperature increases induced by the presence of PSWCNT or PGNS-treated cells upon irradiation were observed using real-time infrared thermal imaging techniques (A). The temperature of cell suspension was measured using the FLIR QuickReport 1.2 software (B). *Significantly higher ($p < 0.05$) compared to the other groups (assessed by the ANOVA and the Student–Newman–Keuls test).

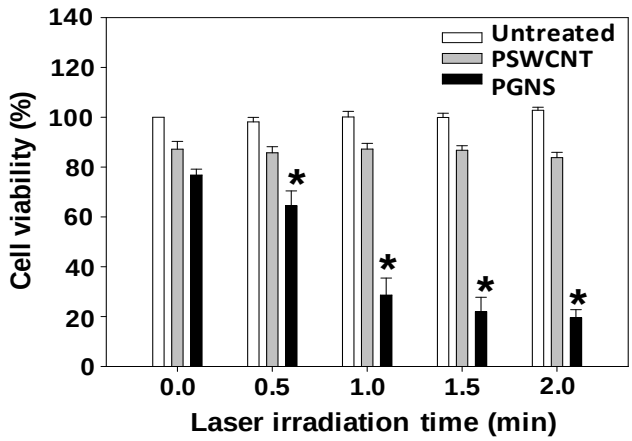

Fig. IV-5. Photothermal cancer cell-killing effects of the PSWCNT and PGNS.

SCC7 cells were left untreated or treated with PSWCNT or PGNS. The viabilities of the cells were measured using the CCK8 assay after laser irradiation for various periods of time. *Significantly lower ($p < 0.05$) compared to the other groups (assessed by the ANOVA and the Student–Newman–Keuls test).

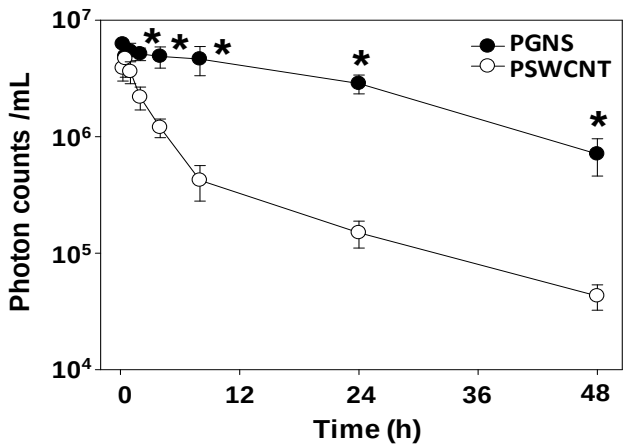

Fig. IV-6. Blood concentration–time profiles for the PSWCNT and PGNS.

Mice were injected intravenously with DSPE-PEG5000-Cy5.5-labeled PSWCNT or PGNS. After a single injection, blood samples were collected over the subsequent 48 h. The fluorescence intensities of the blood samples were measured using a molecular imaging system. *Significantly higher ($p < 0.05$) compared to the PSWCNT-treated group (assessed by the T-test).

3.6. Effect of carbon nanostructure on *in vivo* biodistribution and photothermal effects

A biodistribution study revealed the differential tumor distribution of PGNS and PSWCNT. The distribution of PGNS in the tumor compared to the non-tumor tissue was higher than the corresponding value for PSWCNT (Fig. IV-7). At day 1 after dosing, the distribution at the tumor sites was higher in the PGNS-treated mice than in the PSWCNT-treated mice (Fig. IV-7A). The retention of PGNS at the tumor site differed significantly from the retention of PSWCNT over 7 days post-dosing. The photon count measurements indicated that the PGNS concentration in the tumor tissue was a factor of 2 times the PSWCNT value at day 1 and a factor of 2.8 times the PSWCNT value at day 7 post-dosing (Fig. IV-7B). The thermal detector showed that the highest tissue temperature was induced by NIR laser irradiation of the tumor tissue in the PGNS-treated group (Fig. IV-7C). After 3 min irradiation, the temperature of the tumor site was elevated to 45.1 ± 1.1 ℃ in the PSWCNT-treated group, versus 64.9 ± 1.1 ℃ in the PGNS-treated group (Fig. IV-7D).

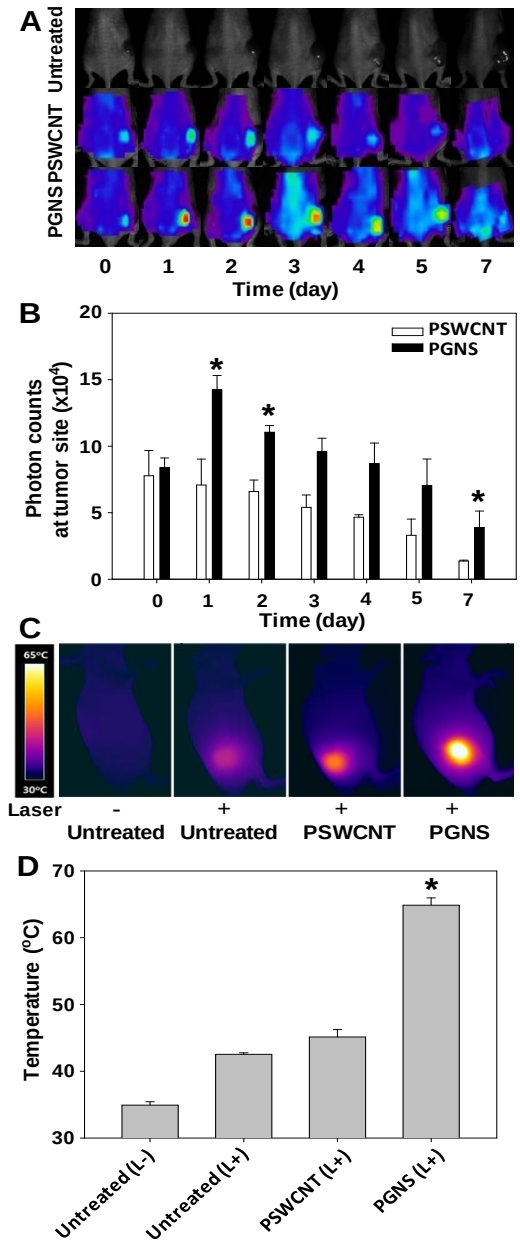

Fig. IV-7. *In vivo* biodistribution and photothermal effects of the PSWCNT and PGNS.

SCC7-bearing mice were injected intravenously with DSPE-PEG_{5000}-Cy5.5-labeled

PSWCNT or PGNS. The *in vivo* distributions of the Cy5.5 fluorescence were visualized over the subsequent 7 days using a molecular imaging system (A). The photon counts at the tumor tissue sites were quantified using the Optiview software (B). Immediately after irradiation with the 808 nm laser, the temperature changes at the tumor site were visualized by real-time infrared thermal imaging (C), and the temperature of the tumor site was measured using the FLIR QuickReport 1.2 software (D). (L-), laser non-irradiated; (L+), laser irradiated. *Significantly higher ($p < 0.05$) compared to the other groups (assessed by the ANOVA and the Student–Newman–Keuls test).

3.7. Structure-dependent photothermal antitumor effects of carbon nanomaterials after NIR laser irradiation *in vivo*

Structure of carbon nanomaterials affected the photothermal antitumor activity. The antitumor activity of PGNS after irradiation with an 808 nm NIR laser (Fig. IV-8) was examined. At day 7 after tumor inoculation, the mice were intravenously injected with PSWCNT or PGNS. Following the irradiation of the tumor sites with the NIR laser, black scabs were found to form at mice treated with PSWCNT and PGNS. The mice treated with PGNS showed darker and wider areas of blackening around the tumor tissues at day 8 (Fig. IV-8A). The black scabs that formed on the PSWCNT-treated mice were partial and did not inhibit the further growing of the tumor volume over time (Fig. IV-8B). Moreover, the mice treated with PGNS but not irradiated showed tumor growth similar to that observed in the untreated mice (Fig. IV-8B). By contrast, the black scabs that formed on the mice treated with PGNS and irradiated with NIR light were completely detached from the tumor sites, and the mice showed no signs of the tumor mass at day 21 (Fig. IV-8A). Histology data revealed the partial destruction of tumor cell nuclei in the PGNS-treated and NIR laser-irradiated group, but not in other groups (Fig. IV-8C). The survival of the NIR-irradiated and PGNS-treated mice was significantly longer than the survival observed in the other groups (Fig. IV-8D). All mice in the PSWCNT- and PGNS-treated groups that were not irradiated died within 45 days of tumor inoculation. After NIR irradiation, 100% of the PSWCNT-treated mice died within 62 days of tumor inoculation. After NIR irradiation, however, 100% of the mice treated with PGNS survived over the 70 days following tumor

inoculation.

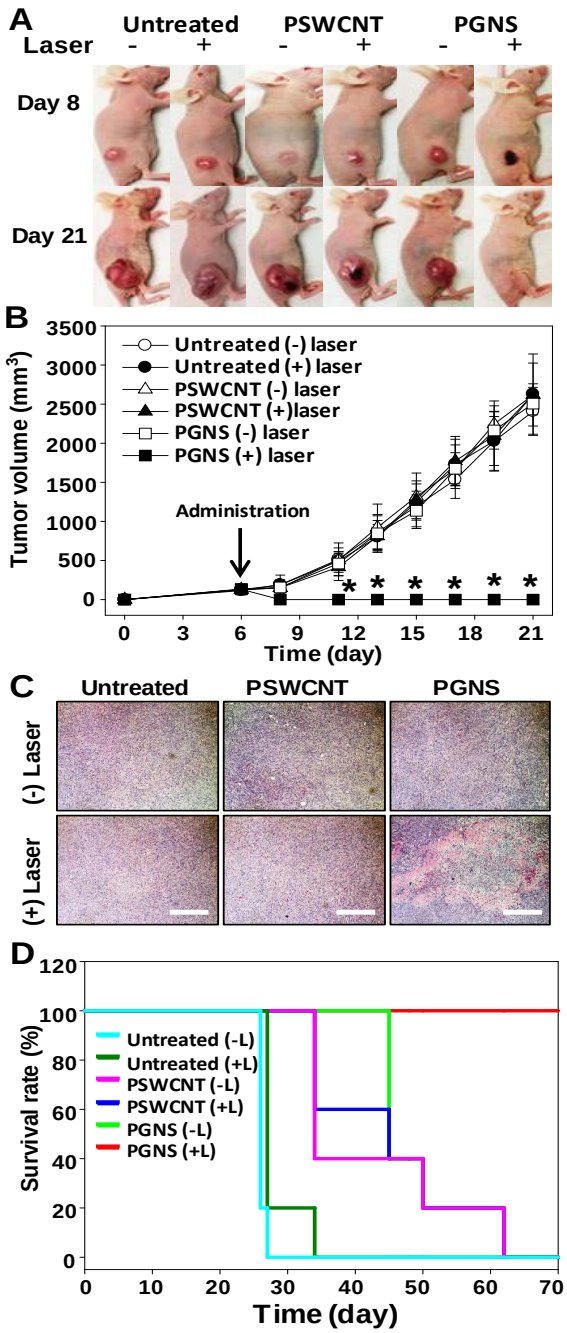

Fig. IV-8. Laser-induced photothermal anticancer effects of the PSWCNT and PGNS.

SCC7-bearing mice were intravenously treated with PSWCNT or PGNS by administering a single injection on day 6. After 24 h, the tumor tissues were irradiated with an 808 nm laser at a power density of 1.2 W/cm^{2}for3min. Starting on the following day (day 8), the appearances of the tumor sites were observed until day 21 (A). The tumor volumes were periodically measured using calipers (B). A histological study was conducted by extracting the tumor tissues after laser irradiation. The tissues were then sectioned for hematoxylin and eosin staining (C). The survival of the mice in each group was monitored daily after irradiation (D). The scale bar indicates 100 mm. *Significantly lower ($p < 0.05$) compared to the other groups (assessed by the ANOVA and the Student–Newman–Keuls test).

4. Discussion

In this chapter, we demonstrated that the *in vitro* and *in vivo* behaviors of photoresponsive carbon nanomaterials differed significantly depending on their structures. The structure of carbon-based nanomaterials affected the *in vitro* cellular uptake and photo-induced antitumor effects. Moreover, the structure of carbon nanomaterials affected the pharmacokinetics, tumor accumulation, and photothermal tumor ablation capacity. The structure comparison study showed that PGNS was greater than the corresponding properties of PSWCNT. Notably, the survival rates of the NIR-irradiated and PGNS-treated mice were substantially longer than the survival rates of the non-irradiated or PSWCNT-treated mice.

Here, both carbon nanotubes and graphene nanosheets were coated with the triblock amphiphilic copolymer, poloxamer 407. Both carbon nanomaterials functionalized with poloxamer 407 exhibited good aqueous stabilities without aggregation in serum (Fig. IV-1B). Poloxamer 407 has been used previously to prepare aqueous dispersions of carbon nanotubes [16] and graphene [13]. Functionalizing graphene oxide with poloxamer 407 was shown to enhance the stability of the graphene oxide in an electrolyte solution [17]. The stability of the PGNS and PSWCNT dispersions arose from the hydrophilicity of the polyethylene moieties on poloxamer 407. Because poloxamer 407 is composed of a central hydrophobic block of polypropylene glycol flanked by two hydrophilic blocks of polyethylene glycol, the hydrophobic polypropylene glycol formed a strong physical bond to the surfaces of the GNS or SWCNT, and the hydrophilic groups

stabilized the surfaces in water. Poloxamer 407 has been approved as an excipient by the United State Food and Drug Administration for various formulations, including intravenous injection, oral suspension, inhalation, and topical dosages [18]. The functionalization of GNS and SWCNT with an FDA-approved copolymer removes the regulatory concerns that surround chemical conversion methods, which involve the use of toxic catalysts.

The structure of carbon nanomaterials did not affect the heating capacity. The heating capacity of PGNS was found to be similar to that of PSWCNT under aqueous conditions (Fig. IV-2). The photothermal heating capacity of graphene was previously reported to exceed that of SWCNT [12]. In the previous study, the materials used to coat the graphene and SWCNT differed. Graphene sheets were coated with polyvinyl pyrrolidone, and SWCNT were coated with sodium dodecylbenzenesulfonate [12]. In our study, both the PGNS and PSWCNT samples were coated with the same functionalization copolymer, which eliminated the possibility that the observed differences arose from differences in the coating materials.

Unlike the heating capacity, the cellular uptake was influenced by the structure of carbon nanomaterials. The *in vitro* study revealed that PGNS provided a higher cellular uptake than PSWCNT (Fig. IV-3). The cell internalization mechanisms were similar, and both the SWCNT and GNS were reported to enter the cells via direct penetration and endocytosis. SWCNT have been reported to directly penetrate the membrane, similar to the actions of nanoneedles, without damaging the cells [19]. Other studies have suggested that energy-dependent

endocytosis, especially clathrin-mediated endocytosis, may be responsible for cellular internalization of the functionalized SWCNT [20, 21]. Similarly, endocytosis and direct penetration have been proposed as possible mechanisms whereby graphene nanomaterials are taken up in cells [22, 24]. The reasons underlying the higher degree to which PGNS is internalized in cells, as compared to PSWCNT, have not yet been clarified. It is possible that the larger surface areas of the graphene nanomaterials (~2600 m^2/g) [25] compared to the SWCNT (~1300 m^2/g) [21] could improve the interactions between the graphene and the cellular membrane, thereby promoting internalization.

Similar to the cellular uptake, *in vivo* pharmacokinetic profiles were affected by the structure of carbon nanomaterials. Pharmacokinetic studies have revealed that PGNS circulates in the blood for a longer period of time, with a larger MRT, than PSWCNT following intravenous administration. The length and branching structures of PEG chains have been reported to be critical to the *in vivo* behavior of SWCNT.[24] Longer and more branched PEG molecules on SWCNT afford longer blood retention times and a lower reticuloendothelial system uptake [26]. Because the surfaces of the PGNS and PSWCNT were identically functionalized with poloxamer 407, it is unlikely that the coating material contributed to the different pharmacokinetic profiles. Rather, it is more likely that the geometric differences between the nanosheets and nanotubes played an important role in the clearance rates of the nanomaterials from the body.

Indeed, a previous study reported that the geometry of a nanocarrier could affect the hemodynamic force and trajectory in the blood stream [27]. The study

reported that flexible filament-like polymeric micelles persisted in circulating blood ten times longer than spherical micelles in rodents [28]. Despite such progress, our understanding of the effects of nanomaterials shape on the pharmacokinetic profile is limited. The influence of the one-dimensional shape of a nanomaterials (i.e., carbon nanotubes) as opposed to a two-dimensional shape (i.e., graphene) on the respective biological responses, especially on the specific organ distributions of the materials *in vivo*, is yet to be elucidated further.

The structure-dependent higher tumor ablation rate and prolonged survival of PGNS-treated mice upon irradiation (Fig. IV-8) may result from the prolonged circulation and higher tumor tissue accumulation of PGNS compared to PSWCNT. Thanks to the prolonged blood circulation time, PGNS was observed to efficiently accumulate in the tumor tissue after 24 hour post-administration (Fig. IV-7A). PSWCNT displayed a shorter MRT than PGNS and was more rapidly eliminated from mice. PSWCNT were therefore localized at the tumor site to a lesser extent than the PGNS. The PGNS and PSWCNT materials lacked specific targeting moieties; therefore, the distributions of PGNS and PSWCNT in the tumor tissues may have resulted from the enhanced penetration and retention effects of the materials [29]. Local irradiation of the PGNS-treated mice resulted in the formation of black scabs that were localized at the tumor tissues. Complete recovery of the mice followed the detachment of the scabs. Previously, an increase in the tumor tissue temperature of up to 60 ℃ was shown to be sufficient for local tumor ablation without affecting the surrounding tissues [30, 31].

5. References

[1] Zhang Z, Wang J, Chen C. Near-infrared light-mediated nanoplatforms for cancer thermo-chemotherapy and optical imaging. Adv Mater 2013; 25:3869-80.

[2] Maltzahn GV, Park JH, Agrawal A, Bandaru NK, Das SK, Sailor MJ, Bhatia SN. Computationally guided photothermal tumor therapy using long-circulating gold nanorod antennas. Cancer Res 2009; 69: 3892-900.

[3] Iancu C, Mocan L. Advances in cancer therapy through the use of carbon nanotube-mediated targeted hyperthermia. Int J Nanomed 2011; 6: 1675-84.

[4] Choi WI, Kim JY, Kang C, Byeon CC, Kim YH, Tae G. Tumor regression *in vivo* by photothermal therapy based on gold-nanorod-loaded, functional nanocarriers. ACS Nano 2011; 5: 1995-2003.

[5] Helmchen F, Denk W. Deep tissue two-photon microscopy. Nat. Methods 2005; 2: 932-40.

[6] Welsher K, Liu Z, Sherlock SP, Robinson JT, Chen Z, Daranciang D, et al. A route to brightly fluorescent carbon nanotubes for near-infrared imaging in mice. Nat. Nanotechnol 2009; 4: 773-80.

[7] Wang Y, Black KC, Luehmann H, Li W, Zhang Y, Cai X, et al. Comparison study of gold nanohexapods, nanorods, and nanocages for photothermal cancer treatment. ACS Nano 2013; 7: 2068-77.

[8] Moon HK, Lee SH, Choi HC. *In vivo* near-infrared mediated tumor destruction by photothermal effect of carbon nanotubes. ACS Nano 2009; 3: 3707-13.

[9] Yang K, Zhang S, Zhang G, Sun X, Lee ST, Liu Z. Graphene in mice: ultrahigh *in vivo* tumor uptake and efficient photothermal therapy. Nano Lett 2010; 10: 3318-23.

[10] Wu MC, Deokar AR, Liao JH, Shih PY, Ling YC. Graphene-based photothermal agent for rapid and effective killing of bacteria. ACS Nano 2013; 7: 1281-90.

[11] Huang X, El-Sayed IH, Qian W, El-Sayed MA. Cancer cell imaging and photothermal therapy in the near-infrared region by using gold nanorods. J Amer Chem Soc 2006; 128: 2115-20.

[12] Markovic ZM, Harhaji-Trajkovic LM, Todorovic-Markovic BM, Kepic DP, Arsikin KM, Jovanovic SP, et al. *In vitro* comparison of the photothermal anticancer activity of graphene nanoparticles and carbon nanotubes. Biomaterials 2011; 32: 1121-9.

[13] Seo JW, Green AA, Antaris AL, Hersam MC. High-concentration aqueous dispersions of graphene using nonionic, biocompatible block copolymers. J Phys Chem Lett 2011; 2: 1004-8.

[14] Lotya M, King PJ, Khan U, De S, Coleman JN. High-concentration, surfactant-stabilized graphene dispersions. ACS Nano 2010; 4: 3155-62.

[15] Liu Z, Tabakman SM, Chen Z, Dai H. Preparation of carbon nanotube bioconjugates for biomedical applications. Nat Protoc 2009; 4: 1372-82.

[16] Bardi G, Tognini P, Ciofani G, Raffa V, Costa M, Pizzorusso T. Pluronic-coated carbon nanotubes do not induce degeneration of cortical neurons *in vivo* and *in vitro*. Nanomed-Nanotechnol 2009; 5: 96-104.

[17] Hong BJ, Compton OC, An Z, Eryazici I, Nguyen ST. Successful stabilization of graphene oxide in electrolyte solutions: enhancement of biofunctionalization and cellular uptake. ACS Nano 2012; 6: 63-73.

[18] Dumortier G, Grossiord JL, Agnely F, Chaumeil JC. A review of poloxamer 407 pharmaceutical and pharmacological characteristics. Pharm Res 2006; 23: 2709-28.

[19] Pantarotto D, Briand JP, Prato M, Bianco A. Translocation of bioactive peptides across cell membranes by carbon nanotubes. Chem Comm 2004; 1: 16-7.

[20] Feazell RP, Nakayama-Ratchford N, Dai H, Lippard SJ. Soluble single-walled carbon nanotubes as longboat delivery systems for platinum(IV) anticancer drug design. J Amer Chem Soc 2007; 129: 8438-9.

[21] Meng L, Zhang X, Lu Q, Fei, Z, Dyson PJ. Single walled carbon nanotubes as drug delivery vehicles: targeting doxorubicin to tumors. Biomaterials 2012; 33: 1689-98.

[22] Huang J, Zong C, Shen H, Liu M, Chen B, Ren B, et al. Mechanism of cellular uptake of graphene oxide studied by surface-enhanced Raman spectroscopy. Small 2012;8: 2577-84.

[23] Vila M, Portoles MT, Marques PA, Feito MJ, Matesanz MC,

Ramirez-Santillan C, et al. Cell uptake survey of pegylated nanographene oxide. Nanotechnology 2012; 23:465103.

[24] Mullick Chowdhury S, Lalwani G, Zhang K, Yang JY, Neville K, Sitharaman B. Cell specific cytotoxicity and uptake of graphene nanoribbons. Biomaterials 2013; 34:283-93.

[25] Stoller MD, Park S, Zhu Y, An J, Ruoff RS. Graphene-based ultracapacitors. Nano Lett 2008; 8: 3498-502.

[26] Liu Z, Davis C, Cai W, He L, Chen X, Dai H. Circulation and long-term fate of functionalized, biocompatible single-walled carbon nanotubes in mice probed by Raman spectroscopy. Proc Natl Acad Sci USA 2008; 105:1410-5.

[27] Decuzzi P, Pasqualini R, Arap W, Ferrari M. Intravascular delivery of particulate ystems: does geometry really matter? Pharm Res 2009; 26: 235-43.

[28] Geng Y, Dalhaimer P, Cai S, Tsai R, Tewari M, Minko T, et al. Shape effects of filaments versus spherical particles in flow and drug delivery. Nat Nanotechnol 2007; 2:249-55.

[29] Matsumura Y, Maeda H. A new concept for macromolecular therapeutics in cancer chemotherapy: mechanism of tumoritropic accumulation of proteins and the antitumor agent smancs. Cancer Res 1986; 46: 6387-92.

[30] Ma Y, Tong S, Bao G, Gao C, Dai Z. Indocyanine green loaded SPIO nanoparticles with phospholipid-PEG coating for dual-modal imaging and photothermal therapy. Biomaterials 2013; 34: 7706-14.

[31] Zheng X, Zhou F, Wu B, Chen WR, Xing D. Enhanced tumor treatment using biofunctional indocyanine green-containing nanostructure by intratumoral or intravenous injection. Mol Pharmaceut 2012;9: 514-22.

Chapter V

Graphene nanosheets loaded with indocyanine green for targeted and enhanced photothermal anticancer therapy

1. Introduction

Photothermal therapy (PTT) utilizes photoresponsive agents taken up by cells and the conversion of absorbed light into local heating to destroy malignant tissue [1]. PTT is considered as a minimally invasive cancer treatment approach and advantageous over chemotherapy owing to spatial and temporal controllability [2-4], resulting in limited side effects which commonly occur in chemotherapy due to unspecific drug delivery to all tissues including healthy ones. In addition, multidrug resistance is always a great concern in chemotherapy, leading to treatment failure [5], which is possible to be avoided by PTT when an ablative temperature is reached, thus to induce irreversible tissue necrosis [6].

Until now, several types of near-infrared (NIR) dyes with maximal absorption peak at NIR region are explored as photo-absorbers for photothermal anticancer therapy [7]. Among them, indocyanine green (ICG) is the only one to be used clinically for imaging of retinal and choroidal vasculatures, as well as for guiding biopsies [8]. However, the use of ICG suffers dramatically from light-induced fast decomposition [9, 10] and quick clearance with a plasma half-life of 2-4 min [11]. Thus various modalities have been utilized to improve the photo-stability and prolong blood retention of ICG, encompassing calcium phosphosilicate nanoparticles, superparamagnetic iron oxide nanoparticles, gold nanoparticles and polymeric micelles [12-16].

Carbon-based nanomaterials such as carbon nanotubes (CNTs), graphenes, and fullerenes have been intensely studied for photothermal therapy applications.

On a per mass basis, CNTs and graphenes both exhibit a larger extinction coefficient of NIR light absorption than gold nanomaterials, and consequently higher photothermal conversion efficiency [17]. CNTs were functionalized by various molecules such as PEG, DNA, antibodies and folates for passive or active photothermal killing of cancer cells and malignant tissue upon irradiation with NIR laser [18-21]. Intravenous administration of PEG-conjugated graphene nanosheets has been exhibited ultrahigh tumor retention and efficient photothermal antitumor efficacy [22]. In chapter IV, we demonstrated that poloxamer 407-functionalized graphene nanosheets showed superior photothermal tumor ablation capacity to poloxamer 407-functionalized carbon nanotubes in murine xenograft tumor model [23]. Although graphene-based nanosheets have their own photothermal effect, the reduction of injection dose would be desirable in the prospective of safety issue.

In this chapter, we tested whether the use of graphene-based photothermal nanoplatform for delivery of ICG could improve the photothermal potency. Moreover, to enhance tumor accumulation, cellular internalization and subsequent photothermal tumor destruction efficacy, we used cholesteryl hyaluronic acid-coated reduced graphene oxide nanosheets (CHA-rGO) for ICG delivery vehicle to CD44-overexpressing xenograft tumor.

2. Materials and methods

2.1. Preparation of ICG-loaded nanosheets

To prepare ICG-loaded rGO (rGO/ICG) or ICG-loaded CHA-rGO (CHA-rGO/ICG) nanosheets, 0.2 ml of rGO or CHA-rGO nanosheets (rGO 0.5 mg/ml, CHA-rGO 1.5 mg/ml) in TDW were added with 0.2 ml of ICG aqueous solution (100 μM, Sigma-Aldrich), and 0.6 ml of TDW. After stirring the mixture for 2 h at room temperature, free ICG was removed using a PD-10 desalting column (GE Healthcare, Buckinghamshire, UK).

For the measurement of ICG loading efficiency, serial amount of ICG was added to rGO or CHA-rGO nanosheets (rGO concentration was fixed at 100 μg/ml; ICG concentration was ranged from 10 μM to 100 μM). After mixing for 2 h at room temperature, unbound free ICG was removed by PD-10 desalting column. The content of ICG was quantified with UV spectrometer at 810 nm after subtraction the absorbance of rGO or CHA-rGO using a UV-Vis spectrophotometer (UV-3100, Shimadzu Corp, Tokyo, Japan). The loading efficiencies were calculated by the percentage of ICG content before and after purification.

2.2. Stability test of ICG-loaded nanosheets

The stability of rGO and CHA-rGO nanosheets with and without ICG loading was tested in phosphate buffered saline (PBS, 150 mM, pH 7.4). An aliquot (0.2 ml) of testing samples in TDW was added to 0.8 ml of PBS, and the solutions were

allowed to stand for 7 days. The stability of CHA-rGO/ICG nanosheets was evaluated during this period by monitoring the mixtures for the appearance of precipitates using a digital camera (Canon PC1089, Canon Inc, Tokyo, Japan).

2.3. Size and zeta potential measurement

The morphology and lateral sizes of the generated nanosheets were measured using transmission electron microscopy (TEM) and dynamic light scattering, respectively. The morphology of nanosheets was examined by transmission electron microscopy (JEM1010; JEOL Ltd, Tokyo, Japan). The rGO or CHA-rGO nanosheets were diluted with TDW and placed in an ELS-Z (Photal, Osaka, Japan). The hydrodynamic diameters of the nanosheets were determined by He-Ne laser (10 mW) light scattering, and the zeta potential values of rGO and CHA-rGO nanosheets with or without ICG loading were determined using an ELS-8000 instrument (Photal, Osaka, Japan). The samples were diluted with TDW and zeta potential values were determined by laser Doppler microelectrophoresis at an angle of 22^{o}.

2.4. Photothermal effect and photo-stability of ICG complexed by CHA-rGO nanosheets

Photothermal properties were measured by IR thermal imaging system after irradiation of each sample. Free ICG solution (concentration of ICG 1 μM), or suspensions of rGO (5 μg/ml), rGO/ICG (rGO 5 μg/ml, ICG 1 μM), CHA-rGO (15 μg/ml), and CHA-rGO/ICG (15 mg CHA-rGO μg/ml, ICG 1 μM) were irradiated

using an 808 nm continuous wave NIR diode laser beam (BWT Beijing LTD, Beijing, China) with an output power of 1.2 W. The temperature of the suspensions during laser irradiation was recorded using an IR thermal imaging system every 30 seconds (FLIR T420, FLIR Systems Inc., Danderyd, Sweden). To test the stability of ICG during NIR laser irradiation, the visible spectra of free ICG, rGO/ICG and CHA-rGO were monitored every 30 seconds by UV spectrometer in the range of 400 nm - 950 nm.

2.5. *In vitro* photothermal effect of CHA-rGO/ICG following laser irradiation

Human KB epidermal carcinoma cells (American Type Culture Collection, Rockville, MD, USA) were cultured in RPMI-1640 medium (Gibco BRL life Technologies, Carlsbad, CA, USA) supplemented with 10% fetal bovine serum and 100 units/ml penicillin plus 100 μg/ml streptomycin (complete RPMI-1640 media). KB cells were seeded onto 12-well plates at a density of 1×10^5 cell/well. The following day, cells were treated with free ICG, rGO, rGO/ICG, CHA-rGO, or CHA-rGO/ICG at an ICG concentration of 5μM and nanosheets concentration of 20 μg/ml. After 24 h incubation at 37 ℃, the cells were washed twice with cold phosphate buffered saline (PBS) and re-suspended in complete RPMI-1640 media. The cell suspensions were irradiated with an 808 nm continuous-wave NIR diode laser at an output power of 1.2W for various exposure periods. Immediately after irradiation, the cells were diluted 10-fold using complete RPMI-1640 media and transferred to 96-well plates for the cell viability assays. The cell viability was

quantified using a Cell Counting Kit-8TM (CCK8) according to the protocol provided by the manufacturer (Dojindo Molecular Technologies, Inc., Rockville, MD, USA). The values are expressed as a percentage of the cell viability measured in the control groups.

2.6. Animals

In vivo experiments were conducted using five-week old female Balb/c athymic nude mice supplied by Orient Bio. Lab. Animal Inc. (Seungnam, Kyonggi-do, South Korea, approved animal experimental protocol number SNU-130129-3-1). Animals were raised under standard pathogen-free conditions at the animal center for pharmaceutical research in the Seoul National University. All animal experiments were conducted in accordance with the Guidelines for the Care and Use of Laboratory Animals of the Institute of Laboratory Animal Resources, Seoul National University.

2.7. *In vivo* photothermal study

The photothermal anticancer effects of CHA-rGO/ICG were tested using KB tumor-bearing nude mice. Five-week old athymic nude mice (Orient Bio, Inc.) were subcutaneously injected at the dorsal right side with 2×10^6 KB cells. When the tumor volume reached 80–100 mm^3, the mice were subjected to intravenous administration of free ICG, rGO, rGO/ICG, CHA-rGO, or CHA-rGO/ICG at the rGO dose of 5 mg/kg, the CHA dose of 10 mg/kg, and the ICG dose of 1 mg/kg. One hour post-administration, the mice were anesthetized and positioned in a

mouse holder. The tumor sites were irradiated for 3 min with an 808 nm continuous wave NIR laser at an output power of 1.2W. Light-induced temperature changes in the tumor region were recorded using a real-time infrared thermal imaging system (FLIRT420, FLIR Systems Inc., Danderyd, Sweden). The tumor sizes were measured in two dimensions using a slide caliper, and the tumor volume was calculated according to the equation $a \times b^2 \times 0.5$, where a is the largest and b is the smallest diameter. In some experiments, the tumor tissues were extracted on day 20 after drug administration, and fixed in 10% neutral buffered formalin and embedded in paraffin blocks for further histological evaluation. Tumor tissue sections (4 mm thick) were immunostained with an anti-proliferating cell nuclear antigen (PCNA) antibody (Thermo Fisher Scientific) and subjected to terminal deoxynucleotidyl transferase dUTP nick-end labeling (TUNEL) assays (Millipore Corporation, Billerica, MA, USA) to determine cell-proliferation status and apoptosis, respectively. The numbers of proliferating and apoptotic cells were counted using the image analysis software, Image-Pro Plus Version 6.0 (Media Cybernetics, Inc., Rockville, MD, USA), after photographing five different fields at a magnification of 200 using an Eclipse TE2000-S microscope (Nikon, Tokyo, Japan).

2.8. Statistics

ANOVA was used for statistical evaluation of experimental data, using Student-Newman-Keuls test for a post-hoc test. All statistical analyses were done using the SigmaStat software (version 3.5, Systat Software, Richmond, CA, USA),

and a p-value < 0.05 was considered significant.

3. Results

3.1 Characterization of CHA-rGO/ICG nanophysisorplexes

ICG was loaded onto the surfaces of rGO or CHA-rGO nanosheets via π-π interaction as illustrated in Fig. V-1A. At rGO:ICG weight ratio of 5:1, the loading efficiency of rGO and CHA-rGO nanosheets were 100.4 ± 3.6 % and 92.3 ± 5.0 %, respectively (Fig. V-1B). The morphology of rGO/ICG (Fig. V-2A) did not differ from these of CHA-rGO/ICG (Fig. V-2B). The loading of ICG did not significantly affect the sizes of rGO and CHA-rGO (Fig. V-2C). The zeta potential values of nanosheets were decreased after loading of ICG onto rGO (Fig. V-2D). Immediately after dispersion in PBS, aggregation was formed in rGO/ICG whereas the stable dispersion of CHA-rGO/ICG was maintained at least for 7 days (Fig. V-2E).

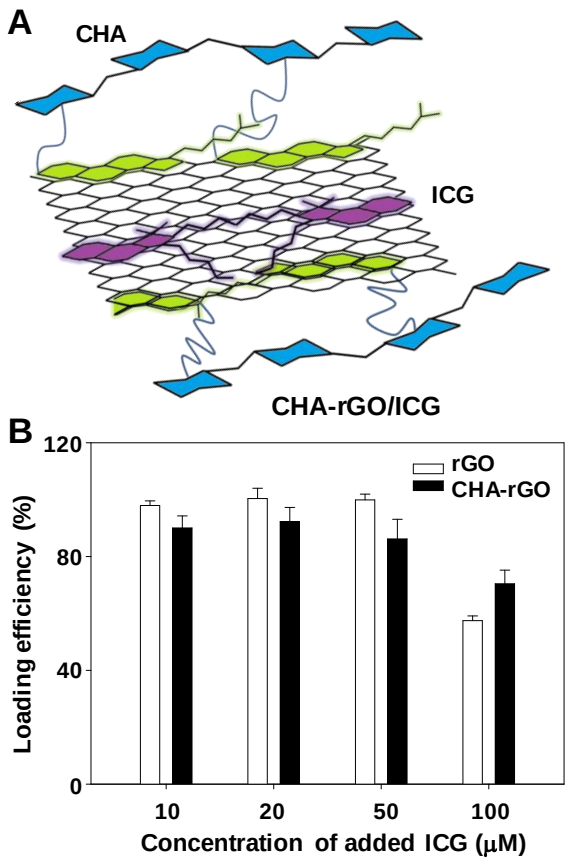

Fig. V-1. Illustration of CHA-rGO/ICG nanophysisorplexes and loading efficiency of ICG

The schematic illustration of CHA-rGO/ICG nanophysisorplexes is shown in (A). The loading efficiency of ICG on rGO or CHA-rGO was measured using a UV/vis spectrophotometer (B).

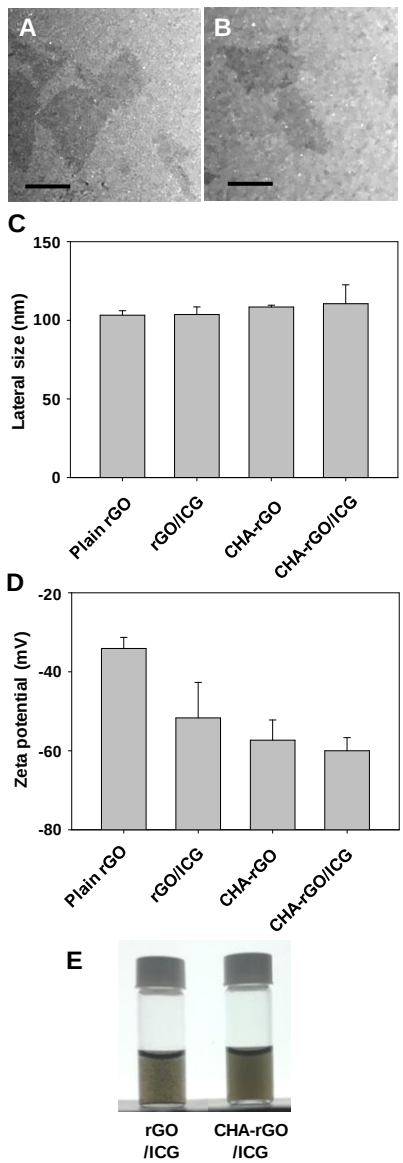

Fig. V-2. Characterization of CHA-rGO/ICG nanophysisorplexes.

TEM images of rGO/ICG (A) and CHA-rGO/ICG (B) were obtained. The lateral diameters of rGO, rGO/ICG, CHA-rGO, and CHA-rGO/ICG were measured by dynamic light scattering (C). The zeta potentials were determined using an

electro-Doppler method (D). The stability of rGO/ICG and CHA-rGO/ICG nanosheet suspensions was evaluated in PBS (E).

3.2 Photothermal effect and photo-stability of ICG on nanosheets

Compared to free ICG, ICG on nanosheets showed different photothermal effect and photo-stability. With laser irradiation, free ICG increased temperature. However, the extent of temperature increase by free ICG was almost saturated after 2 min of laser irradiation. The temperature increase by free ICG after 1, 2, and 5 min irradiation was 2.3 ± 0.3, 3.4 ± 0.2, 4.2 ± 0.3 ^{o}C, respectively (Fig.V-3A). Both rGO and CHA-rGO similarly showed higher thermal conductivity than free ICG, with gradual temperature increase in proportion to the irradiation time. The temperature increased by rGO and CHA-rGO after 5 min irradiation was 15.1 ± 0.3 and 14.5 ± 0.4 ^{o}C, respectively. Unlike free ICG, ICG on nanosheets displayed continuous increase of temperature in line with the irradiation time. The temperature increased by rGO/ICG and CHA-rGO/ICG after 5 min irradiation was 23.6 ± 0.8 and 23.4 ± 0.6 ^{o}C, respectively (Fig.V-3B). Photo-stability significantly differed between ICG in free form and on nanosheets. UV spectra of free ICG reveal that NIR absorption peak of free ICG was rapidly lost upon irradiation. After 1 min of irradiation, the NIR absorption peak of ICG almost disappeared (Fig.V-3C). In contrast, ICG on rGO (Fig. V-3D) or CHA-rGO (Fig.V-3E) retained its NIR absorption peak even after 5 min of irradiation.

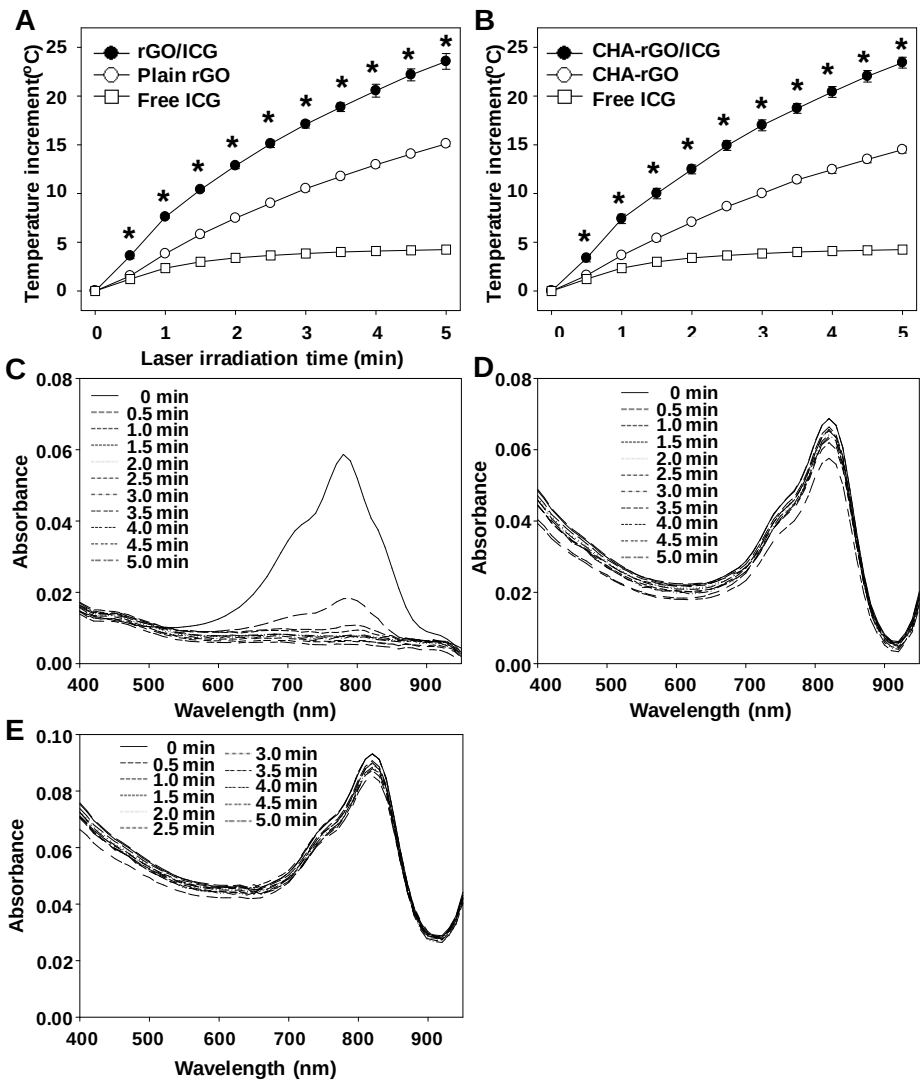

Fig. V-3. Photothermal behavior and photo-stability of the CHA-rGO/ICG nanophysisorplexes.

Irradiation with an 808 nm laser increases the temperatures of the rGO/ICG (A) or CHA-rGO/ICG (B) suspensions, as measured using real-time infrared thermal imaging techniques. UV absorbance spectrum of free ICG (C), rGO/ICG (D), or

CHA-rGO/ICG (E) was measured with different laser irradiation time. *Significantly different ($p < 0.05$) from the other groups (ANOVA and Student-Newman-Keuls test).

3.3. Cellular uptake and photothermal antitumor effects of ICG delivered using CHA-rGO nanosheets

Although rGO/ICG and CHA-rGO/ICG showed similar thermal conductivity (Fig. V-4), they differed in cellular uptake and *in vitro* photothermal antitumor effects. In KB cells, the cell pellets treated with CHA-rGO or CHA-rGO/ICG appeared to be much darker as compared to those treated with rGO or rGO/ICG (Fig. V-4A). The temperature increase of cell suspensions after irradiation depended on the CHA and ICG on rGO nanosheets. The irradiation-induced temperature increase was the highest in the group treated with CHA-rGO/ICG, followed by CHA-rGO, rGO/ICG, rGO, and free ICG (Fig. V-4A, 4B). Real-time IR thermal imaging showed that the temperature of cell suspension was 77.8 ± 2.3 ^{o}C in the group treated with CHA-rGO/ICG after 3 min irradiation, which was 2.4-fold higher than the temperature of the cells treated with free ICG (Fig.V-4B). In the absence of NIR irradiation, no group showed significant killing of KB cells (Fig.V-4C). However, after 3 min NIR irradiation, more than 90% of KB cells were dead only in the group treated with CHA-rGO/ICG.

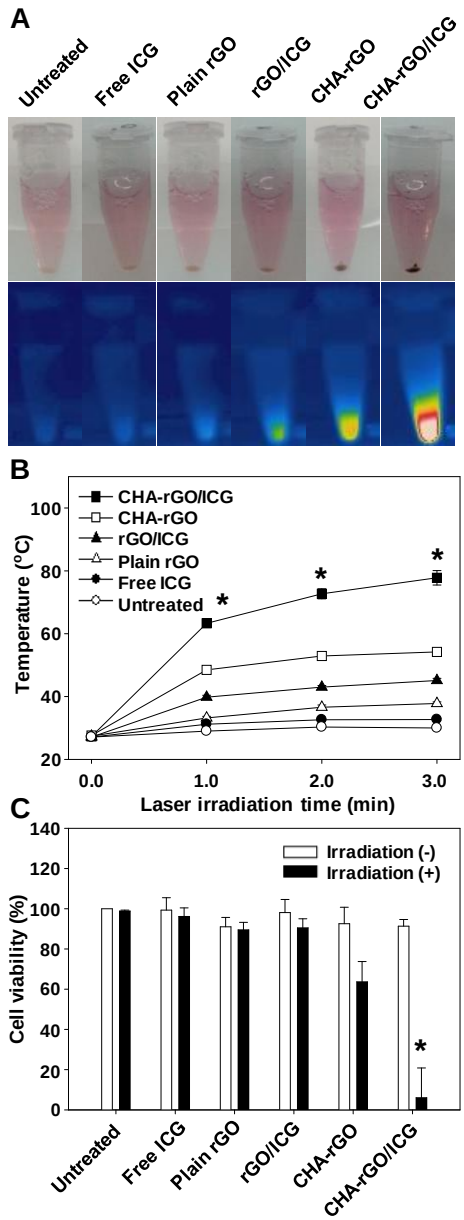

Fig. V-4. Photothermal antitumor effect of the CHA-rGO/ICG.

KB cells were left untreated or treated with free ICG, rGO, rGO/ICG, CHA-rGO, or CHA-rGO/ICG. After 24 h, the appearances of the pellets and the real-time

temperature increases upon irradiation from untreated or the samples-treated cells were observed (A). The highest cell suspension temperature was measured using the FLIR QuickReport 1.2 software (B). The viabilities of the cells were measured using the CCK8 assay after laser irradiation (C). *Significantly different ($p < 0.05$) from the other groups (ANOVA and Student-Newman-Keuls test).

3.4. *In vivo* photothermal effect of ICG delivered by CHA-rGO nanosheets

After systemic administration of CHA-rGO/ICG to KB tumor-bearing mice, the temperature increase of tumor sites was monitored by IR thermal imaging (Fig. V-5). One hour post-treatment, the highest temperature was observed in the tumor tissues of the group treated with CHA-rGO/ICG after 3 min of NIR laser irradiation (Fig. V-5A). In CHA-rGO/ICG-treated group, the temperature of tumor site was 49.4 ± 1.0 ^{o}C, which was 9.0 and 9.2 ^{o}C higher than rGO/ICG and free ICG-treated groups, respectively (Fig.V-5B).

3.5. *In vivo* antitumor effect of CHA-rGO/ICG nanophysisorplexes

In vivo photothermal antitumor effect was improved by delivery of ICG using CHA-rGO nanosheets. Although there was single NIR irradiation on day 1, free ICG, rGO, rGO/ICG, and CHA-rGO-treated group revealed rapid growth rate (Fig.V-6A, V-6C) with the tumor volumes over 2300 mm^3 on day 20 after drug administration (Fig.V-6B). In contrast to these groups, the mice treated with CHA-rGO/ICG showed different response to irradiation. One day after NIR irradiation (day 2), tumor sites were covered with black scab, which was almost completely detached on day 20 with complete eradication of tumor mass (Fig.V-6B, V-6C). The tumor cell proliferation and apoptosis were evaluated by immunohistochemistry (Fig. V-7). The number of PCNA-positive cells of tumor tissues was significantly lower in the group treated with CHA-rGO/ICG in comparison with other groups (Fig. V-7A, V-7C). Tunnel assay showed the highest

population of apoptotic cells in the group treated with CHA-rGO/ICG (Fig. V-7B, V-7D). The number of apoptotic cells in the tumor tissue of CHA-rGO/ICG-treated group was 20.8-fold and 61.6-fold higher than that of free ICG-treated group and untreated group, respectively (Fig. V-7D).

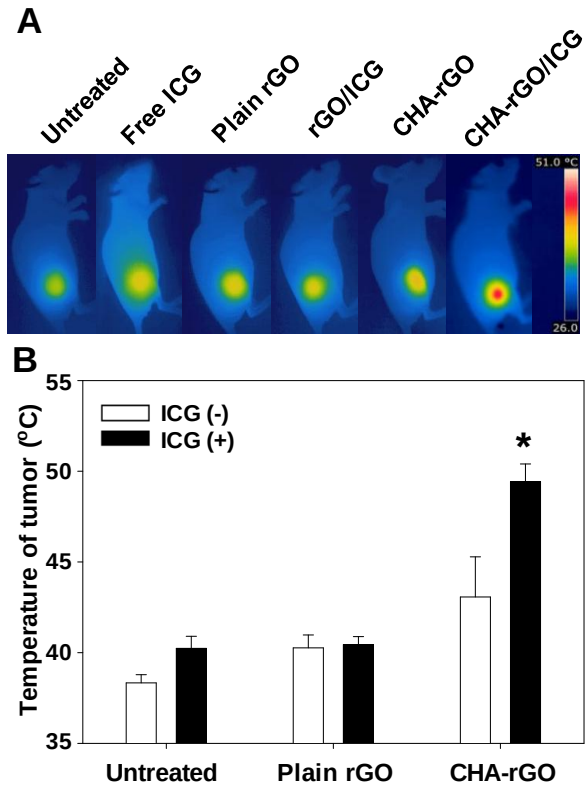

Fig. V-5. *In vivo* photothermal effect of the CHA-rGO/ICG nanophysisorplexes.

KB-bearing mice were injected intravenously with free ICG, rGO, rGO/ICG, CHA-rGO, or CHA-rGO/ICG. Immediately after irradiation with the 808 nm laser, the real-time temperature changes at the tumor site were visualized by real-time infrared thermal imaging (A), and the average temperature of the tumor site was measured using the FLIR QuickReport 1.2 software (B). *Significantly higher ($p < 0.05$) compared to the other groups (assessed by the ANOVA and the Student–Newman–Keuls test).

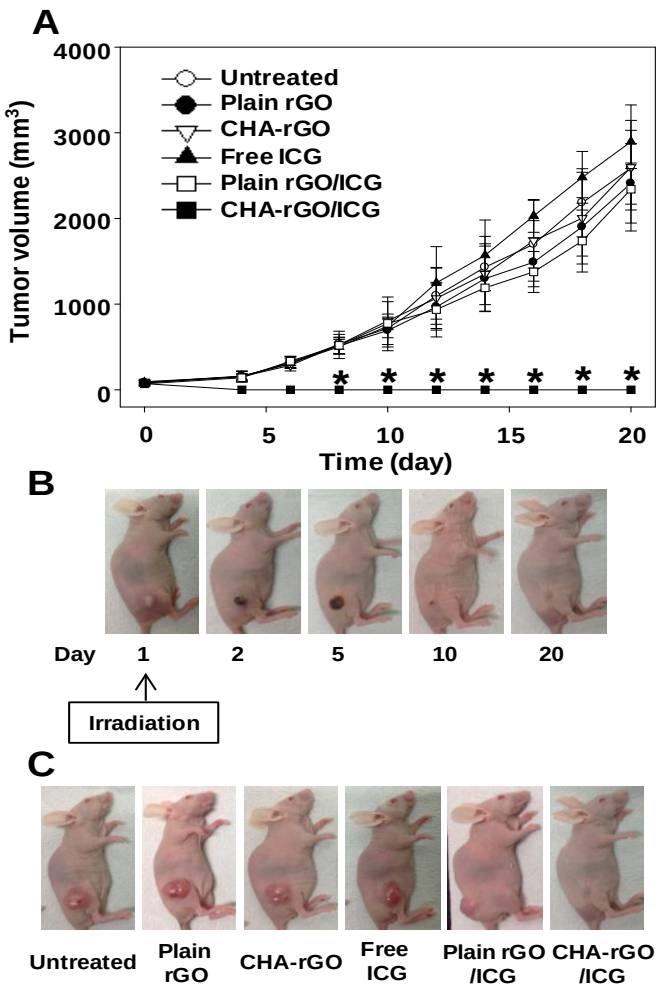

Fig. V-6. Laser-induced photothermal antitumor effect of the CHA-rGO/ICG nanophysisorplexes.

KB-bearing mice were intravenously treated with free ICG, rGO, rGO/ICG, CHA-rGO, or CHA-rGO/ICG by administering a single injection on day 0. After 24 h, the tumor tissues were irradiated with an 808 nm laser at a power density of 1.2 W/cm2 for 3 min. The tumor volumes were periodically measured using calipers until day 20 (A). Starting on the day 1, the appearances of the tumor sites

of CHA-rGO/ICG-treated mice were monitored (B). On day 20, the appearances of all groups were observed (C). ($n = 5$) *Significantly lower ($p < 0.05$) compared to the other groups (assessed by the ANOVA and the Student–Newman–Keuls test).

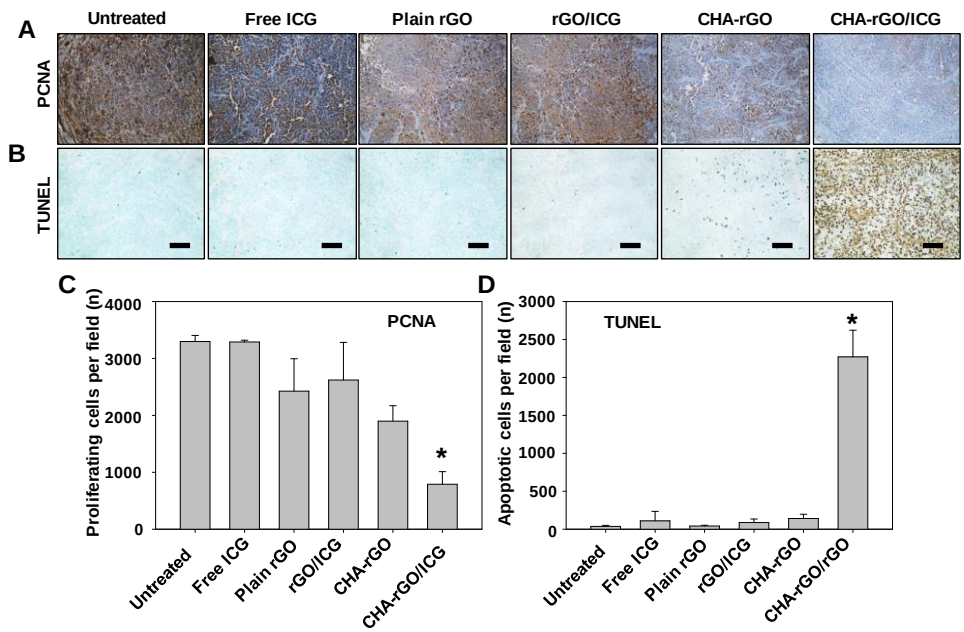

Fig. V-7. Immunohistochemistry of tumor tissues.

Tumor tissues were excised and sectioned for anti-PCNA antibody immunostaining (A) and TUNEL assay (B). The numbers of PCNA-immunostained proliferating cells (C) and TUNEL-labeled apoptotic cells (D) in isolated tumor tissues were determined (n = 5) Bar size = 100mm. *Significantly different ($p < 0.05$) from the other groups (ANOVA and Student-Newman-Keuls test).

4. Discussion

In this chapter, we demonstrated that the photothermal potency of ICG can be highly increased by delivery onto CHA-rGO nanosheets. ICG in free form suffered from photo-induced decomposition after NIR laser irradiation. However, by loading onto rGO or CHA-rGO nanosheets, ICG could retain its photo-stability after NIR laser irradiation. Although rGO/ICG and CHA-rGO/ICG showed similar thermal conductivity *in vitro*, CHA-rGO/ICG showed the higher photothermal effect in cell level and tumor-bearing mice.

We observed that the photo-stability of ICG could be highly increased when loaded onto rGO or CHA-rGO nanosheets (Fig. V-3D, V-3E). ICG is an amphiphilic dye with high absorption in NIR range. The NIR absorption peak of free ICG rapidly decomposed after 1 min of irradiation. Consistent with our result, ICG is known to rapidly decompose into small fragments upon absorbing energy from light [10, 24]. Such instability of ICG to light has restricted its application as either fluorescence imaging agent or photothermal absorber. Enhanced photo-stability of ICG on rGO or CHA-rGO nanosheets is probably due to graphene-mediated efficient quenching of electron donor (singlet oxygen) [25, 26]. Since singlet oxygen was reported to catalyze the photo-induced decomposition of ICG [10], the quenching of electron donor by rGO or CHA-rGO nanosheets may increase the photo-stability of ICG.

Although rGO/ICG and CHA-rGO/ICG showed similar thermal conductivity, treatment of KB cells with CHA-rGO/ICG showed higher photothermal effect (Fig.

V-4C). The higher *in vitro* KB cell-killing effect of CHA-rGO/ICG can be explained by the higher cellular uptake of CHA-rGO/ICG via HA receptors on KB cells. In chapter III, We demonstrated that CHA-coated graphene oxide nanosheets could more efficiently deliver doxorubicin into CD44-overexpressed KB cells efficacy. Moreover, the darkest black color pellets of cells treated with CHA-rGO/ICG (Fig. V-4A) supports that the highest KB cell photothermal killing effect could be related to the enhanced uptake of CHA-rGO/ICG.

In addition, CHA-rGO is of advantageous for delivery of ICG against plain rGO in terms of stable loading capacity *in vivo*. Anionic ICG can be efficiently loaded onto the surface of rGO via π-π stacking, leading to decreased zeta potential of rGO/ICG (Fig V-2C). But ICG loaded CHA-rGO owns similar zeta potential value with CHA-rGO, indicating the ICG interacts with rGO rather than CHA superficially. Similar with other ICG delivery vehicles[13, 14, 16, 27], such inside encapsulation of ICG within CHA-rGO could enable higher stability and prolonged circulation time in blood owing to decreased accessibility to blood component. When loaded by rGO, ICG is more possible to be released before reaching tumor site, either by passive diffusion or displacement by serum proteins from plain rGO.

The *in vivo* photothermal tumor ablation effects of ICG were greatest in KB tumor-bearing mice treated with CHA-rGO/ICG. The enhanced photothermal effect is probably contributed to the higher distribution of CHA-rGO/ICG to the tumor tissue. This notion is supported by our observation that the local tumor tissue temperature was the highest in the group treated with CHA-rGO/ICG (Fig.

V-5A). Since the thermal conductivity of both rGO/ICG and CHA-rGO/ICG was similar *in vitro*, it is likely that the higher temperature could be due to the higher distribution of CHA-rGO/ICG to tumor tissues. Previously, hyaluronic acid derivative-coated carbon nanotubes were reported to distribute to the hyaluronic acid receptor-overexpressing tumor tissue more effectively [28, 29].

The lack of cell proliferation and high population of apoptotic cells was observed in the tissues treated with CHA-rGO/ICG, but not with CHA-rGO or ICG alone (Fig. V-7). Although CHA-rGO alone indeed showed an increase of tumor tissue temperature to 43 ^{o}C, it did not significantly induce the apoptosis of tumor cells. The real time thermo-analyzer revealed that the temperature at tumor tissues was elevated to 49.4 ^{o}C only in the group treated with CHA-rGO/ICG. Cellular damage is known to occur when temperature is increased to 50-52 ^{o}C for 4-6 min due to the denaturation of proteins [30]. In our study, ICG loaded graphene nanosheets were employed as light absorber to convert energy to heat in tumor site. Similar with other photothermal modalities, such as gold nanorods, the heat transfer from the surface of graphene to the surrounding cellular environment is highly localized and decays exponentially with a few nanometers [33]. By that reason, the temperature of graphene surface would be higher than 50-52 ^{o}C, and the cellular protein with close proximity to graphene surface is likely to be highly denatured. Thus cellular internalized CHA-rGO/ICG can be regarded as potent nano-heaters after NIR laser treatment. Thus, the photothermal activity of CHA-rGO/ICG could result from the fast local heating of tumor up to an ablative temperature, inducing irreversible cell deaths.

Although in this study we loaded photolabile ICG onto CHA-rGO, CHA-rGO might be further developed for delivery of other photolabile photothermal chemicals such as cyanine dyes IR-125, IR-806, FS-308 [31, 32]. In addition, to enhancing the photo-stability of such photolabile photothermal agents, the photothermal property of CHA-rGO per se could augment the therapeutic potency of photothermal drugs. In the perspective of CHA-rGO, the loading of photothermal agents could save the dose of CHA-rGO with increased therapeutic outcomes.

5. References

[1] Zhang Z, Wang J, Chen C. Near-infrared light-mediated nanoplatforms for cancer thermo-chemotherapy and optical imaging. Adv Mater 2013; 25:3869-80.

[2] Maltzahn GV, Park JH, Agrawal A, Bandaru NK, Das SK, Sailor MJ, Bhatia SN. Computationally guided photothermal tumor therapy using long-circulating gold nanorod antennas. Cancer Res 2009;69:3892-900.

[3] Iancu C, Mocan L. Advances in cancer therapy through the use of carbon nanotube-mediated targeted hyperthermia. Int J Nanomed 2011;6:1675-84.

[4] Choi WI, Kim JY, Kang C, Byeon CC, Kim YH, Tae G. Tumor regression *in vivo* by photothermal therapy based on gold-nanorod-loaded, functional nanocarriers. ACS Nano 2011;5: 1995-2003.

[5] Min Y, Mao C-Q, Chen S, Ma G, Wang J, Liu Y. Combating the Drug Resistance of Cisplatin Using a Platinum Prodrug Based Delivery System. Angew Chem Int Ed 2012;51:6742-47.

[6] Goldberg SN, Gazelle GS, Mueller PR. Thermal Ablation Therapy for Focal Malignancy. AJR Am J Roentgenol 2000;17:323-31.

[7] Yuan A, Wu J, Tang X, Zhao L, Xu F, Hu Y. Application of near-infrared dyes for tumor imaging, photothermal, and photodynamic therapies. J Pharm Sci 2013;102:6-28.

[8] Namikawa K, Yamazaki N. Sentinel lymph node biopsy guided by indocyanine green fluorescence for cutaneous melanoma. Eur J Dermatol

2011;21:184-90.

[9] Saxena V, Sadoqi M, Shao J. Degradation kinetics of indocyanine green in aqueous solution. J Pharm Sci 2003;92:2090-97.

[10] Engel E, Schraml R, Maisch T, Kobuch K, Konig B, Szeimies RM, Hillenkamp J, Baumler W, Vasold R. Light-induced decomposition of indocyanine green. Invest Ophthalmol Vis Sci 2008;49:1777-83.

[11] Desmettre T, Devoisselle JM, Mordon S. Fluorescence Properties and Metabolic Features of Indocyanine Green (ICG) as Related to Angiography. Surv Ophthalmol 2000;45:15-27.

[12] Barth BM, E IA, Shanmugavelandy SS, Kaiser JM, Crespo-Gonzalez D, DiVittore NA, McGovern C, Goff TM, Keasey NR, Adair JH, Loughran TP, Claxton DF, Kester M. Targeted indocyanine-green-loaded calcium phosphosilicate nanoparticles for *in vivo* photodynamic therapy of leukemia. ACS Nano 2011;5:5325-37.

[13] Ma Y, Tong S, Bao G, Gao C, Dai Z. Indocyanine green loaded SPIO nanoparticles with phospholipid-PEG coating for dual-modal imaging and photothermal therapy. Biomaterials 2013;34:7706-14.

[14] Yang H, Mao H, Wan Z, Zhu A, Guo M, Li Y, Li X, Wan J, Yang X, Shuai X, Chen H. Micelles assembled with carbocyanine dyes for theranostic near-infrared fluorescent cancer imaging and photothermal therapy. Biomaterials 2013;34:9124-33.

[15] Kuo WS, Chang YT, Cho KC, Chiu KC, Lien CH, Yeh CS, Chen SJ. Gold nanomaterials conjugated with indocyanine green for dual-modality

photodynamic and photothermal therapy. Biomaterials 2012;33:3270-78.

[16] Yue C, Liu P, Zheng M, Zhao P, Wang Y, Ma Y, Cai L. IR-780 dye loaded tumor targeting theranostic nanoparticles for NIR imaging and photothermal therapy. Biomaterials 2013;34:6853-61.

[17] Robinson JT, Tabakman SM, Liang Y, Wang H, Casalongue HS, Vinh D, Dai H. Ultrasmall reduced graphene oxide with high near-infrared absorbance for photothermal therapy. J Am Chem Soc 2011;133: 6825-31.

[18] Chakravarty P, Marches R, Zimmerman NS, Swafford AD-E, Bajaj P, Musselman IH, Pantano P, Draper RK, Vitetta ES. Thermal ablation of tumor cells with antibody-functionalized single-walled carbon nanotubes. Proc Natl Acad Sci 2008;105:8697-702.

[19] Zhou F, Wu S, Wu B, Chen WR, Xing D. Mitochondria-Targeting Single-Walled Carbon Nanotubes for Cancer Photothermal Therapy. Small 2011;7:2727-35.

[20] Ghosh S, Dutta S, Gomes E, Carroll D, D'Agostino R, Olson J, Guthold M, Gmeiner WH. Increased Heating Efficiency and Selective Thermal Ablation of Malignant Tissue with DNA-Encased Multiwalled Carbon Nanotubes. ACS Nano 2009;3:2667-73.

[21] Burke A, Ding X, Singh R, Kraft RA, Levi-Polyachenko N, Rylander MN, Szot C, Buchanan C, Whitney J, Fisher J, Hatcher HC, D'Agostino R, Kock ND, Ajayan PM, Carroll DL, Akman S, Torti FM, Torti SV. Long-term survival following a single treatment of kidney tumors with multiwalled carbon nanotubes and near-infrared radiation. Proc Natl Acad

Sci 2009;106:12897-902.

[22] Yang K, Zhang S, Zhang G, Sun X, Lee S-T, Liu Z. Graphene in Mice: Ultrahigh *In Vivo* Tumor Uptake and Efficient Photothermal Therapy. Nano Lett 2010;10:3318-23.

[23] Miao W, Shim G, Lee S, Oh Y-K. Structure-dependent photothermal anticancer effects of carbon-based photoresponsive nanomaterials. Biomaterials 2014;35:4058-65.

[24] Penha FM, Rodrigues EB, Maia M, Meyer CH, Costa Ede P, Dib E, Bechara E, Lourenco A, Lima Filho AA, Freymuller EH, Farah ME. Biochemical analysis and decomposition products of indocyanine green in relation to solvents, dye concentrations and laser exposure. Ophthalmologica 2013;230 Suppl 2:59-67.

[25] Wang Y, Li Z, Wang J, Li J, Lin Y. Graphene and graphene oxide: biofunctionalization and applications in biotechnology. Trends Biotechnol 2011;29:205-12.

[26] Wojcik A, Kamat PV. Reduced graphene oxide and porphyrin. An interactive affair in 2-D. ACS Nano. 2010;4:6697-706.

[27] Zheng M, Yue C, Ma Y, Gong P, Zhao P, Zheng C, Sheng Z, Zhang P, Wang Z, Cai L. Single-step assembly of DOX/ICG loaded lipid--polymer nanoparticles for highly effective chemo-photothermal combination therapy. ACS Nano 2013;7:2056-67.

[28] Datir SR, Das M, Singh RP, Jain S. Hyaluronate Tethered, "Smart" Multiwalled Carbon Nanotubes for Tumor-Targeted Delivery of

Doxorubicin. Bioconjug Chem 2012;23:2201-13.

[29] Swierczewska M, Choi KY, Mertz EL, Huang X, Zhang F, Zhu L, Yoon HY, Park JH, Bhirde A, Lee S, Chen X. A Facile, One-Step Nanocarbon Functionalization for Biomedical Applications. Nano Lett 2012;12:3613-20.

[30] Zhou J, Chen JK, Zhang Y. Theoretical analysis of thermal damage in biological tissues caused by laser irradiation. Mol Cell Biomech 2007;4:27-39.

[31] Camerin M, Jori G, Della Ciana L, Fabbroni S, Bonacchi S, Montalti M, Prodi L. Photothermal sensitisation and therapeutic properties of a novel far-red absorbing cyanine. Photochem Photobiol Sci 2009;8: 1422-31.

[32] Jiang R, Cheng S, Shao L, Ruan Q, Wang J. Mass-Based Photothermal Comparison Among Gold Nanocrystals, PbS Nanocrystals, Organic Dyes, and Carbon Black. J Phys Chem C 2013;117:8909-15.

[33] Lee SE, Liu GL, Kim F, Lee LP. Remote optical switch for localized and selective control of gene interference. Nano Lett 2009;9:562-70.

Summary

As a novel class of two dimensional nanomaterials with a number of extraordinary optical, thermal and chemcial properties, graphene-based nanosheets (GNS) have gain great interest and the dramatic progress of their applications in nanomedicine and biomedical area has been made in the past few years. In particular, the unique structural features, such as large surface are and ease to functionalize, and intrinsic photoresponsive characteristics of GNS permit promising applications for design of advanced drug delivery systems for a broad range of therapeutics, and phototherapies, such as photodynamic and photothermal therapy for cancer treatment.

Polyethylene glycol-grafted graphene oxide (pGO) have been proven to be a safe and potent multimodal nanocarrier of photosensitizers and synergistic anticancer agents. The pGO nanosheets showed much higher safety than GO nanosheets *in vivo*. Treatment of cells with a photosensitizer chlorin e6 (Ce6) in pGO nanophysisorplexes significantly enhanced cellular delivery compared to that seen with Ce6 alone. The combination and dose reduction indexes revealed that combining doxorubicin (Dox) with Ce6 with at a molar ratio of 1:2 provided the highest synergism. The Ce6 and Dox-loaded pGO nanophysisorplexes (Ce6/Dox/pGO) were 148.0 ± 18.0 nm in size. Molecular imaging of mice showed that Ce6/Dox/pGO could accumulate in tumor tissues over 3 days. Moreover, in

SCC tumor-bearing mice, the photodynamic anticancer effects of Ce6/Dox/pGO were higher than those of Ce6/pGO or Dox/pGO. Moreover, tumor sections from illuminated mice treated with Ce6/Dox/pGO showed substantial disruption of tumor nuclei, whereas the other groups did not. These results suggest that pGO nanosheets have superior *in vivo* safety relative to GO, and that it is possible to enhance the tumor tissue distribution and photodynamic anticancer effects of systemically administered Ce6 by forming multimodal nanophysisorplexes with pGO and synergistic anticancer chemotherapeutics such as Dox.

For tumor active targeting delivery of anticancer agents, cholestryl hyaluronic acid-coated reduced graphene oxide nanosheets (CHA-rGO) were designed and fabricated. Compared with rGO, CHA-rGO nanosheets showed increased colloidal stability under physiological conditions and improved *in vivo* safety, with a survival rate of 100% after intravenous administration of 40 mg/kg in mice. The Dox loading capacity of CHA-rGO was 4-fold greater than that of rGO. Uptake of Dox by CD44-overexpressing KB cells was higher for CHA-rGO than for rGO, and was decreased in the presence of hyaluronic acid through competition for CD44 receptor binding. After intravenous administration in tumor-bearing mice, CHA-rGO/Dox showed higher tumor accumulation than rGO/Dox. The *in vivo* antitumor efficacy of Dox delivered by CHA-rGO was significantly increased compared with free Dox or rGO/Dox. In CHA-rGO/Dox-treated mice, tumor weights were reduced to 14.1% 0.1% of those in untreated mice. These findings indicate that CHA-rGO nanosheets possess greater stability, safety, drug loading capacity, and CD44-mediated delivery of Dox than rGO nanosheets. These

beneficial properties of CHA-rGO improved the distribution of Dox to tumors and facilitated the cellular uptake of Dox by CD44-overexpressing tumor cells, resulting in enhanced anticancer effects.

Photothermal therapy for the treatment of solid tumors has emerged as an attractive alternative approach. Thanks to the high absorption in NIR range, carbon-based nanomaterials (such as GNS and carbon nanotubes) are potent photoresponsive agents for converting absorbed light into local heating through non-irradiative mechanism. Poloxamer 407-functionalized single-walled carbon nanotubes (PSWCNT) and poloxamer 407-functionalized graphene nanosheets (PGNS) were prepared and compared in terms of photoresponsibility, *in vitro* and *in vivo* behaviors and fate. Both of PSWCNT and PGNS exhibited similar physical stability and heating capacities after irradiation with an 808 nm near-infrared (NIR) laser. Despite sharing common physical properties, the cellular uptake of the PSWCNT and PGNS differed significantly. Cancer cells treated with PGNS took up a higher quantity of the nanosheets than of the PSWCNT and displayed a higher rate of cancer cell killing upon laser irradiation. Structure of carbon nanomaterials also affected the *in vivo* behaviors. PGNS could circulate in the blood 2.2 times longer than that of the PSWCNT. PGNS accumulated in the SCC7 tumor tissues to a greater degree than did PSWCNT over 7 days. NIR irradiation resulted in the complete ablation of tumor tissues in the PGNS-treated group but not in the other groups. After NIR irradiation, 100% of the PGNS-treated and NIR-irradiated mice survived until day 70. These results suggest the importance of structure in controlling the *in vivo* behaviors of carbon nanomaterials. The structure of

carbon-based nanomaterials affected the *in vitro* cellular uptake and photo-induced antitumor effects. Moreover, the structure of carbon nanomaterials affected the pharmacokinetics, tumor accumulation, and photothermal tumor ablation capacity. The structure comparison study showed that PGNS was greater than the corresponding properties of PSWCNT. Notably, the survival rates of the NIR-irradiated and PGNS-treated mice were substantially longer than the survival rates of the non-irradiated or PSWCNT-treated mice.

Apart from for delivery of chemotherapeutics, CHA-rGO was utilized as tumor targeted delivery system for a near-infrared dye, ICG. Upon loading onto graphene nanosheets, the laser-induced decomposition of ICG was substantially decreased, resulting in enhanced and synergistic photothermal efficacy. Significant higher internalization of CHA-rGO/ICG and subsequent greater photothermal killing effect after laser irradiation was observed by CD44-overexpressing KB cells. After systemic administration, NIR laser was locally applied to tumor sites. CHA-rGO/ICG treated tumor-bearing mice showed the highest tumor local temperature, which is sufficient to trigger thermal-induced tumor necrosis and destruction. Immunohistological staining also confirmed that greatest percentage of apoptotic cells was exhibited in CHA-rGO/ICG treated and laser-irradiated tumors, which resulted in the formation of black scabs at tumor sites. Complete recovery of the mice followed the detachment of the scabs without recurrence. The results indicate that CHA-rGO nanosheets endow enhanced photo-stability and photothermal efficacy of ICG, permitting great tumor distribution and potent photothermal tumor ablation capacity as an attractive and promising alternative to

other cancer therapies.

Taken together, we have provided evidence that GNS can be used as novel delivery vehicles for various chemical drugs and surface-engineered GNS would be a potent modality for photothermal therapy for cancer treatment, which indicates the promise to further explore the utility of GNS as multifunctional and multimodal nanoplatform for anticancer therapy.

요약

항암치료를 위한 그래핀 기반 나노시트의 응용연구

서울대학교 대학원

약학과 물리약학전공

묘원준

그래핀 기반 나노시트(GNS)는 항암치료제 분야에서 신규하고 강력한 나노약물로서 출현해왔다. 우선, 폴리에틸렌 글리콜을 접목한 그래핀 옥사이드(pGO)는 광감작제인 콜린 e6 (Ce6)의 세포 내 전달 효과를 현저히 증강시켰으며, 생체 내 안정성 또한 그래핀 옥사이드 나노시트에 비해 높음을 보여줬다. 게다가 Ce6/Dox/pGO는 증강된 콜로이드성 안정성을 보여주고, 생체내 안정성을 개선시켜주며, 독소루비신(Dox)의 적재 용량을 증강시킬 뿐만 아니라, 세포내 전달 효율도 높인다. KB 종양세포를 이식한 실험쥐의 분자영상을 촬영한 결과 CHA-rGO/Dox가 눈에 띄게 높은 종양 조직 내 축적효과를 보였고, 다른 그룹에 비해 높은 종양성장 억제 효과를 보였다. 세번째로 광반응성 탄소 나노 소재의 구조에 따른 생물학적 특성을 연구했다. 비이온성

계면 활성제인 폴록사머 407로 표면을 코팅한 단층 나노튜브(PSWCNT)와 폴록사머 407로 코팅된 그래핀 나노시트(PGNS)는 유사한 물리적 안정성을 보이고, 808nm 근적외선(NIR) 레이저 조사 후 열용량 또한 유사함을 보였다. PGNS 처리한 종양 세포들이 PSWCNT처리한 종양 세포들에 비하여 보다 많은 양의 나노시트를 흡수하였으며, 그 결과 레이저 조사 후 높은 비율로 암세포들이 죽었다. 게다가 PGNS는 PSWCNT보다 혈액에서 2.2배 오래 순환하였으며, SCC7종양 조직에 더 많이 축적되었다. NIR 조사 결과 다른 그룹과 달리 PGNS 처리한 그룹에서 종양조직이 완전히 제거되었다. 마지막으로 CHA-rGO를 근적외선 염료 ICG의 표적 항암 전달체로 사용하였다. ICG를 CHA-rGO에 탑재하면 ICG 단독 사용 했을 때보다 높은 광안정성을 보였고, NIR 레이저 조사에 따른 광열 효과 또한 높여졌다. 종양세포를 이식한 실험쥐에 CHA-rGO/ICG를 투여했을 때 종양 조직에서 국소적으로 온도가 가장 높았고, 그 결과 종양이 제거되었다. 결론적으로 GNS 다양한 화학 약물의 신규한 전달체로서 사용될 수 있으며, 표면 개질 GNS는 광열치료를 통한 항암 치료제로 유용하게 쓰일 수 있다.

주요어: 그래핀 기반 나노시트, 광역동 치료, 항암화학요법, 광열치료, 향상된 항암 효과

학 번: 2010-31367